Journal of Materials Chemistry A

ROYAL SOCIETY OF CHEMISTRY

REVIEW

View Article Online
View Journal | View Issue

Cite this: *J. Mater. Chem. A*, 2025, **13**, 12712

A review on photocatalytic methane conversion systems: from fundamental mechanisms to the emerging role of ferroelectric materials

Yiming Lei, Xavier Sala, Jordi García-Antón and Jose Muñoz *

Methane (CH_4) conversion is a promising strategy for reducing greenhouse gases, synthesizing high-value-added chemicals, and thus achieving carbon neutralization. However, due to its inertness, CH_4 requires high energy input to initiate the conversion process, which always leads to excessive energy consumption and catalyst deactivation. Along these lines, the use of sunlight as energy input has demonstrated enormous potential to help overcome the uphill thermodynamics of methane conversion under mild reaction conditions. Nevertheless, the high recombination rate of photoinduced charge carriers still hampers photocatalytic efficiency. In the past years, ferroelectric photocatalysts have attracted much attention for dealing with sluggish charge separation/transfer dynamics, presenting themselves as excellent materials for enhancing photocatalytic CH_4 conversion rates under mild conditions. Consequently, this work reviews and discusses four pivotal photocatalytic CH_4 conversion routes, including (i) dry reforming of methane (DRM), (ii) partial oxidation of methane (POM), (iii) non-oxidative coupling of methane (NOCM), and (iv) oxidative coupling of methane (OCM). In particular, special attention has been paid to the recent advances in ferroelectric-assisted photocatalytic CH_4 conversion to elucidate the influence of polarized ferroelectrics in the charge transfer mechanisms. Finally, the main challenges in the field are highlighted, also presenting possible strategies to overcome them in order to encourage more in-depth research on ferroelectric-assisted methane conversion in the future.

Received 2nd December 2024
Accepted 11th March 2025

DOI: 10.1039/d4ta08554j

rsc.li/materials-a

1. Introduction

The rapid global population growth and rising living standards cause the high consumption of fossil fuels, leading to a non-

Departament de Química (Unitat de Química Inorgànica), Facultat de Ciències, Universitat Autònoma de Barcelona (UAB), Cerdanyola del Valles, 08193 Barcelona, Spain. E-mail: JoseMaria.Munoz@uab.cat

Yiming Lei

Yiming Lei is a PhD student in the Department of Chemistry at Universitat Autònoma de Barcelona, Spain (2023–current). He is awarded by the China Scholarship Council (CSC). His current research focuses on the functionalization of 2D Xene materials represented by 2D germanene derivatives for real implementations including (bio) sensor and catalysis.

Jose Muñoz

Dr Jose Muñoz received his PhD in chemistry from Universitat Autònoma de Barcelona (UAB). Afterward, he carried out two postdoctoral stays: the first one at the Materials Science Institute of Barcelona (ICMAB, 2016–2019) with a "Juan de la Cierva" fellow, and the second one at the Central European Institute of Technology (CEITEC, 2020–2022) with an MSCA-IP grant. In 2023 he returned to the UAB as an independent researcher with a "Ramón y Cajal" senior grant. His research interests combine 3D printing technology, 2D materials, and molecular engineering for the development of biosensors and multiresponsive devices.

negligible energy crisis and environmental issues.[1,2] It is predicted that compared to 2018, the total energy demand will increase by about 40% in 2024.[3] Fossil fuels as the dominant energy source will be depleted after 70 years, meaning that the current energy-industry system cannot be maintained without developing an alternative energy source.[4] Besides, a series of environmental issues like climate change and air pollution owing to the over-exploitation of natural resources are the most complex challenges faced today.[5] Therefore, the development of alternative energy resources is extremely urgent due to the increasing growth in energy demand and the necessity to reduce environmental problems.[6,7] With a sufficient reserve of methane (CH_4) hydrate and shale gas, the utilization of methane for industrial production becomes a reliable strategy for replacing petroleum.[8,9] Besides the abundant natural resources, the diversity of synthesis pathways to obtaining CH_4 is also a great advantage to utilizing this high-quality fuel gas. For instance, natural gas is expected to increase from 35.57 Tcf (trillion cubic feet) in 2024 to 42.07 Tcf by 2050, meaning that the chemical synthesis of high-value-added products will be possible on a large scale if suitable methane conversion technologies are realized.[10,11] In addition, biogas—composed of ~60% CH_4—can be generated from animal excrement, wastewater, and food debris *via* anaerobic digestion, which is a clean and green chemistry route.[12] In this regard, CH_4 from biogas can be purified to obtain biomethane as a promising renewable energy for further chemical transformation. Another environmentally friendly production route for preparing CH_4 is CO_2 reduction (or hydrogenation) reactions. CH_4 can be made from CO_2 captured from industrial sources, combined with hydrogen obtained from water splitting using surplus renewable energy. This offers additional opportunities for large-scale CH_4 conversion while reducing the use of fossil fuels and the global greenhouse effect. Thus, the diverse sustainable sources of CH_4 are beneficial for its utilization towards the production of high value-added chemicals, oxygenated products including alcohols and aldehydes chemicals, and even longer chain compounds like long chain alkane.

Methane conversion to added-value chemical products can be classified into two different strategies: indirect and direct routes. While indirect routes include (i) dry reforming of methane (DRM) and (ii) steam reforming of methane (SRM), direct routes are based on (iii) partial oxidation of methane (POM), (iv) oxidative coupling of methane (OCM), and (v) non-oxidative coupling of methane (NOCM). The main difference between these two strategies is the fact that indirect routes need to firstly produce syngas (a mix of CO and H_2) for the production of high-value-added products from methanol (CH_3OH) conversion, as summarized in Table 1.[13] Importantly, these strategies have been shown to be useful in addressing excess greenhouse gas emissions without disrupting current infrastructure.[14–19]

However, because of the thermodynamic stability of methane (440 kJ mol^{-1} for C–H bond cracking) due to its symmetrical tetrahedral geometry, it is difficult to convert methane into high-density energy fuels or chemicals taking into account other small hydrocarbon molecules with low chemical bond energy like 413 and 412 kJ mol^{-1} in propane and ethane, respectively.[14,20,21] To date, the thermocatalytic reaction, carried out at high temperature or pressure, is still the main industrial route of methane conversion.[22] It is undeniable that thermocatalytic processes often cause high energy consumption and catalyst poisoning (generally due to the rapid carbon deposition and catalyst sintering).[23] To overcome these hurdles, increasing attention is paid to photocatalytic methane conversion technologies.

Compared to traditional thermocatalysis and its reaction conditions, photocatalysis is a promising technology that can be carried out under ambient conditions, using photons to drive chemical processes.[24–27] Light illumination causes energetic charge carriers to move across the photocatalyst, significantly reducing the activation energy and overcoming the thermodynamic barrier.[28–31] Thus, photocatalytic methane conversion with solar energy as the only energy input during the reaction process can reduce energy consumption to the greatest extent possible. Typically, over the conventional semiconductor surfaces, the light-driven catalytic reactions can be viewed as three fundamental steps as follows (Fig. 1a):[32,33] (i) when the light irradiates the semiconductor-based photocatalysts, if the energy of the photons is equal to or greater than the semiconductor band gap (E_g), photons can be captured to excite photoelectrons. (ii) Then, the photoelectrons transfer and occupy the conduction band (CB). And the holes stay at the valence band (VB). Afterward,

Table 1 Main products from diverse methane conversion processes

Conversion process	Product	Reaction pathway	ΔG^0 (298 K) [kJ mol^{-1}]
DRM	CO + H_2 (syngas)	$CH_4 + CO_2 \rightarrow 2CO + 2H_2$	170.7
	CH_3COCH_3	$2CH_4 + CO_2 \rightarrow CH_3COCH_3 + H_2O$	114.1
SRM	CO + H_2 (syngas)	$CH_4 + H_2O \rightarrow CO + 3H_2$	142.1
	CH_3OH	$CH_4 + H_2O \rightarrow CH_3OH + H_2$	117.3
	C_2H_5OH	$2CH_4 + H_2O \rightarrow C_2H_5OH + 2H_2$	161.7
POM	CO + H_2 (syngas)	$2CH_4 + O_2 \rightarrow 2CO + 4H_2$	−173
	CH_3OH	$2CH_4 + O_2 \rightarrow 2CH_3OH$	−222.6
	HCHO	$2CH_4 + O_2 \rightarrow 2HCHO + 2H_2$	−103.6
OCM	C_2H_4	$2CH_4 + O_2 \rightarrow C_2H_4 + 2H_2O$	−287.6
	C_2H_6	$4CH_4 + O_2 \rightarrow 2C_2H_6 + 2H_2O$	−320
NOCM	C_2H_6	$2CH_4 \rightarrow C_2H_6 + H_2$	68.6
	C_6H_6	$6CH_4 \rightarrow C_6H_6 + 9H_2$	433.9

electrons migrate to the reduction centres, while holes transfer to oxidation sites. (iii) Finally, the adsorbed reactants will interact with electrons and holes to compete with the photocatalytic redox reactions. And several possible products should be desorbed from the photocatalyst surface to ensure the subsequent reaction cycles. Notably, several factors can affect the whole photocatalytic efficiency. For example, many semiconductor-based photocatalysts have a narrow light response range, which means that they only absorb ultraviolet light and little visible light.[34–37] Therefore, visible-infrared light energy (~90% of the solar energy) is wasted, resulting in a low quantum efficiency.[38–40] In addition, poor adsorption/activation of reactants at the few active sites or high charge transfer resistance in photocatalysts can lead to the recombination of photoexcited carriers before they can participate in the redox process, which is also a major challenge.[41–44] In addition, difficulties in the absorption–desorption also limit the photocatalytic efficiency.[45,46] Among these issues, the sluggish charge separation inhibits the solar conversion and hinders the catalytic process, so improving the charge transfer dynamics is a must to improve the photocatalytic activity. Although the design of co-catalysts[47–50] and heterojunction structures[51–54] got a lot of attention to accelerate the charge transfer process, the efficiency is still not satisfactory for commercial use. Consequently, rationally designed photocatalysts with intrinsic controllable photo-induced charge transfer behaviour are crucial. Under these circumstances, ferroelectrics have been identified as potential materials that might offer new opportunities to further promote charge separation and thus improve photocatalytic activity.

In general, ferroelectric materials are polar non-centrosymmetric (NCS) materials with domain walls.[55] These domain walls can generate an electric field induced by non-coincide positive–negative charge centres. And the NCS crystal structure endows ferroelectrics with spontaneous polarization ability even without external stimulation.[56–61] Thus, an external electric field can simply adjust the polarization directions. However, high-temperature conditions might lead to the

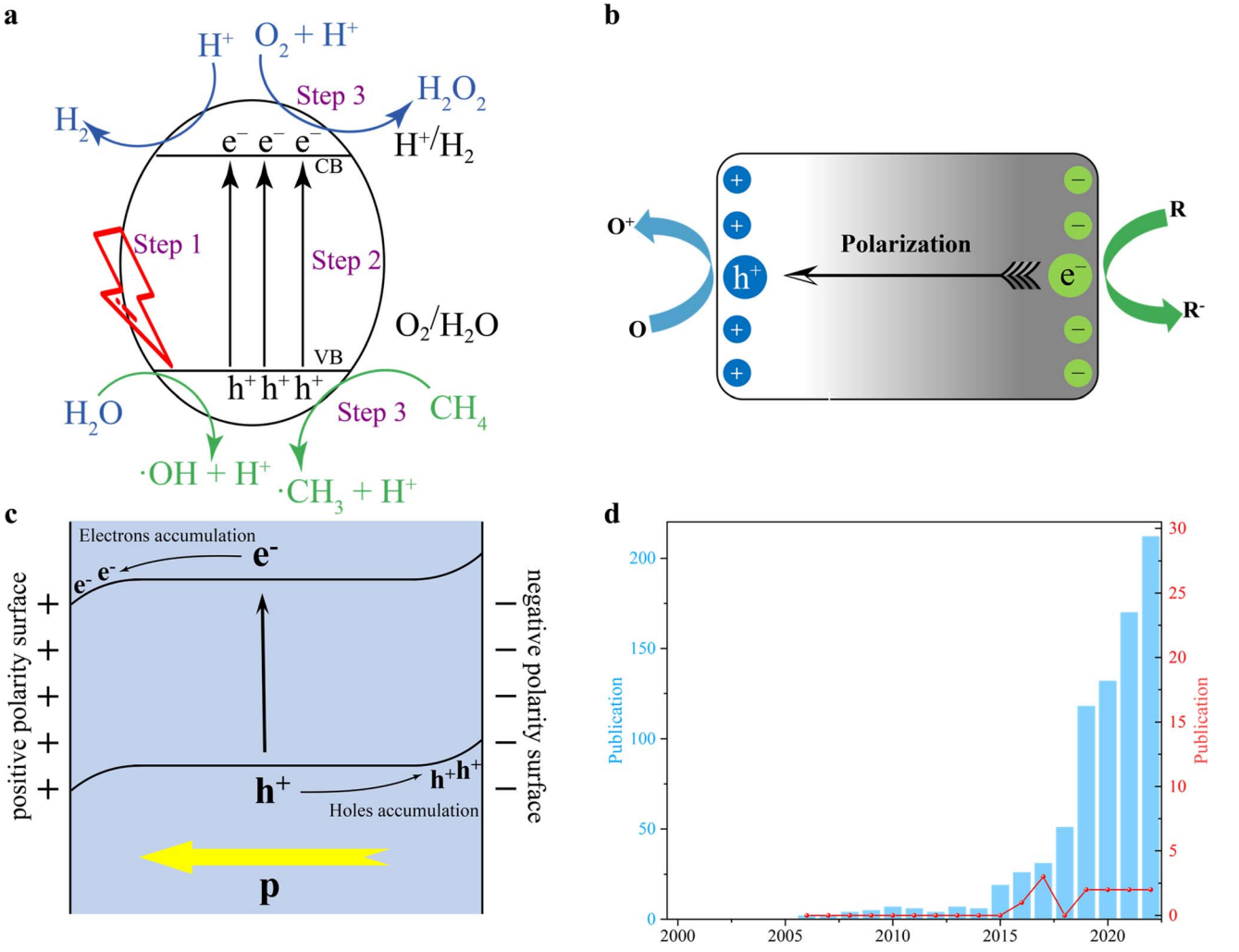

Fig. 1 (a) Three basic steps of photo-driven catalytic reactions. Step 1: inducing photoexcited electrons and holes; Step 2: charges migration; Step 3: photo-driven redox reactions. (b) An illustration showing the impact of the polarization effect in the separation of charge carriers and subsequent redox reactions. (c) The band bending phenomenon in ferroelectric photocatalysts owing to polarization effect. (d) The blue bar chart is publications of ferroelectric, photocatalysts according to the search result in "Web of Science". Key words: "photocatalysis" and "ferroelectric". The red curve is "publications of photocatalytic methane conversion *via* ferroelectric photocatalysts".

symmetric structure of the ferroelectric crystal, causing the materials to lose their ferroelectricity. The built-in electric field associated with the asymmetric domain wall (DW) polarity in ferroelectric materials facilitates the vectorial migration of photoexcited charge carriers (Fig. 1b).[56–61] In addition, by controlling the polar facets, ferroelectric materials are able to further improve the ability of reactant adsorption and product desorption.[41,62,63] Also, the selectivity of products as one of the most important factors for highly efficient photocatalytic methane conversion is adjusted by polarity switching at DWs.[63,64] More importantly, the adsorbed reactants at specific active sites can generate several intermediates and charges with different polarity properties. In this case, their accumulation will lead to the band bending in different directions (Fig. 1c).[65] Specifically, the positive polarity always caused an electron accumulation and thus a downward band bending. This can promote the flow of electrons and restrict hole movement.[66,67] Conversely, the surface with negative polarity should lead to an upward band bending, since there is an electron depletion layer. Obviously, in this case, the electron transfer will be difficult and hole transfer is accelerated owing to the different concentrations of charges on both sides of the interface.[68,69] Accordingly, the controllable properties of charge transfer in ferroelectric materials are beneficial for photocatalytic redox reactions with methane conversion no exception. Among the extensive library of ferroelectric materials—which can be mainly divided into three families, *viz.* inorganic, organic, and organic–inorganic hybrid ferroelectrics—inorganic and organic–inorganic hybrid ferroelectrics made of perovskite and its halide derivatives show, simultaneously, strong spontaneous polarization and optoelectrical properties.[70–72] Thus, special interest has been focused on the implementation of perovskite-based ferroelectrics for photocatalytic approaches.

Although many publications on ferroelectric-assisted photocatalysis have been recently reported, there are fewer works on their implementation for photocatalytic methane conversion applications to advance toward the efficient production of value-added chemicals and energy sources (Fig. 1d). Therefore, this review aims to provide a comprehensive tutorial about the recent progress in ferroelectric-assisted photocatalytic methane conversion, pointing out the remarkable materials and merits of the most common CH_4 conversion technologies. Finally, the main challenges in this emerging field and the corresponding solutions are listed. All in all, this review is hoped to provide in-depth insights to encourage the scientific community to further explore ferroelectric materials as potential photocatalysts for their implementation in the field of energy conversion in general, and methane conversion in particular.

2. Routes for photocatalytic methane conversion

2.1. Prominent semiconductors for photocatalytic methane conversion

Before reviewing the fundamental reaction mechanisms and key studies on different photocatalytic methane conversion strategies, it is essential to first introduce prominent examples of semiconductor photocatalysts capable of facilitating this conversion. Among the broad spectrum of semiconductor materials, two main families stand out due to their stability under redox catalytic reactions:[73–75] metal oxides and nitrides. Indeed, the intrinsic properties of these materials are crucial for understanding why the C–H bond in CH_4 can be cleaved photocatalytically (see Fig. 2).

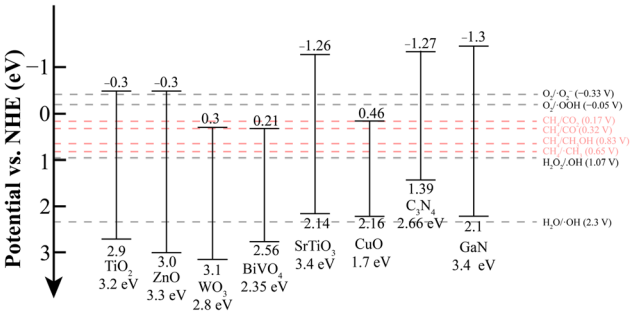

Fig. 2 Energy band structures of semiconductors and the redox potentials of reactants and active species.

2.1.1. Metal oxides. As some of the most conventional semiconductors, several metal oxides exhibit large band gaps, which suggest strong redox capabilities for complete photocatalytic methane conversion reactions (Fig. 2).[76] For instance, the suitable CB and VB positions exhibited by TiO_2 and ZnO have been widely studied for both indirect and direct photocatalytic methane conversion process.[16–19,77] From a selectivity perspective, WO_3 (ref. 78) and $BiVO_4$ (ref. 79 and 80) are potential semiconductors to preferentially forming CH_3OH owing to their CB positions are positioned just between the redox potential of CH_4/CO and CH_4/CH_3OH.[81,82] Moreover, $SrTiO_3$ and CuO are potential candidates to obtain high-value-added chemicals; however, their energy band structures are defective.[83,84] To address this issue, surface/energy band engineering is widely utilized.[85] Alternatively, introducing high temperatures to promote CH_4 activation has also shown to be a feasible strategy.[86] Another key aspect to be considered is the ability of the employed photocatalyst to adsorb/desorb the substrate. In particular, porous semiconductor materials, such as SiO_2 (ref. 87) and zeolites[88] have been shown to boost the photocatalytic methane conversion reaction by not only taking advantage of their large surface areas and abundant active sites but also accommodating alternative metal oxide semiconductors, such as Ga_2O_3.[89]

2.1.2. Nitrides. Research on nitride-based photocatalytic methane conversion systems has primarily focused on carbon nitride (C_3N_4) derivatives. Due to their polymeric properties, a diverse range of C_3N_4 materials with tailored properties have been prepared by selecting different monomer precursors for their synthesis.[90] Additionally, their photocatalytic ability has been further modified through the incorporation of different metal nanoparticles.[91] Relevant examples include Ru/Zn-modified C_3N_4 for CH_4 coupling with CO_2,[92] La-modified C_3N_4 with tube shape for DRM[93] and POCM,[94] and Cu-modified C_3N_4

for CH_4 oxidation to CH_3OH.[95] Interestingly, the interaction between Cu and C_3N_4 on Cu-modified C_3N_4 also allowed the conversion of CH_4 into ethanol (CH_3CH_2OH) *via* the combination of $-CH_2-OH$ on Cu atoms and $-O-CH_3$ on C atoms. Another potential nitride for methane conversion is GaN, which has demonstrated benzene production under UV light irradiation.[96] Specifically, Si-doped GaN nanowires, characterized by n-type semiconductor properties, have exhibited good selectivity toward benzene (96.8%), with an evolution rate of 0.019 μmol h^{-1}. However, the limited number of studies on GaN limits the understanding of the reaction mechanism on its surface. To date, a key challenge in nitride-based materials is that replacing O atoms with N atoms broadens the light response range, but the energy band structures of the resulting metal nitrides may not be optimal for methane conversion. Therefore, achieving a balance between enhanced optical properties and strong redox capabilities remains a crucial issue to be addressed.

2.2. Indirect methane conversion

Indirect methane conversion pathways encompass the oxidation of CH_4 to syngas through either SRM or DRM technologies, in which the resulting mixture of CO and H_2 serves as the precursor for their subsequent conversion into upgraded products. Generally, SRM utilizes steam (H_2O) to produce syngas according to the formula $CH_4 + H_2O \rightarrow CO + 3H_2$,[97] DRM involves the reaction of CH_4 with CO_2 by following the formula $CH_4 + CO_2 \rightarrow 2CO + 2H_2$.[55]

2.2.1. Steam reforming of methane (SRM): mechanism and kinetics. Indirect methane conversion technology still attracts much attention, because of the reforming ability that convert the CH_4 into syngas including CO and H_2, which can be further used as a fuel to produce downstream chemicals of significant economic value (*e.g.*, methanol, butanal, and kerosene).[98] These products from the downstream process could be important raw materials for high-value-added industrial products, such as plastics from methanol *via* formaldehyde as intermediate,[99] biodiesel precursor from butanal *via* catalytic hydroxy alkylation/alkylation reaction,[100] and aviation kerosene from long-chain alkanes *via* Fischer–Tropsch.[101] Therefore, with abundant CH_4 and so many CO_2 sources, such as fossil fuel combustion or agricultural waste, their consumption and reuse are promising to sufficiently supply the chemical industry.[102,103]

Since the high H/C ratio of CH_4 among hydrocarbons, SRM is a reliable technology to provide hydrogen energy at high operating temperatures.[104] In brief, in the presence of CH_4 and water, hydrogen production can be produced as shown in eqn (2-1). And some oxygenated products like CH_3OH can also be directly formed by SRM through another reaction pathway shown in eqn (2-2). SRM is an endothermic reaction, which is always operated at temperatures of >700 °C, indicating that the catalysts for SRM should be stable under high-temperature conditions.[105]

$$CH_4 + H_2O \rightarrow CO + 3H_2 \quad (2\text{-}1)$$

$$CH_4 + H_2O \rightarrow CH_3OH + H_2 \quad (2\text{-}2)$$

Several excellent works have tried to construct kinetic models for specific reaction conditions. Because of the endothermic nature, the fast transfer of both heat and mass is important to a highly efficient SRM process. In traditional industrial SRM reactors, the heat energy always is transferred from the furnace to the tube reactor, resulting in rapid reaction rates and thus very low effectiveness factor (η), compared to the diffusion rate of reactants and products over pellet-type catalysts.[105] Abbas's group simulated and studied the SRM process based on a one-dimensional (1D) theoretical model.[106] Theoretically, the activation energy for SRM was 257.01 kJ mol^{-1}. High temperature, low pressure, and high H_2O/CO_2 ratio contributed to rapid CH_4 conversion and high purity of H_2. This work is consistent with the previous report from Xu *et al.*, also showing a low η (<0.03) when using a small portion of catalyst in industrial-scale conditions.[107] An early theoretical work studying the influence of SRM reactors on kinetics has also been investigated.[108] Two computational fluid dynamics (CFD) models were developed for simulating the steam reforming and combustion of methane in microchannel reactors. The models included 20 mm in length and 0.7 mm side with 4 or 20 square microchannels. The results illustrated that the gaseous reactants were heated isothermally so that the complete CH_4 combustion occurred at the channel entry within a short distance. The cross-flow disposition led to 80 °C of maximum temperature differences and an easier feed stream distribution, which was beneficial for the rapid reaction kinetics. In addition to the unique reaction vessels, the reaction temperature was also investigated from a kinetic perspective. Kechagiopoulos *et al.* clarified the reaction kinetics of SRM at low temperatures in conjunction with isotopic investigations.[109] Temperature-programmed experiments of CH_4 reforming and decomposition modes with isotopic investigations showed the cleavage of the C–H bond was the rate-determining step, but the steam-derived intermediates had a low influence on the whole reaction rate. The authors also proposed a thermodynamically consistent microkinetic model with the consideration of several surface pathways, indicating that $-CH_3$ dehydrogenation on the catalyst surface could also limit the reaction rate.

Although SRM has become a mature industrial technology for obtaining hydrogen fuel, it still has several disadvantages such as mass/heat transfer and carbon deposition (coking). Coking often blocks reactors or breaks catalyst particles so as to cause deactivation. Experimentally, when the ratio of steam to carbon (S/C) is lower than 1, rapid and severe coke will inevitably occur.[110] Meanwhile, the high temperature and pressure are also related to the carbon deposition problem.[111] In the process of SRM industrialization, researchers try to use a high S/C ratio (2.5–3.0) to avoid the coke deposition and catalyst deactivation problem. However, the excessive partial pressure of steam reduces energy efficiency. In order to develop catalysts with high stability, the Boudouard reaction (including CH_4 and CO cracking) should be considered to suppress coke formation. Additionally, the ratio and selectivity of products from SRM also need to be further controlled. In this case, the catalytic transformation of CH_4 and CO_2 into syngas *via* DRM might be an ideal alternative technology to SRM. DRM has the potential

ability to achieve real carbon neutrality *via* the conversion of solar energy to chemical energy and mitigate the greenhouse effect. Considering the fact that the study about ferroelectric-assisted SRM systems is still a blank field, the SRM will not be further discussed in this review article. Some excellent works have comprehensively summarized and discussed the traditional thermal and advanced photo(thermal) catalytic SRM implementations. Interested readers are recommended to read ref. 97 and 112.

2.2.2. Dry reforming of methane (DRM): mechanism and kinetics. Comparing SRM (eqn (2-1)) and DRM (eqn (2-3)), DRM is particularly attractive because it uses two abundant greenhouse gases as feedstocks. However, this technology is also because of its inherent endothermic nature and the deactivation during the process triggered by carbon deposition at high-temperature conditions.[113] One of the advantages of the DRM process is the high energy efficiency compared to SRM, since SRM uses water as feed gas, meaning lots of energy has to be used to evaporate the water.[98] In DRM reactions, the feed reactants are gaseous, indicating that the energy could be entirely involved in redox chemical reactions rather than physical evaporation as in SRM. And during the DRM process, the flow rate and ratio of reactants are easily controlled. Importantly, DRM has a higher CO/H_2 ratio (1 : 1) than SRM (1 : 3). Thus, further downstream processes are contributed by the CO-rich syngas from DRM.[114]

$$CH_4 + CO_2 \rightarrow 2CO + 2H_2 \quad (2\text{-}3)$$

Generally, both traditional thermal catalysts and photocatalysts tend to activate reactants (CH_4 and CO_2) *via* a bifunctional route: (i) after CH_4 is absorbed on reduction sites, dehydrogenation will occur (Fig. 3a). However, during the CH_4 activation step, the cracking of the strong CH_3–$H_{(g)}$ bond is very difficult because of the high binding energy (439.3 kJ mol^{-1}), meaning the first step of CH_4 dissociation is one of the rate-determining step (DRS).[115] Regarding the CO_2 molecules, as shown in Fig. 3b, they can be specifically adsorbed on three different reactive sites involving the metal (cocatalyst) surface, metal–support interface, and support. Although the conversion of CO_2 to CO or carbonate precursors is simple and direct,[116–118] the intrinsic properties of CO_2 like non-polarity and thermodynamic stability lead to robust C=O bond with ~750 kJ mol^{-1} of dissociation energy barrier. From the thermodynamic view, the activation of CO_2 with high energy input is another RDS factor.[103,119] Further, the strong chemical bonds in CH_4 and CO_2 make a high-temperature condition (>800 °C) necessary during the conventional thermal catalytic DRM process, resulting in the unavoidable sintering and carbon deposition on transition metal-based catalysts.[120–122] It has been confirmed that the photocatalytic DRM can be carried out at low temperatures using semiconductor photocatalysts, which may be an effective strategy to avoid sintering and coking of catalysts.[123]

For the kinetic studies, several kinetic models have been proposed based on different adsorption states of the reactants, so that the rate-determining step (RDS) could be studied in different DRM systems. Here, three mainstream kinetic models for predicting the reaction rates are presented.

(1) Power-law model: the power-law model was constructed to provide reaction parameters without including reaction mechanisms. This kinetic model only assumed one situation, in which catalyst surfaces tend to adsorb more CH_4 instead of CO_2 so that the CH_4 adsorption dominated the whole reaction. Thus, the parameters from this simple model are rough and sometimes are not consistent with the actual experimental results.

(2) Eley–Rideal (ER) model: the ER model investigated the DRM kinetics in the temperature range of 700–850 °C with the pressure ratio of CH_4 to CO_2 was 1. Besides, other competitive or reverse reactions were also taken into consideration.[124] In this model, only one reactant (CH_4 or CO_2) is adsorbed on the catalyst surface to interact with another unadsorbed gaseous reactant. The ER model showed that both conversion processes, CH_4 to H_2 and active carbon (C) to CO ($C + CO_2 \rightarrow CO$), determine the reaction rate.

(3) Langmuir–Hinshelwood–Hougen–Watson (LHHW) model: although the ER model has considered a lot of factors including crucial parameters and common side reactions, the LHHW model is more accurate because the mechanistic steps in the LHHW model are consistent with practical experimental conditions and results.[125] The greatest difference between LHHW and other models is that in the LHHW model, two reactants should be adsorbed on actives at the same time. In this case, the LHHW model regards both activation and cracking processes as the RDS. And another step is thermodynamic equilibrium. The LHHW model is proposed based on the activation process of two reactants and the interaction between CH_x and O, which finally generates the desired syngas product. It has been confirmed that CH_xO as an intermediate could be rapidly dissociated to CO and H_2.[126] However, water was always detected even though no water or steam was present in the initial reactants owing to the unavoidable RWGS (reverse water–gas shift) side reaction.[98] Fortunately, although a small amount

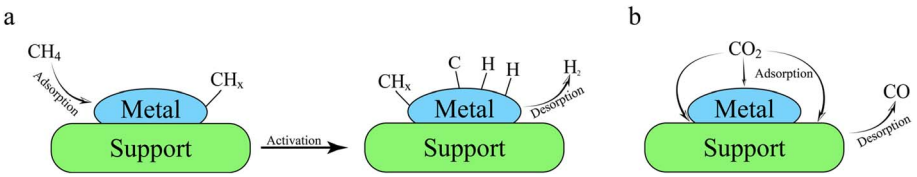

Fig. 3 Illustration of reactants activation during DRM process: (a) CH_4 adsorption and dissociation (cracking), generating H_2 product. (b) CO_2 adsorption on three different active sites including metal surface, metal–support interface, and support, and then direct generation and desorption of CO within one step.

of water had a slight effect on the ratio of syngas (H_2 : CO), the RWGS with water generation leads to more CH_xO active species and thus the yield rate of syngas.

2.2.2.1. Thermal catalytic DRM. Considering the fact that many photo(thermal)catalysts have been developed based on previous investigations of mature thermal DRM technology, some common thermal catalysts for conventional DRM reactions should be introduced before showing the advantages of ferroelectric-assisted photocatalytic DRM technology. During the thermal catalytic process, the selection of catalysts is important to achieve long-term and high conversion efficiency of methane. Although the cost of catalysts cannot be neglected, noble metals (*e.g.* Rh, Ru, Pt, Ir, and Pd) could be considered as suitable candidates due to their high activity and stability under harsh conditions for the DRM process.[120–122] An early work reported a Ru/Al_2O_3 catalyst. Ru/Al_2O_3 exhibited 46% CH_4 conversion and 77% H_2 selectivity. Kinetic and temporal studies indicated that the Ru metals induced both CH_4 and CO_2 conversion processes. In addition, H and O species as intermediates were continuously provided by the Al_2O_3 substrate, so that catalyst aging (or active Ru oxidation) could be inhibited. Another example is the Ru-loaded lanthanum oxide (Ru/La_2O_3) for DRM application published by Cornaglia and co-workers.[127] Ru/La_2O_3, which showed ~15% conversion efficiency of CH_4, had excellent stability for more than 80 h at high temperatures (823–903 K).

Furthermore, when considering industrial production, other requirements have been proposed, such as maintaining high activity while reducing the cost of catalysts, or achieving high stability and efficiency at the same time. In this case, transition metals have 3d orbitals with unpaired d-electrons. Especially, Ni-based catalysts have become the best choice owing to their low cost, high adsorption energy towards O and C atoms, and excellent activity for DMR.[128–130] However, the strong cracking process of CH_4 over Ni surface always leads to carbon deposition ($CH_4 \rightarrow C^* + 4H^*$), which can cover the active sites on the catalyst surface and finally result in inactivation. Because long-term stability is also pivotal for catalyst industrialization, several advantages have been proposed to improve the stability of Ni-based catalysts. For instance, the fabrication of bimetallic thermal catalysts has been used in Ni-based catalysts.[131–133] The Ni-based alloy can resist carbon formation than single Ni.[134] Zhang *et al.* reported $Ni_xAl_1O_{2-\delta}$ mesoporous catalyst.[135] The oxygen vacancy formed by the partially inverted structure of $NiAl_2O_4$ spinel can be used to activate CO_2. Then CO_2 reacted with deposited carbon atoms to avoid carbon deposition so that the stability was improved up to 50 h at 800 °C. Besides, in recent years, it has been reported that the position of carbon atoms could be tailored in interstitial or surface sites in/over Ni crystalline.[136] And the interstitial atoms affect the electronic properties of surface atoms, further adjusting the catalytic behaviour. This provides a new idea to eliminate carbon deposition. In addition to reactants activation and long-term stability, other factors also determine the activity and selectivity of DRM implementation. Several works have discussed the impact of important factors in the DRM efficiency and product selectivity.[137–139] However, the photocatalytic DRM systems did not get enough attention from the past works.

2.2.2.2. Photocatalytic DRM. Photocatalysis can reduce the harsh conditions of the traditional thermal DRM process by taking advantage of light illumination, as the energetic photo-excited charges effectively dissociate the C–H and C=O bonds and prevent carbon deposition under mild conditions instead of high temperature and pressure conditions to maintain the activity of the catalysts after several cycles.[140–143] However, low-energy photons can hardly be used to directly excite photocatalysts to trigger reactions, so the infrared light energy has been overlooked for a long time.[39,40,144] The photothermal DRM approach has led to an increase in DRM activity by integrating solar energy and thermal energy in the same reactor,[145–147] and more studies have attempted to utilize both light and thermal energy from light irradiation to further improve the conversion rate of CH_4. A representative work is the one reported by Shoji and co-workers employing $SrTiO_3$-supported rhodium catalyst (Rh/STO).[86] During DRM experiments, the limit of thermal catalytic DRM over Rh/STO was determined, suggesting the maximum H_2 generation under dark and high-temperature conditions (Fig. 4a). However, under light irradiation without external thermal energy input, Rh/STO could overcome the limitation in the thermal system even at a mild temperature. On the other hand, no H_2 could be detected from bare STO, meaning Rh was an important active centre for photothermal catalytic DRM. Rh remained at 1–2 nm of particle size before and after the DRM, indicating that there was no aggregation of Rh particles (Fig. 4b and c). And no carbon deposition was detected by STEM images. Thus, catalytic DRM with light energy as the only input energy source effectively enhanced the longevity of catalyst *via* inhibiting aggregation and coking. The charge transfer pathway during the DRM reaction was discussed by *in situ* EPR measurements. Trapped hole peaks in the VB were clearly observed under light irradiation (Fig. 4d). However, the trapped electrons in the CB were not obtained in Rh/STO, suggesting that the photoexcites electrons were injected into Rh. In N_2, CO_2/CH_4 or CH_4 atmosphere, the signal intensity of the hole decreased, indicating that the holes reacted with CH_4 instead of CO_2 (Fig. 4e). The subtract potential profile from Kelvin probe force microscope (KPFM) analysis implied that the electron could transfer from STO to Rh due to the gap in their Fermi levels (Fig. 4f–h). According to isotopic trace analysis, in the Rh/STO catalyst, the lattice oxygens (O_2^-) acted as mediators to drive DRM instead of protons. Thus, CH_4 was selectively oxidized by surface lattice oxygen ions of STO, while CO_2 was reduced by photoelectrons from STO over Rh particles, avoiding the recombination of charge carriers in the interior of STO (Fig. 4i).

Photo(thermal) catalytic DRM technology realizes a highly efficient CH_4 conversion under mild conditions because it can overcome the thermodynamic energy barrier with external light energy input and assistance.[148,149] From this perspective, the charge-carrier recombination instead of CH_4/CO_2 activation will become the main challenge for the whole DRM process, since the random collision of electrons and holes will be aggravated by high-temperature conditions from external heating or light

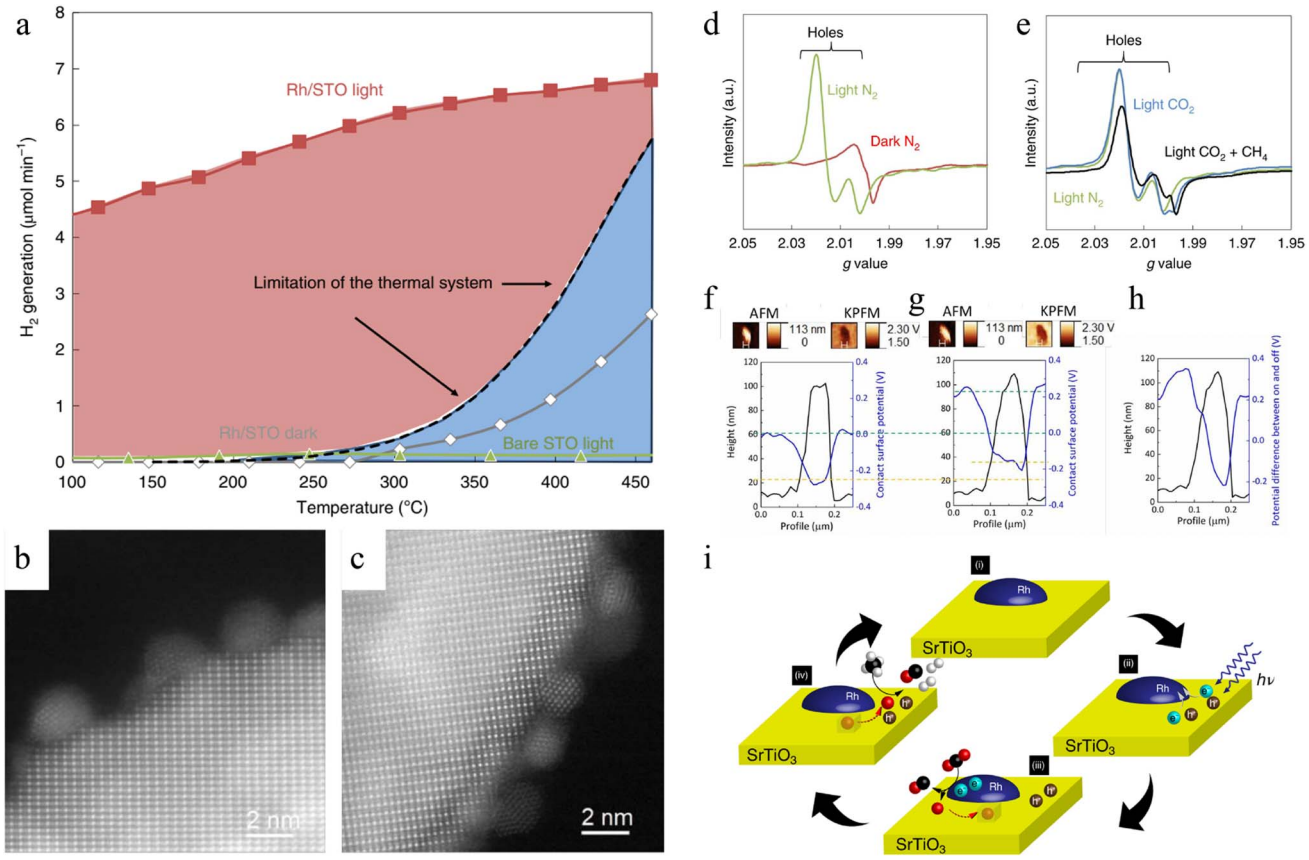

Fig. 4 (a) H_2 evolution efficiency and the limitation of the thermal DRM system. Reaction conditions: 150 W Hg–Xe lamp, 1% CH_4 and 1% CO_2 mixture in argon balance gas (4.5 μmol min^{-1}). HAADF-STEM images of Rh/STO (b) before and (c) after DRM. ESR spectra of Rh/STO (d) in an N_2 atmosphere; (e) in N_2, CO_2, or CH_4/CO_2 atmosphere. KPFM analysis of Rh/STO (f) before and (g) during UV light irradiation, and (h) potential difference between light-on and light-off conditions. (i) Charge carriers and oxygen ions transfer mechanisms.[86] Copyright © 2020, Springer Nature.

illumination.[38] The collision of electrons and holes leads to their recombination and the waste of the captured photon energy before the charges take part in the photo(thermal) catalytic redox process.[150,151] In this case, ferroelectric materials are able to inhibit the photoinduced charge recombination and promote charge transfer by constructing a built-in electric field during the photo(thermal)catalytic DRM process.

2.3. Direct methane conversion

Direct methane conversion technologies, including POM, OCM, and NOCM, rely on converting methane into added-value products without the need of producing syngas as intermediate fuel.[152] Thus, these technologies are especially appealing when compared to traditional indirect methane conversion approaches since reduce energy consumption, improve selectivity, and minimize greenhouse gas emissions.[153]

2.3.1. Partial oxidation of methane (POM): mechanism and kinetics. Another major and well-established reaction route is the partial oxidation of methane (POM), which consists of the combustion of methane to produce syngas or methanol, which can be further utilized for the production of olefins, middle distillates, acetic acid, *etc.*[154] Thus, POM holds the ability to supply to the downstream fine chemical industry.[155] Different reaction mechanisms of POM *via* homogenous and heterogenous catalysts have been proposed. In detail, for homogeneous catalysts, the metal centres are always considered as active sites for C–H activation by several methods (*e.g.* oxidative addition, metal-radical activation, 1,2-addition over the metal centres, *etc.*).[156,157] On the other hand, in heterogeneous systems, there are two main transition statuses involving $^{\bullet}CH_3$ radicals or M–CH_3.[158] The CH_4 activation has two processes including dehydrogenation and deprotonation of C–H. In the dehydrogenation process, a hydrogen atom is separated from CH_4 by M–O or other active electrophilic oxygen atoms and then forms $^{\bullet}CH_3$ and $^{\bullet}OH$ radicals as a transition state (Fig. 5).[156,159] In the deprotonation process, this mechanism involves the generation of CH_3^- and H^+ by the dissociative adsorption of CH_4.[160,161] The CH_3^- coordinates to the catalyst surface and forms an M–C σ-bond *via* oxidative addition, electrophilic activation, and σ-bond metathesis. H^+ interacts with the metal sites/O species in heterogeneous catalysts and molecules/ligands in homogeneous catalysts.[161–163] Under these conditions, the carbon centre will always maintain a formal oxidation state (FOS) showing a tetrahedral geometry with sp^3 hybridization during the formation of reaction intermediates.[161] The FOS of the carbon

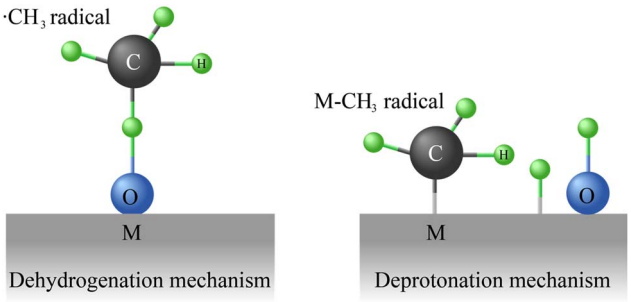

Fig. 5 Dehydrogenation and deprotonation mechanism for CH_4 activation during POM reactions.

centre is not changed, confirming that the methane activation step is an acid-based reaction according to the deprotonation mechanism, suggesting that the deprotonation tends to occur in some homogeneous systems with highly polar solvents (*e.g.* H_2O or concentrated acids).[156] In addition to two aforementioned mechanisms, free radicals (*e.g.* ·OH from the Fenton reaction) can initiate the POM reactions,[164] and plasma has also been used to oxidize CH_4 to various C_1 species.[165] The high stability and thermodynamic inertness of CH_4 also make the oxidation reaction an extremely difficult task. The conventional industrial thermocatalytic POM processes require high temperature (700–1000 °C) and pressure (2.5–3.5 MPa), which can cause the oxidation of catalysts and non-negligible risk of explosion due to the presence of O_2.[155] To overcome the possible hazards during POM, photocatalytic technology once again becomes a promising strategy once again to complete POM under mild conditions, reducing energy consumption, and largely avoiding coke formation and sintering.

Several studies have discussed the kinetic model of POM over different catalysts. An early study elucidated the kinetics of the catalytic reactions over Pt catalysts,[166] where the apparent activation energy of CH_4 and O_2 conversion is only 10 kJ mol^{-1}, suggesting that the POM reaction is not temperature dependent, but completely determined by the transport behavior. Due to the excess of CH_4 in this system, the efficiency of oxygen consumption, which is strongly influenced by mass transfer to the surface, appears to have become the RDS. However, the selectivity of the products (*e.g.* CO and H_2) is strongly influenced by the temperature at the surface of the Pt catalysts.[167] In addition to the noble metal catalysts, a microkinetic model of the CH_4 oxidation reaction over PdO catalysts was proposed based on DFT results under atmospheric to moderate pressures, rare fuel, and low-temperature conditions.[168] The adsorption of activated CH_4 *via* dehydrogenation step over unsaturated surface Pd–O site pairs (denoted as Pd_{cus}–O_{cus}) is a RDS during the initial stage of the POM reaction. Another focus of this work was the strong water-inhibiting effect, which persists up to high temperatures.[169] The water inhibition could be considered as hydroxide formation leading to reduced availability of the Pd_{cus}–O_{cus} site pairs. Thus, the presence of water vapor interacting with the catalyst particles was one of the main factors causing sluggish kinetics and even catalyst deactivation. Another kinetic model of Ni-based catalysts was also developed by comparing the numerical simulations with the experimental data in a flow reactor.[170] The results showed that the initial temperature for CH_4 conversion to CO_2 and H_2O was 723 K. However, there was no significant syngas evolution up to 880 K. At temperatures above 880 K, the formation of H_2 and CO was increased, resulting in an equilibrium composition with CO_2 and H_2O. This behaviour indicated the indirect reaction pathway of syngas formation *via* the initial generation of H_2O and CO_2 during the CH_4 oxidation process.[171–173] Thus, the competition between the first and second steps determined the efficiency of the overall POM reaction, meaning that the CO_2 dissociation and CO desorption were the RDSs for CO evolution at high temperatures. This review only shows some representative studies, including noble metal-/metal oxide-/transition metal-based catalysts and their kinetic models, which determine the reaction rate. More kinetic models of POM and discussion of reaction pathways over different catalysts have been well demonstrated by other comprehensive works and are therefore not shown in this review.[174–176]

2.3.1.1. Thermal catalytic POM. Various thermal catalysts using different oxidants for POM have been developed and reported over the last few decades. Early works used VO_x and MoO_x to convert CH_4 to formaldehyde (desired product) and methanol (by-product) at 450 °C.[177] The C–H bond activation over Pt and Pd sites has also been investigated *via* Periana's system using sulfuric acid (H_2SO_4) as the oxidant.[157] The H_2SO_4 oxidant stabilized the methyl bisulfate product so that Pt^{2+} complex-based catalysts achieved ~90% conversion and 81% selectivity. In addition to the noble metal-based catalysts, under mild conditions, zeolites with transition metal centres (*e.g.* Cu and Fe) could easily dissociate C–H bonds and were therefore developed for the oxidization of CH_4 with N_2O or O_2 as oxidant (Fig. 6a).[178,179] Metal zeolite was activated in O_2 at 450 °C but reacted with CH_4 without O_2 at 200 °C. This stepwise process avoided the over-oxidation of CH_4 at high temperatures (the first step) and thus achieved over 90% CH_3OH selectivity in the second step (Fig. 6b). In addition, metal oxide-based supports have also been extensively studied for POM reactions. Some reports showed the real implementations of oxide-based thermal catalysts such as SiO_2, Al_2O_3, MgO, ZrO_2, and CeO_2.[180–184] For example, the Ni-loaded CeO_2 catalysts were suitable for long-term POM at high temperatures, excellent redox capacity, and coke resistance behaviour. Bal *et al.* reported Ni/CeO_2 catalyst, which could activate and totally convert methane at 400 and 800 °C, respectively.[185] Due to the cooperation between Ni and CeO_2, Ni/CeO_2 could resist coke and produce syngas ($H_2:CO = 2$, Fig. 6c). Besides CeO_2, iron oxides were also investigated as oxygen carrier candidates,[186] but the oxygen species in iron oxide-based supports were too active to avoid the overoxidation of CH_4 to CO_2 and H_2O.[187] In addition, tungsten oxides (WO_3) showed their superior stability and selectivity for specific products (*e.g.* syngas).[188] However, one of the main challenges for WO_3 thermal catalysts has been poor reducibility, suggesting that a high temperature is required to utilize the lattice oxygen in WO_3 and initiate reactions.[189] Despite the above advances in POM applications, the high

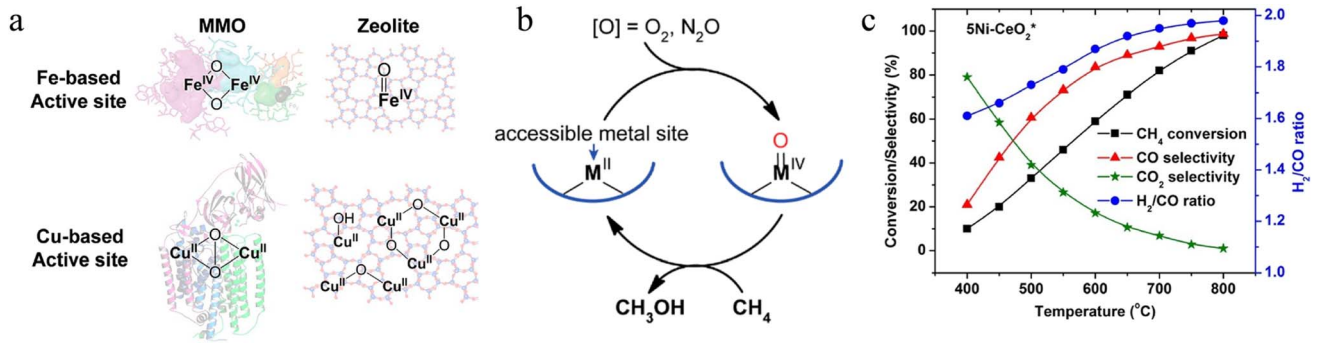

Fig. 6 (a) Active site in enzymes and zeolites with Fe or Cu atoms. (b) Conceptual activation of CH_4 at a high-spin high-valent metal-oxo species.[178] Copyright © 2018, American Chemical Society. (c) Selectivity of Ni–CeO_2 during POM reaction.[185] Copyright © 2016, Elsevier B.V.

stability and thermodynamic inertness of CH_4 also make the oxidation reaction an extremely difficult task. Conventional industrial catalytic POM processes require high temperature (700–1000 °C) and pressure (2.5–3.5 MPa), which can cause oxidation of catalysts and non-negligible explosion risks due to the presence of O_2.[155]

2.3.1.2. Photocatalytic POM. Many conventional semiconductor photocatalysts, such as TiO_2, WO_3, $BiVO_4$, *etc.*, have shown remarkable activity in CH_4 oxidation.[80,190,191] For example, Morante's group investigated the selectivity of $BiVO_4$ photocatalyst in the presence of nitrite ions.[192] The low concentration of nitrite was beneficial for the selective oxidation of CH_4 to CH_3OH. By reducing the free $^{\bullet}CH_3$ radicals, nitrite as a $^{\bullet}OH$ scavenger limited the subsequent undesirable oxidation process of CH_3OH, thus greatly reducing the formation of CO_2. Meanwhile, the nitrite ions could become a UV-filtering species, inhibiting water photolysis, which ultimately forms $^{\bullet}OH$. In this way, more than 90% selectivity towards CH_3OH could be achieved over $BiVO_4$ (Fig. 7a). As an ultrawide-bandgap semiconductor, strontium tantalate ($Sr_2Ta_2O_7$) with Pd nanoparticles has also been used to perform POM reactions under low-temperature conditions.[193] In this composite, O_2 could accept the electrons from $Sr_2Ta_2O_7$ to form radical species. In addition, the layered perovskite structure made $Sr_2Ta_2O_7$ has high stability for immobilizing Pd nanoparticles (Fig. 7b). The hot electrons from Pd nanoparticles facilitated the activation of O_2 and CH_4. The photothermal effect was triggered by hot carrier relaxation. Thus, light illumination lowered the initial temperature of POM reactions to below 423 K and improved the catalytic performance to below 873 K to produce syngas. Other previous research has also demonstrated the excellent ability of photocatalysis to reduce the large heat energy during the POM process over various semiconductor-based photocatalysts such as g-C_3N_4, TiO_2, and $CuMoO_4/SiO_2$.[94,194] In addition, the recombination between electron–hole pairs is an unavoidable defect in the photocatalytic process. Compared to some photocatalytic reactions with simple products (*e.g.* water splitting, organic degradation), the selectivity of POM products is also a major challenge due to the diversity of products. In this case, ferroelectric materials show their ability to overcome these problems.

2.3.2. Oxidative coupling of methane (OCM): mechanism and kinetics. The OCM technology is a new technology that directly converts methane to olefins without an intermediate process.[8,195] The OCM has relatively low-temperature reaction conditions and cleaner product distribution, so it has recently attracted wide attention for industrial production.[196] The OCM is generally considered to be a mixed catalytic and gas-phase process.[197–201] In principle, the reaction pathways of OCM involve three steps on the catalyst surface (Fig. 8).[196] First, CH_4 reacts with O_2 present in the feed to form $CH_3^{\bullet}$ radicals on the catalyst surface, which is a heterogeneous step. This is followed

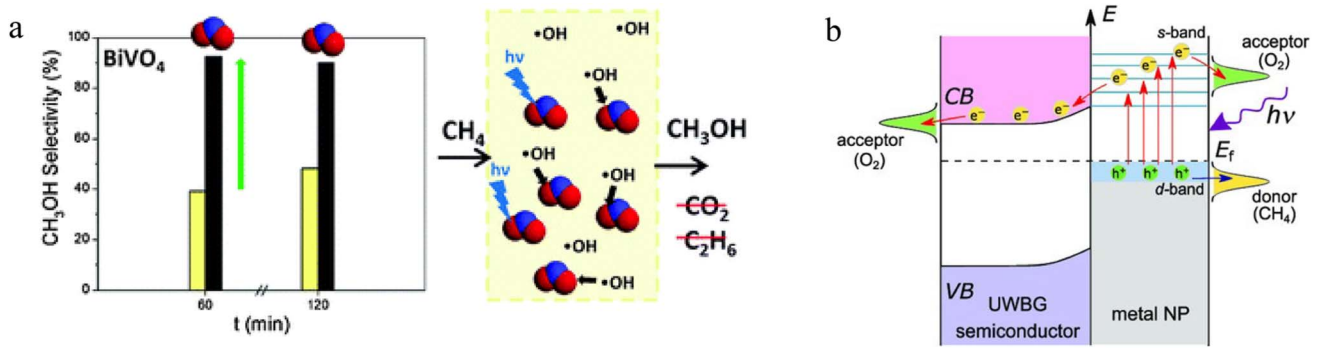

Fig. 7 (a) Selectivity for POM towards CH_3OH product. Reaction conditions: 450 W Hg lamp, 20% CH_4 in He (~22.4 mL min^{-1}), 55 °C.[192] Copyright © 2015, Royal Society of Chemistry. (b) Band alignment mechanism in a metal NP/semiconductor system.[193] Copyright © 2019, Wiley.

by a homogeneous step, during which $CH_3^{\cdot}$ is coupled to produce ethane (C_2H_6). Finally, the production of ethylene (C_2H_4) is achieved by subsequent dehydrogenation of C_2H_6. During these steps, one of the difficulties is the energy required to dissociate the strong C–H bond (~438 kJ mol^{-1}), which is also present in other CH_4 conversion technologies, suggesting that a sufficiently low activation energy barrier is required for the generation of $CH_3^{\cdot}$ radicals and the subsequent coupling or dehydrogenation process.[202] Overcoming the thermodynamic barriers often requires the introduction of O_2 and high temperatures, which leads to the production of unwanted products, such as CO_2 and graphitic carbon.[85] In addition, C_2H_4 is more unstable than CH_4, so consecutive oxidation of C_2H_4 is also a major challenge.[203,204] Moreover, it is difficult to achieve efficient CH_4 conversion while maintaining high selectivity for C_2 products, because the complete and partial oxidation of methane to CO_x and the combustion of C_2H_6 and C_2H_4 can occur simultaneously. Thus, the low selectivity and evolution rates of C_2 products are major challenges for large-scale utilization.

The actual reaction steps can be more complex than the theoretical three basic steps because both gas phase and catalyst surface reactions should be considered simultaneously to discuss the kinetic models and the RDSs.[205–207] However, the currently proposed kinetic models are still incomplete and not able to fully explain the obtained experimental data.[208,209] However, two typical assumptions based on the absence and presence of catalysts have been studied, leading to the development of many kinetic models in different catalytic systems. A representative kinetic scheme reflecting the OCM reaction under gas-phase conditions without heterogeneous catalysts has been demonstrated.[210] According to this kinetic model, the time dependence of the compound concentrations could be calculated, thus determining the product selectivity as a function of the degree of conversion. Specifically, when there was an excess of CH_4 in the gas phase, the concentration of active oxygen species interacting with $CH_3^{\cdot}$ to form carbon oxides was low, resulting in a high selectivity for C_2 hydrocarbon products. In contrast, under high O_2 concentration conditions (*e.g.* CH_4 : O_2 = 2), the formation of oxygen-containing radicals such as $HO_2^{\cdot}$ and $^{\cdot}OH$ was promoted, leading to the low evolution rate of C_2 hydrocarbon products. The authors summarized the optimum reaction conditions for achieving the maximum selectivity of C_2 products. The reaction temperature should be 1000–1100 K, and the pressure *ca.* 10 bar while the ratio of CH_4 to O_2 was not less than 5–7. A total pressure higher than 10 bar was advantageous to produce the primary product C_2H_6 instead of the desired C_2H_4. A lower ratio between CH_4 and O_2 would make the non-selective reaction dominant. Based on the above study, further work has been carried out through dedicated experimental measurements, regression, sensitivity, and parameter contribution analyses were carried out to explore the optimal OCM reaction conditions.[198,211–213] An interesting paper by Simoní Da Ros and co-workers summarizes some details of these works.[208] In short, the updated kinetic model of OCM gas phase reaction systems has contributed to the optimization of the reaction parameters, and thus the operation of the product distribution.

For the kinetic model in the presence of catalysts, Stansch *et al.* described a 1D homogeneous plug flow model comprising 10 reaction steps according to the experimental data over a La_2O_3/CaO catalyst with high activity and selectivity towards C_2 hydrocarbons in a packed bed reactor.[207] An important assumption in this kinetic model was the small effect in gas phase reactions, meaning that only a few cases where the gas phase reaction can be neglected, such as short contact time and low gas volume, were suitable for this model. Despite this drawback, the dynamics of the oxidative reaction were successfully represented by Hougen–Watson-type rate equations (eqn (3-1)). The power law rate equations determined the rates of dehydrogenation, C_2H_4/H_2O reforming, and the WGSR (water–gas shift reaction, eqn (3-2) to (3-5)). The effects of O_2 and CO_2 on enhancing C_2H_4 selectivity *via* inhibiting C_2H_6 were also described (eqn (3-6)).

$$r_j = \frac{k_{0,j}\, e^{-E_a/RT} p_c^{m_j} p_{O_2}^{n_j}}{\left(1 + K_{j,CO_2}\, e^{-\Delta H_{ad,CO_2 j}/RT} p_{CO_2}\right)} \quad (3\text{-}1)$$

$$r_1 = k_{0,1}\, e^{-E_{a,1}/RT} p_{C_2H_6} \quad (3\text{-}2)$$

$$r_2 = k_{0,2}\, e^{-E_{a,2}/RT} p_{C_2H_4}^{m_2} p_{H_2O}^{n_2} \quad (3\text{-}3)$$

$$r_3 = k_{0,3}\, e^{-E_{a,3}/RT} p_{CO}^{m_3} p_{H_2O}^{n_3} \quad (3\text{-}4)$$

$$r_4 = k_{0,4}\, e^{-E_{a,4}/RT} p_{C_2H_4}^{m_4} p_{H_2O}^{n_4} \quad (3\text{-}5)$$

$$r_5 = \frac{k_{0,5}\, e^{-\frac{E_{a,5}}{RT}} \left(K_{0,O_2}\, e^{-\Delta H_{ad,O_2}/RT} p_{O_2}\right)^{n_5} p_{CH_4}}{\left[1 + \left(K_{0,O_2}\, e^{-\Delta H_{ad,O_2}/RT} p_{O_2}\right)^n + K_{j,CO_2}\, e^{-\Delta H_{ad,O_2}/RT} p_{O_2}\right]^2} \quad (3\text{-}6)$$

where $E_{a,L}$ is the activation energy (J mol^{-1}), $\Delta H_{ad,CO_2}$ is the adsorption enthalpy for CO_2 (J mol^{-1}), $\Delta H_{ad,O_2}$ is the adsorption enthalpy for O_2 (J mol^{-1}), $k_{0,L}$ is the pre-exponential factor, $K_{0,L}$ is the adsorption constant (Pa^{-1}), n is the number of

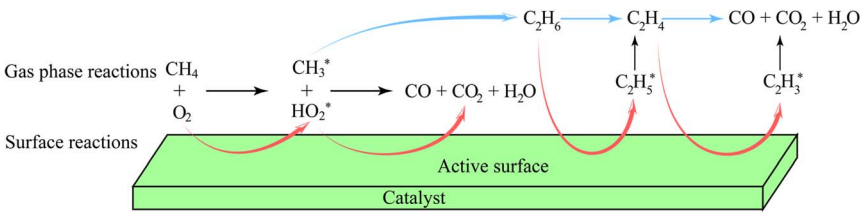

Fig. 8 OCM reaction steps in the gas phase and over the catalyst surface.

experiments, n_j is the reaction order, p is the partial pressure (Pa) and R is the gas constant (J mol^{-1} K^{-1}). The author emphasized that the proposed kinetic model could be used for all reaction steps over other OCM catalysts with similar properties involving basic carrier and non-reducible catalytic components. According to the above kinetic model, other updated models considering the gas-phase reactions were proposed later.[214–217] These works included at most 39 gas-phase reactions, which played important roles in explaining the selectivity of products, the inhibiting effect of excess O_2, and the prediction of OCM reactors.

2.3.2.1. Thermal catalytic OCM. Considerable efforts have been made to develop catalysts for OCM to C_2 hydrocarbons. For thermal catalysts, an early result was reported by Ito *et al.*, who developed a lithium-doped magnesium oxide (Li/MgO) catalyst that had a high activity for the formation of $^{\bullet}CH_3$ radicals in the presence of O_2, resulting in high selectivity for C_2 compounds (C_2H_4 and C_2H_6) and 28% conversion of CH_4.[218] Cu- and Fe-contained zeolite thermal catalysts have been widely studied with their dehydrogenation mechanism. For example, the Cu-/Fe-based catalysts have been used for OCM using N_2O or H_2O_2 as strong oxidants.[219,220] The Cu–O–Cu sites have been confirmed as the main active platform to activate CH_4 *via* hydrogen abstraction, convert $^{\bullet}CH_3$ and $^{\bullet}OH$ radicals to CH_3OH, and avoid catalyst inactivation by rapid desorption of products (Fig. 9a).[221] Recently, IrO_2 has been shown to be an effective catalyst for OCM application. Nørskov's group claimed that Ir coordinatively saturates with surface oxygen,[159] which could be considered as an oxygen-promoted surface contributing to the high activity *via* the dehydrogenation process.[222] However, another research with the opposite idea suggested that the (110) facet over IrO_2 is able to dissociate C–H at low-temperature *via* the deprotonation mechanism. In addition to the controversial reaction mechanism, single IrO_2 was not suitable for long-term OCM because overoxidation was unavoidable, resulting in undesired CO and CO_2. Besides IrO_2, other common thermal catalytic systems with the deprotonation process are noble metal-contained catalysts, which always exist in a low oxidation state so that proton acceptors can be accessible.[156,223,224] Taking Pt as an example, an organic ligand-stabilized Pt^{II} complex was designed for the conversion of CH_4 into methyl bisulfate (CH_3OSO_3H).[157] Using H_2SO_4 as a strong oxidant, this complex achieved 90% conversion of CH_4 and 81% selectivity of CH_3OSO_3H at 220 °C. Mechanistic studies showed that platinum-methyl, the intermediate of methyl ester, was produced *via* C–H activation of CH_4 over Pt^{II}. And Pt^{II} was the most active oxidation of Pt for OCM (Fig. 9b). Other works on homogeneous Pt-based catalysts reported a similar mechanism, in which Pt oxidized to Pt^{II} active sites and Pt^{IV}–CH_3 bond in an orderly manner. Finally, the reductive elimination produced CH_3OH and regenerated Pt^{II} active sites.[225–227] Although recent advances have been made in traditional thermocatalytic OCM, high temperatures (typically >600 °C) are always required for reactant activation, resulting in undesired products such as CO_x due to the high energy output property (exothermicity) of hydrocarbon combustion.[228] Meanwhile, the stability of OCM catalysts is also an inevitable issue due to the excessive heat energy released during the reaction.

2.3.2.2. Photocatalytic OCM. Photocatalysis is a promising approach to achieving OCM reactions in mild conditions.[21,28,229] However, studies of photocatalysis technology for realizing OCM are rare. Thus, in this section, a few noticeable and representative works will be summarized to display the great potential of photocatalytic OCM application. For instance, Tang's group designed a Pt/CuO_x-loaded TiO_2 photocatalyst with a 60% selectivity of C_2H_6 product in a gas flow reactor

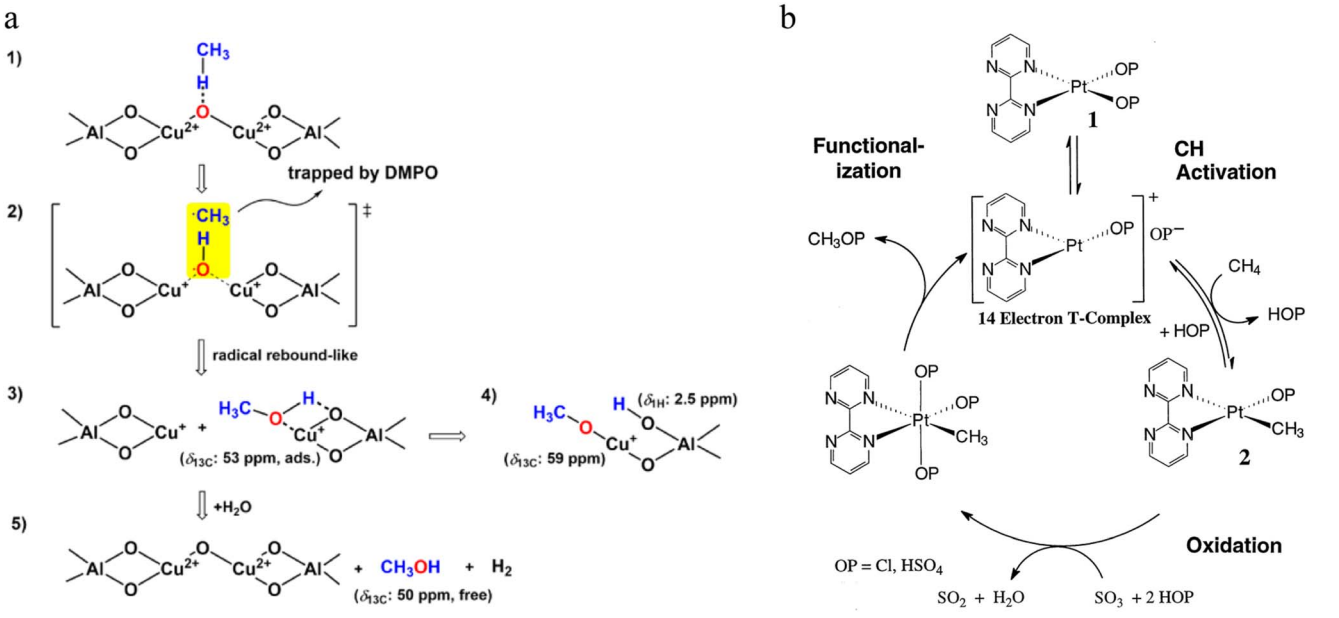

Fig. 9 (a) Transformation mechanism of CH_4 into CH_3OH on the Cu/Na-ZSM-5 zeolite.[221] Copyright © 2019, American Chemical Society (b) OCM mechanism.[157] Copyright © 1998, The American Association for the Advancement of Science.

(Fig. 10a).[85] In this nanohybrid, Pt as an electron acceptor facilitated the charge separation, while CuO_x was an active site for photoexcited holes. Thus, deep dehydrogenation and overoxidation could be effectively avoided because of the low oxidation potential of photoinduced holes over the VB of CuO_x clusters (Fig. 10b). A similar work to Pt/CuO_x-loaded TiO_2 photocatalyst was an Au–ZnO/TiO_2 photocatalyst with an ethane production rate of ~5000 μmol g^{-1} h^{-1} and 90% selectivity (Fig. 10c).[228] These values are the highest efficiency in the previously published works. The modification of Au and TiO_2 not only accelerated the charge transfer but benefited the O_2 activation owing to the low adsorption energy and activation barrier at oxygen vacancies (Fig. 10d and e).[230] The comprehensive investigation demonstrated that Au as a cocatalyst promotes the formation of $^{\bullet}CH_3$ radicals and inhibits the overoxidation of CH_4 to CO_2 through the OCH_3 intermediate (Fig. 10f–g). Another representative work was reported in 2019 by Liu *et al.*[231] A plasma-assisted photocatalyst was developed for the oxidation of CH_4 to C_2H_4 and CO *via* a new reaction route with CH_4 and CO_2 as reactants. Experimental analyses indicated that CO_2 and CH_4 tend to adsorb on TiO_2 and Ag surfaces, separately. Because of the localized surface plasma resonance (LSPR) effect on Ag and photoelectric effect in TiO_2, under a mild condition (simulated solar irradiation, 84.2 mW cm^{-2}), the evolution rates of CO and C_2H_4 were 1149 and 686 μmol g^{-1} h^{-1}, respectively. Apparently, the above studies successfully

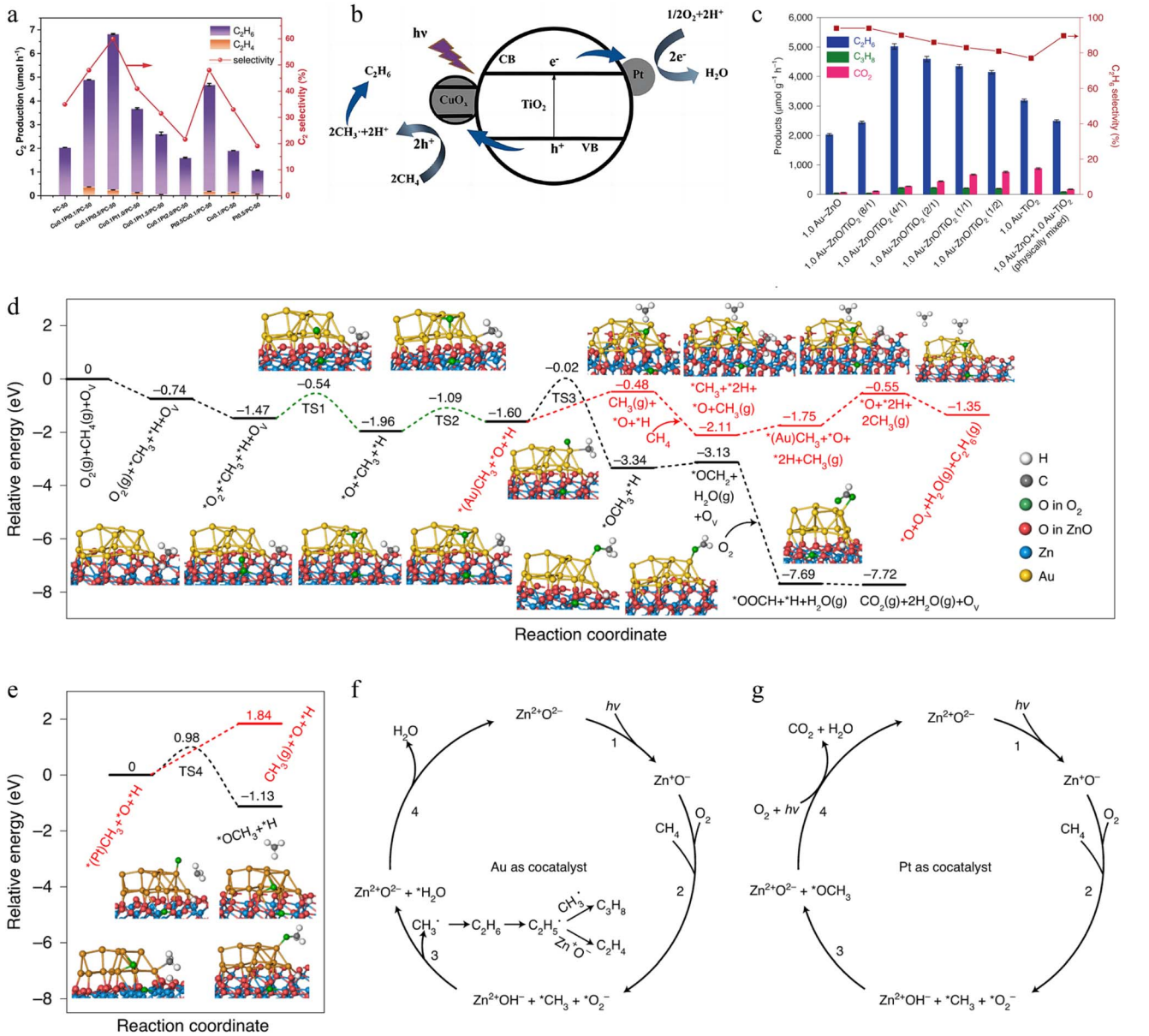

Fig. 10 Copyright © 2020 Wiley. (a) C_2 production and selectivity of photocatalytic OCM. Reaction conditions: $O_2/CH_4 = 1:400$, GHSV = 2400 h^{-1}, 40 W 365 nm LED 40 W, 40 °C.[85] (b) Photocatalytic OCM process.[85] (c) Photocatalytic OCM activity. Reaction conditions: 69 mL min^{-1} of CH_4 and 1 mL min^{-1} of 20% O_2/N_2, 300 W Xe lamp. Theoretical energy diagrams for (d) oxidizing CH_4 to C_2H_6 or CO_2 and (e) two key competing pathways. Proposed reaction process on (f) Au–ZnO and (g) Pt–ZnO.[228] Copyright © 2021 Springer Nature.

elucidate the great capacity of photocatalysis for OCM to obtain C_2 products with high selectivity.

2.3.3. Non-oxidative coupling of methane (NOCM): mechanism and kinetics. Since the C–C coupling reaction is able to produce more useful products than simple CO products, NOCM has become one of the main CH_4 conversion routes. Compared to the OCM, NOCM is more attractive since no oxidizing agent is necessary during this process. Meanwhile, NOCM can avoid too active oxidative products, which are often generated by the OCM process, and get high selectivity to desired products like H_2. The NOCM reaction mechanism is simpler compared to the above POM and DRM reactions. In brief, the activation process of CH_4 is direct during NOCM, during which the CH bond is dissociated. The absorbed H species was reduced to H_2, and two methyl radicals coupled with each other to form C_2H_6.

Several microkinetic models during NOCM have been proposed based on different kinds of catalysts. Dumesic's group studied the kinetic model of NOCM on PtSn surfaces with SiO_2 or H-ZSM-5 supports *via* DFT calculation.[232] Their model predicted that the full Pt surfaces adsorbed CH and C fragments and C–C coupling had the highest rate during the whole NOCM process. The RDS was the CH_4 activation and product (H_2) desorption over Pt species. Besides, the desorption of C_2H_6 as another main product also influenced the whole reaction rate to a large extent.

Kopyscinski *et al.* built another kinetic model based on a metal-free GaN/SBA-15 catalyst.[233] Their kinetic model was proposed *via* a simple 1D model with the same observed rate as the forward rate, reflecting the reaction process away from the chemical equilibrium and without mass transfer limitation. The kinetic studies and also the isotope labelling experiments confirmed that the possible reaction pathway should be through a fast transformation from CH_4 to $CH_3^{\bullet}$. Subsequently, the 2nd step was slow bond cleavage of C–H, forming $CH_2^{\bullet}$ and finally coupling to C_2H_6. However, the author believed that the RDS should be the conversion step from $CH_3^{\bullet}$ to $CH_2^{\bullet}$ instead of the H–CH_3 bond cracking since the apparent order of NOCM was ~0 in CH_4, indicating a fast adsorption process. More importantly, the authors claimed that active sites always fully adsorbed species. Their idea might be a basis for understanding and developing other metal-free catalysts.

With the appearance of single-atom catalysts (SACs), lots of SACs have been used for NOCM so some related kinetic studies have been conducted. For instance, Pohar's group explored the micro-kinetics of NOCM to C_2H_6 over Pt/CeO_2 catalyst.[234] In the SAC system, the RDS step was similar to the above metallic catalysts, in which the abstraction of the first $H^{\bullet}$ from a CH_4 molecule and the sorption/desorption of the H_2 product. However, one of the deficiencies in this model was the authors assumed the reactions only performed on Pt sites. Some works have proved that the active sites could also be the interface between Pt with CeO_2.[235] In the future, the synergistic effects between CeO_2 support and Pt sites should be accounted for. Kim *et al.* also studied the kinetic model on SAC containing Fe single-atom.[236] Similarly, they also claimed the formation of $CH_3^{\bullet}$ limited the whole NOCM efficiency. More importantly, they emphasized in the case of $CH_3^{\bullet}$ production, the activation barriers of CH_4 needed abundant $CH_3^{\bullet}$ conditions. However, the C–C coupling required higher hydrogen transfer rates on carbon-attached structures under $CH_3^{\bullet}$ deficient conditions. This conflict suggested the optimal conditions for these two steps (CH_4 conversion and C–C coupling) were difficult over a single catalyst. Therefore, the above works showed that there is still no perfect kinetic theory explaining all the catalytic NOCM systems. It is urgent to develop more theories and models to supply this area.

2.3.3.1. Thermal NOCM. The high thermodynamic barrier for NOCM means the high energy is essential to C–C coupling. Therefore, thermal catalytic technology is one of the common strategies to realize the NOCM reaction.[237,238] Since the NOCM was first reported by Wang's group,[239] different kinds of thermal catalysts have been designed and prepared for highly efficient and selective NOCM implementation. Metal- and alloy-based catalysts are one of the mainstream materials for NOCM. For instance, Soulivong's group reported a SiO_2-supported HTa catalyst with an ethane selectivity of 98%. However, in this work, the CH_4 conversion was less than 0.5%, which was not enough for industrialization.[240] Similarly, Guo *et al.* realized CH_4 conversion of 48% with C_2H_4, C_6H_6, and $C_{10}H_8$ with carbon selectivity of 53%, 22%, and 25% on Fe/SiO_2 catalyst at 950 °C.[241] The high CH_4 conversion rate and good selectivity are attractive, but how to separate such diverse products seemly will be another problem. Varma prepared Pt–Bi bimetallic catalyst supported on ZSM-5 zeolite for NOCM, achieving more than 90% selectivity at 873 K, suggesting the potential of polymetallic or alloy systems for NOCM.[242] Recently, due to the rapid development of molybdenum titanium carbide (MXene) family materials, noble metals presented by Pt have been anchored on the MXene substrate.[243] It has been confirmed that the metal/MXene system could activate the C–H bond in CH_4 molecular, then forming methyl radicals, which favoured desorption over subsequent dehydrogenation, so that coke deposition could be suppressed. In this case, the stability and CH_4 conversion rate could be enhanced.

Although so many works have been reported in the thermal catalytic NOCM field. As mentioned before, the inevitable disadvantage of NOCM, the high-temperature conditions, still cannot be avoided, which causes large energy consumption, low selectivity, and short longevity of thermal catalysts. Hence, the photocatalytic NOCM at mild conditions attracts more and more attention for exploring a new NOCM route and thus achieving carbon neutrality.

2.3.3.2. Photocatalytic NOCM. Photocatalytic NOCM can convert CH_4 to C_2H_6 and H_2 using light energy instead of thermal energy, thereby reducing the reaction temperature and thus avoiding catalyst coking or deactivation. In addition, the energy barrier for CH_4 activation can be lowered by photocatalysts. In 1998, Yoshida's group first reported the photocatalytic NOCM reaction over SiO_2/Al_2O_3 composite.[244] The SiO_2/Al_2O_3 photocatalyst exhibited the highest CH_4 conversion rate of 0.328 μmol h^{-1} under UV light irradiation. This study proved that the energy transfer from active sites (highly surface-dispersed Al species) to absorbed CH_4 might be the crucial step for CH_4 activation. Subsequently, a series of silica-based,

metal oxide-based, and zeolite-based catalysts have been widely investigated in the photocatalytic NOCM field.[89,245–247] Xiong *et al.* reported that the incorporation of Pd single atoms (SAs) into the lattice could overcome the limitations since the effect of O sites in VB was reduced.[248] In this work, TiO_2 was used as a proof-of-concept model. DFT calculations suggested that the TiO_2 (001) facet was the best surface for the SAs modification because of the loose arrangement of O atoms that can form the M–O bond (Fig. 11a). In order to demonstrate the activity and selectivity toward CH_4 to C_2H_6 conversion, a series of metal SA-modified TiO_2 were prepared for photocatalytic NOCM (Fig. 11b). The highest activity and selectivity were observed for Pd SA-loaded TiO_2. Therefore, the Pd_1/TiO_2 photocatalyst was further investigated. The high-angle annular dark-field scanning transmission electron microscopy (HAADF-STEM) revealed the atomically dispersed Pd elements on the TiO_2 support (Fig. 11c). The coordination of Pd was investigated by synchrotron radiation-based X-ray absorption near-edge structure (XANES) spectroscopy (Fig. 11d). Only a single peak at 1.53 Å could be detected on Pd/TiO_2 corresponding to the coordination between Pd and O (Pd–O), indicating the presence of isolated Pd atoms in the photocatalyst. Thus, the coordination

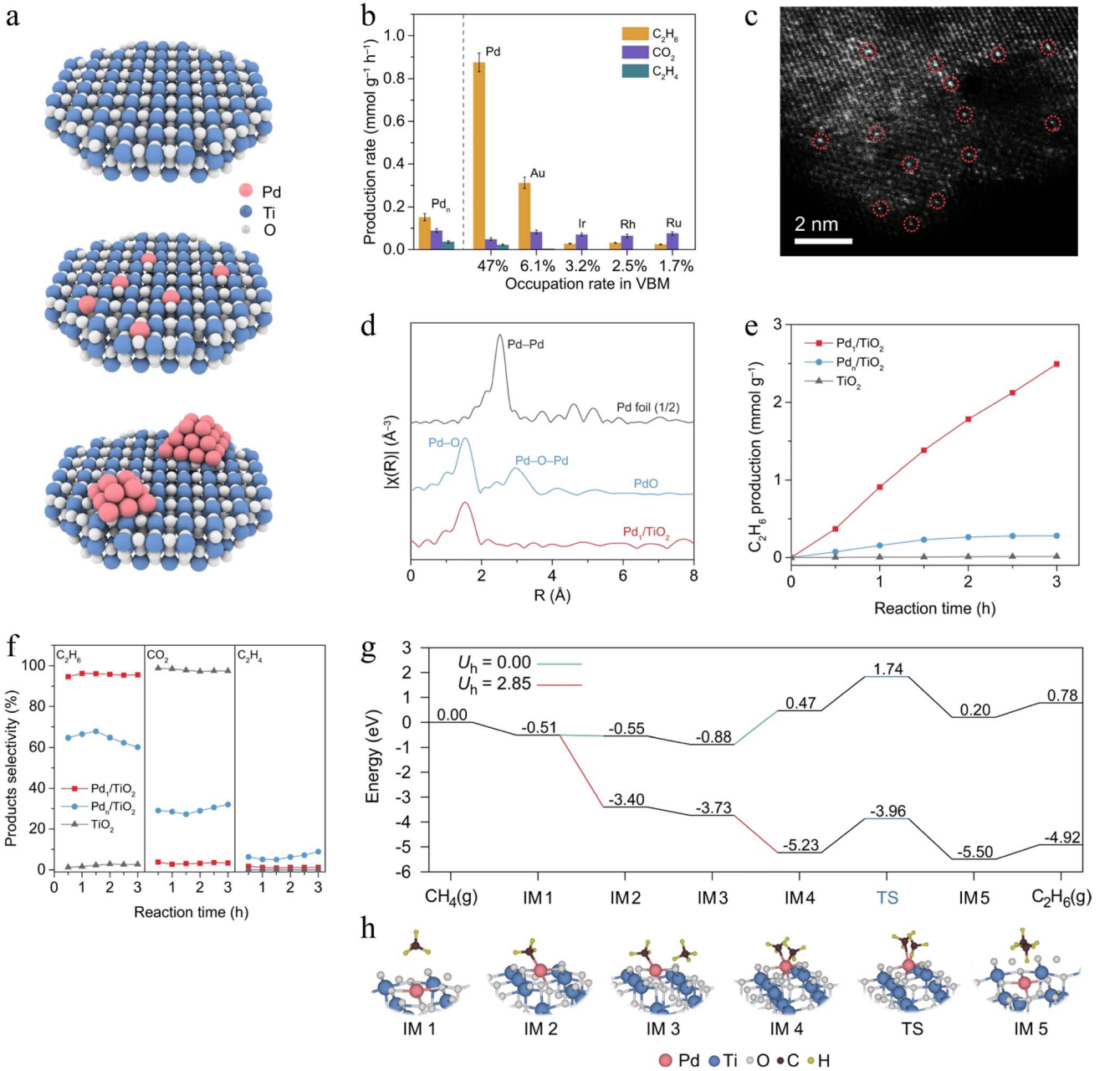

Fig. 11 (a) Pristine TiO_2, Pd_1/TiO_2, and Pd_n/TiO_2 models. (b) The metal contribution in VBM and photocatalytic NOCM performance. Reaction conditions: 0.1 MPa CH_4, 300 W Xe lamp, room temperature. (c) STEM image and (d) Pd K-edge EXAFS spectra in *R* space of Pd_1/TiO_2. (e) The C_2H_6 production rates (f) and the corresponding selectivity of C_2H_6, C_2H_4, and CO_2 in 0.1 MPa CH_4. (g) Free-energy diagrams for C_2H_6 production on Pd_1/TiO_2. (h) Coordination environment during the DFT simulation.[248] Copyright © 2022, Springer Nature.

environment of Pd–O_4 was formed through Pd SA binding with O atoms in TiO_2 crystalline. Under ambient conditions with Xe lamp illumination, the photocatalytic NOCM results showed pristine TiO_2 nanosheets exhibited a very low production rate of C_2H_6 (Fig. 11e). This could be attributed to the involvement of the lattice oxygen in CH_4 conversion, resulting in a susceptible overoxidation to produce CO_2 (Fig. 11f). In contrast, Pd/TiO_2 exhibited a very high C_2H_6 production rate during the NOCM reactions. The improvement of the photocatalytic activity was due to Pd active sites instead of the lattice oxygen in TiO_2, which suppressed the overoxidation of CH_4 and accelerated the desorption of C_2H_6. To investigate the role of Pd SAs in CH_4 dissociation and intermediate coupling *via* photogenerated holes, the energy barrier of the CH_4–CH_4 coupling on the active sites of Pd/TiO_2 was studied by DFT calculation (Fig. 11g–h). Under dark conditions (Uh = 0.00), CH_4 required higher energy for activation. Meanwhile, 1.74 eV of activation energy from CH_4 to TS state was so high that hindered the whole NOCM. However, photogenerated holes would provide additional potential, so that the energy barrier of the step turns down (IM3 to IM4). In addition, the energy barriers of C–C coupling and C_2H_6 desorption *via* Pd SAs were also lowered. Thus, the photoexcited charge and the atomic-level reaction platform were advantageous for triggering the photocatalytic NOCM reaction with lower energy input and mild conditions. This work suggested the great advantages of photocatalysis in the activity and selectivity of NOCM.

3. Key role of ferroelectric materials in photocatalytic reactions

3.1. Ferroelectric materials

Ferroelectricity was first discovered in rock salt in 1921.[249] The ferroelectric material is one of the piezoelectric materials, which belongs to pyroelectrics and then dielectric materials in sequence. Unlike pyroelectric and piezoelectric materials, ferroelectrics have spontaneous dipole moments without an external heating source or applied stress activation. The dipole moments generate spontaneous polarization electric fields, which offer a sustainable driving force for the separation and transfer of charge carriers from bulk to the surface of catalysts. In general, ferroelectric materials can be classified into three main families, *viz.* inorganic, organic, and organic–inorganic hybrids. What follows summarizes the most representative ferroelectric-based photocatalysts utilized for CH_4 conversion approaches.

3.1.1. Inorganic ferroelectric materials

3.1.1.1. Ferroelectric oxides. According to different structures, ferroelectric oxides have four basic types: perovskite, pyrochlore, tungsten-bronzes, and layer-type bismuth compounds (also called Aurivillius).[250] Among them, perovskite possesses higher polarization strength. Therefore, they are widely exploited in photocatalysis and photovoltaics. In ferroelectric oxides with perovskite structure, the ferroelectricity is from the electron clouds hybridization mechanism between adjacent ions, called displacive ferroelectricity.[251] The photovoltaic effect in ferroelectric perovskite oxides was discovered in the 1950s and still gaining increasing attention.[252] The homogeneous bulk region in ferroelectric semiconductors with inherent non-centrosymmetry could generate photocurrent and even photovoltage beyond the bandgap.[253,254] Therefore, the photovoltage from ferroelectrics depended on the energy band structure instead of the built-in potential induced by p–n junctions or Schottky junctions at the interface.[55] This property could be not only used in photovoltaics but also extended to photocatalysis. In fact, several studies have applied photoinduced charges and polarization from ferroelectric perovskite oxides to improve photocatalytic efficiency.[255–257] These works confirmed that perovskite oxides were effective in both photocatalytic reduction and oxidation reactions, providing experimental support for fully utilizing ferroelectric oxides in various photocatalytic fields. More details about published work in photocatalytic methane conversion fields will be further introduced in the following sections. Currently, the main deficiency in conventional ferroelectric oxide perovskites is the narrow light responding range and unsatisfactory conductivity, limiting the photovoltaic and photocatalytic efficiency. In this case, the bandgap engineering promotes the development of ferroelectric perovskite into organic–inorganic halide perovskites as shown below.

3.1.2. Organic ferroelectric materials

3.1.2.1. Liquid crystals (LCs). LCs are a crucial part of the family called soft condensed matter materials. Thermodynamically, the state of LCs is located between an isotropic liquid and a crystalline phase.[258] They are partially ordered but have anisotropic physical properties, such as electric conductivity or magnetic susceptibility while maintaining flowability.[259] The mainstream methods for producing LCs are based on thermotropic phases and lyotropic phases, which are achieved by changing the intensive variable of state and the dopant concentration in the isotropic solvent, respectively. The ferroelectric properties in the LC family should be attributed to the chiral smectic C (SmC) phase, which is one of the molecular arrangements in LCs (the other two structures are nematic and smectic A phase).[260] The chiral SmC is similar to SmC structure, but owing to the chiral properties, Meyer *et al.* presented the idea that a chiral smectic C mesophase should be ferroelectric, which has been experimentally confirmed in 1975 *via* reporting practical ferroelectric LCs.[261] Owing to the particular chiral SmC phase with helical structure, ferroelectric LC shows spontaneous polarization and molecular switching in microsecond order. These attractive properties lead to wide applications in modern photonic fields including grating,[262] lensing,[263] beam steering,[264] *etc.* Unfortunately, the aforementioned promising advantages of ferroelectric LCs are still not utilized in the whole catalytic field. Considering the fact that more and more studies tried to regulate the ferroelectricity/ferromagnetism in LCs,[265,266] the ferroelectric LC family could be a potential candidate for achieving efficient photocatalytic implementations.

3.1.2.2. Ferroelectric polymers. In addition to ferroelectric LCs, the organic ferroelectric solid is another great family belonging to the class of organic ferroelectric materials. In this

family, ferroelectric polymer is one of the most widely developed organic ferroelectrics and has been used in organic solar cells,[267] ferroelectric memory,[268] piezoelectric devices,[269] and electrocaloric refrigeration devices.[270] Among them, poly(-vinylidene fluoride) (PVDF) and corresponding copolymers/terpolymers are the most representative ferroelectric polymers. PVDF and the co-/ter-polymers had high dielectric constant so that they are regarded as promising thin film-type materials for high-energy-density capacitors.[271] In the photocatalytic field, PVDF is also developed as the source of ferroelectric fields, which are used to improve charge-carrier transfer behaviours. In brief, through the ferroelectric effect, PVDF-based photocatalysts have promoted different photocatalytic redox reactions, such as overall water splitting,[38,272] CO_2 photoreduction,[273] and advanced oxidation.[274] Although there is no work on PVDF-based photocatalytic systems for methane conversion implementation, in consideration of the great ability of PVDF and other ferroelectric polymers, organic ferroelectric polymers should be applied as substrates or cocatalysts for controlling charge migration pathways in future studies.

Although the low-molecular-mass compound is also a kind of organic ferroelectrics, since it is difficult for the steric to reorient dipoles, causing an extremely larger coercive field than that of other ferroelectrics, the number of the low-molecular-mass compound with ferroelectricity is rare so that the real-implementation of the low-molecular-mass compound is limited.[275] Therefore, the low-molecular-mass compound represented by thiourea,[276] the 2,2,6,6-tetramethyl-1-piperidinyloxy (TEMPO) free radical,[277] and 1,6-bis(2,4-dinitrophenoxy)-2,4-hexadiyne[278] are not listed as an independent sub-section.

3.1.3. Organic–inorganic hybrid ferroelectric materials

3.1.3.1. Ferroelectric metal–organic complex (MOC). Since Valasek reported the ferroelectrics in Rochelle salt,[279] tremendous efforts have been made to design and fabricate novel molecular-based ferroelectric materials. Although the ferroelectric oxides family is well-known due to their strong intrinsic ferroelectric effect, they are heavy, weak mechanically flexible, and not environmentally friendly.[280] Owing to the ferroelectricity of organic molecules, organic ferroelectric materials gradually enter researchers' version as a new generation of ferroelectric material. If a metal–organic complex (MOC) can show ferroelectricity *via* modulating dipole moments of its components, this MOC belongs to the family of organic ferroelectric materials. Further, according to their crystal structures, ferroelectric MOC can be divided into (i) discrete (0D), (ii) 1D chain, (iii) 2D layer structure, and (iv) 3D framework. It is true that several ferroelectric MOCs have been reported by molecular design based on the addition of chiral/polar molecules/ions or structurally flexible ligands or ions, but the ferroelectric MOC is still at the early step since the number of developed MOCs is not abundant. Some works have reviewed the advances of ferroelectric MOC and also predicted their potential real-applicat ion. Detailed descriptions can be seen in these excellent review articles.[280,281] However, in the catalytic field, studies about ferroelectric MOC are scarce, meaning that it is urgent to perform some theoretical studies based on thermodynamic theories and crystallographic requirements to offer fundamental support for exploring and developing ferroelectric MOC in photocatalytic areas.

3.1.3.2. Organic–inorganic perovskites. To a large extent, the prosperity of basic theory and practical applications in the field of ferroelectric materials should be attributed to the conventional inorganic ferroelectric perovskites with high stability and tunable ferroelectric properties.[282] Subsequently, molecular ferroelectrics are flexible, cheap, and environmental-friendly, and also have biocompatibility and homochirality so the appearance of molecular ferroelectrics attracted our version, causing a novel family of hybrid organic–inorganic perovskite ferroelectric (HOIPF) materials.[283,284] Compared to traditional inorganic ferroelectrics, HOIPFs have larger piezoelectricity coefficients, lower toxicity, and controllable chemical structures although their ferroelectricity is weaker. Besides, the ferroelectric quantum theory and Berry phase calculation also clarify their potential in semiconductor areas.[285] Semiconductor properties transform HOIPFs into a new generation of photonic device platforms.[286] For instance, some Pb-based or lead-free HOIPFs had tunable bandgap and high mobility similar to common inorganic ferroelectric semiconductors.[287,288] A series of functional HOIPFs including $(cyclohexylaminium)_2PbBr_4$,[289] (*R*)- and (*S*)-3-(fluoropyrrolidinium)$MnBr_3$ (ref. 290) possess outstanding luminescent properties, such as high-purity luminescence, wider luminescence range, and high photoluminescence efficiency.[291] Besides, the HOIPFs-based optoelectronic applications (*e.g.* bulk photovoltaic and self-powered photodetection) are also gradually explored with tremendous efforts on the photoresponse effects from HOIPFs and multifunctional hybrid ferroelectric systems.[292,293] Although HOIPFs still face some challenges like mechanical weakness, low stability, and short resistivity, the disadvantages do not stop the expansion of the applications of HOIPFs towards photocatalytic fields. Actually, some lead-free halide perovskites (*e.g.* $Cs_2AgInCl_6$ and Cs_3BiBr_6) have been used for photocatalytic advanced oxidation reactions,[294,295] photoreduction reactions,[296] and even photocatalytic organic synthesis.[297]

Considering the number of practical examples of ferroelectric photocatalysts developed for methane conversion is very limited, it is necessary to emphasize the great effect of ferroelectric-assisted photocatalytic systems in improving methane conversion efficiency. In subsequent sections, the representative works about aforementioned ferroelectrics, especially ferroelectric perovskite and ferroelectric oxides, for methane conversion implementations will be introduced for further advancing the ferroelectrics-based catalytic community.

3.1.4. 2D ferroelectric materials.

Although the traditional metal oxide-based ferroelectric materials have displayed stable spontaneous polarization, the high demands of micro/nano devices might result in depolarization and dangling bond problems during the reducing thickness process and finally eliminate the ferroelectricity. In order to deal with this issue, the exploration of 2D materials with stable ferroelectric properties attracts wide interest in the Material Science community. Especially, monolayered 2D materials open a new direction for developing 2D ferroelectrics. Recently, single-layered Sn–Te[298]

and α-In_2–Se_3 (ref. 299) have been confirmed as ferroelectric materials owing to their out-of-plane polarization under 270 K and ambient temperature, respectively. Through theoretical prediction, oxidized MXene family showed switchable polarization *via* the intermediate antiferroelectric phase.[300] Some research also indicated the potential ferroelectricity of monoelemental 2D materials akin to graphene (known as 2D Xenes).[301] For instance, it has been forecasted that the chemical-functionalized phosphorene has ferromagnetism and ferroelectricity simultaneously,[302] however, the poor stability and high surface energy of 2D Xenes seemly become the challenge to realize this prediction. The quantum orders and pristine crystal structures of 2D Xenes should be well reserved when functionalizing them towards ferroelectrics. Fortunately, some works experimentally achieved the implantation of ferroelectricity into 2D Xenes, including CrI_3 (ref. 303 and 304) and $CrGeTe_3$,[305] encouraging further investigation in this area. Beyond them, Kou *et al.* proposed a possible multiferroic or concurrent ferroic and topological order based on the CH_2OCH_3-functionalized germanene (2D-Ge).[306] The p_z orbits of Ge were the resource of ferroelectricity. And the switchable polarization resulted from the electric field-induced ligand molecules (*i.e.* CH_2OCH_3) rotation. Considering the potential use of 2D-Ge derivatives in several fields, including electrocatalysis,[307] biosensing,[308] and (opto)electronics,[309] 2D-Ge might be a suitable candidate to act as a ferroelectric-assisted system for photocatalytic energy conversion reactions.

3.2. Key role of ferroelectric materials in photocatalytic reactions

Ferroelectric materials play a crucial role in photocatalytic reactions owing to their inherent domain walls (DWs), which arise from breaking-symmetry. These DWs influence charge transfer,[310] local surface potential,[311] and even surface adsorption/activation ability,[312] all of which are essential for improving photocatalytic efficiency. Thus, this section summarizes the basic mechanism of DWs influencing photocatalytic reactions, supported by both experimental evidence and theoretical predictions.

3.2.1. Polarization/built-in electric field promoting charge separation. Ferroelectric materials exhibit spontaneous dipole moments that create an internal electric field that favours charge separation.[313] Additionally, they generate spontaneous polarization with potential differences. Then, perpendicular to DWs, these potential differences act as a driving force to establish a built-in electric field. The role of polarization, along with the corresponding built-in electric field, can be categorized into promoting bulk charge separation and surface charge separation, thereby reducing recombination and enhancing photocatalytic performance.[69]

A prominent example for confirming the promotion of bulk charge separation is based on the $SrBi_4Ti_4O_{15}$ ferroelectric photocatalyst.[255] In this work, Huang and co-workers visualized the intrinsic ferroelectric polarization of $SrBi_4Ti_4O_{15}$ nanosheet *via* KPFM, which was rationalized by DFT calculations. The KPFM images showed DWs with an amorphous shape (Fig. 12a). The bright and dark areas corresponded to different polarization directions. DFT calculations revealed that the effective masses of e^- and h^+ along the [100] orientation were smaller than along other orientations, suggesting the higher migration rates of e^- and h^+ along this axis, which was consistent with the polarization direction in $SrBi_4Ti_4O_{15}$. Therefore, ferroelectric polarization promoted charge transfer. Similarly, Park *et al.*[314] prepared $K_{0.5}Na_{0.5}NbO_3$ with a permanent polarization *via* a corona electric field polarization method. With external polarization, the time-resolved photoluminescence (PL) spectra of $K_{0.5}Na_{0.5}NbO_3$ presented a decrease in the decay time from 1.64 to 3.31 ns (Fig. 12b). This result suggests that the ferroelectric polarization field inhibited the recombination between electrons and holes.

Beyond the bulk charge separation, the ferroelectric effect can also promote charge transfer at the interface of heterojunctions. Considering the short time scale of interfacial charge migration, the electrochemical analysis becomes a reliable method to monitor the effect of ferroelectric materials. For example, Huang's group designed a heterojunction containing ferroelectric tetragonal-phase $BaTiO_3$ (T-$BaTiO_3$) and narrow-band-gap semiconductor BiOI (T-$BaTiO_3$/BiOI).[67] They applied photoelectrochemical (PEC) measurements to further investigate the polarization-induced field. Interestingly, with higher bias voltage, the photocurrent of T-$BaTiO_3$/BiOI samples showed clear changes. In contrast, control experiments displayed stable current intensity, indicating that polarization could adjust charge transfer and be adjusted by external bias voltage (Fig. 12c). Other similar works also prepared ferroelectrics-based heterojunctions for accelerating the surface charge mobility during different photocatalytic reactions.[58,315,316] In the field of methane conversion, although mechanistic studies are still at the early stage, state-of-the-art characterization methods like PL and PEC analysis have recently been used to clarify the role of ferroelectric materials in charge transfer kinetics. These results will be discussed in detail in Section 4.

3.2.2. Polar nano regions and surface active sites. The driving force from spontaneous polarization in ferroelectric materials leads to the opposite migration direction between electrons and holes, further resulting in the different polarity walls over the ferroelectric surface (*viz.* polar nano regions). Therefore, by controlling the switchable polarization *via* external fields or stimulations, ferroelectric materials can be explored as a bi-functional electrode for photocatalytic redox reactions.[56] For instance, Rohrer and co-workers used AFM characterization to elucidate the domain-specific reactivity of two samples of elemental-doped $BiVO_4$—named as $(Bi_{1-0.5x}Na_{0.5x})(V_{1-x}Mo_x)O_4$, where $x = 0.05$ and $x = 0.175$ was assigned to samples exhibiting monoclinic and tetragonal domains, respectively.[317] The AFM images of undoped monoclinic $BiVO_4$ showed the alternative properties between reduction and oxidation domains, corresponding to ferroelastic domains (Fig. 13a). This observation suggested the possibility of both reduction and oxidation to take place on the ferroelectric surface but with different polarization. Further, the authors employed piezoelectric force microscopy (PFM) to display the

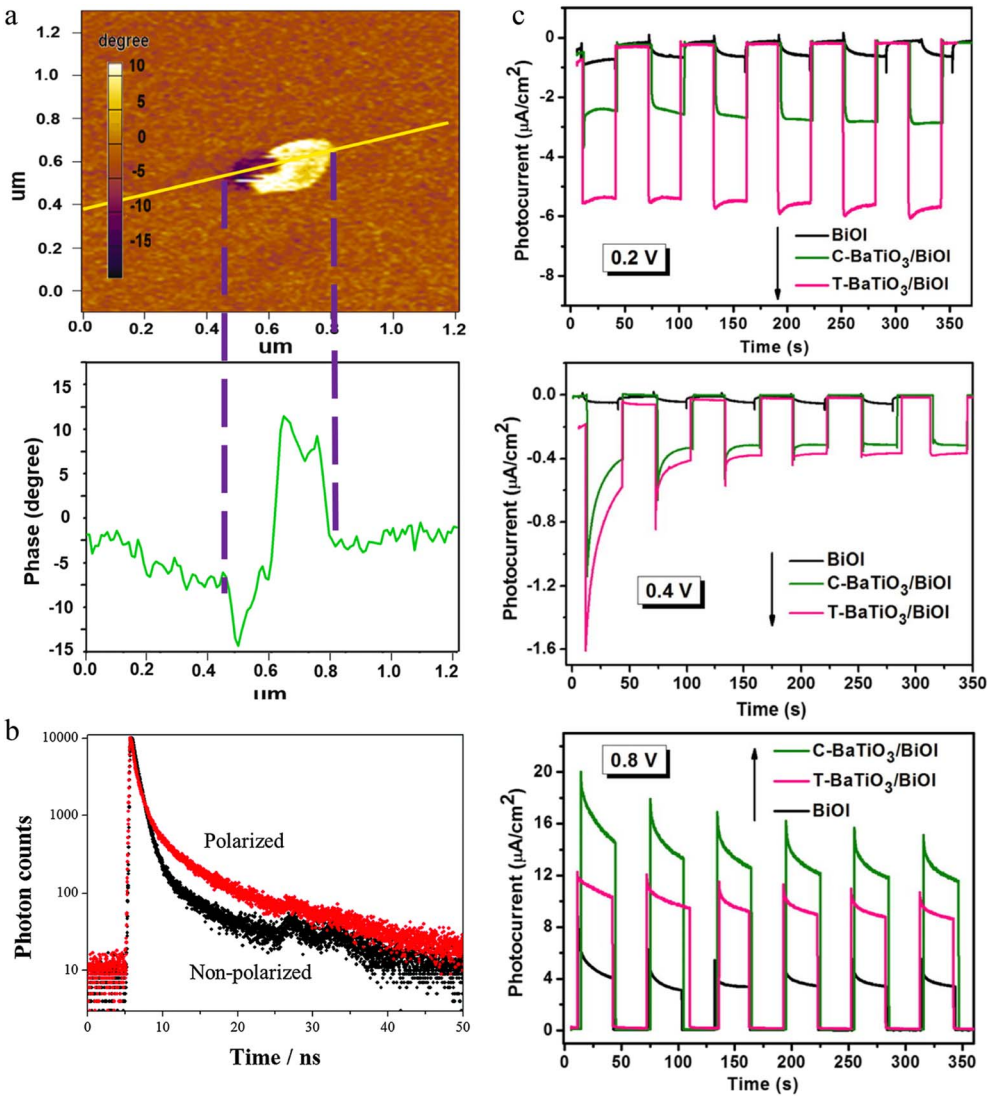

Fig. 12 (a) Phase maps (top) and corresponding curve (bottom) of the piezoelectric response.[255] Copyright © 2018 Elsevier. (b) Decay profile of PL from $K_{0.5}Na_{0.5}NbO_3$.[314] Copyright © 2014 Royal Society of Chemistry. (c) Transient photocurrent responses at different bias voltages.[67] Copyright © 2017 Elsevier.

piezoresponsive nature of doped $BiVO_4$ (Fig. 13b). While the monoclinic $BiVO_4$ sample possessed a polar surface, the tetragonal $BiVO_4$ sample did not show polar domains according to the colour contrast in these images. After light illumination, AFM images presented the photo-deposition states over monoclinic and tetragonal $BiVO_4$ (Fig. 13c and d). The higher height of monoclinic $BiVO_4$ suggested that more particles were deposited on its surface, meaning stronger reactivity. Therefore, the ferroelectric effect was proved to improve the photochemical activity. Similarly, over a $BaTiO_3$ surface, AFM was also applied to monitor ferroelectric properties.[318] Interestingly, the product distribution matched the underlying domain structure of the $BaTiO_3$ matrix, once again confirming the role of the dipolar field in the improvement of reactivity (Fig. 13e and f). Besides the experimental evidence, some works used DFT calculations to show the polarization-dependent binding geometries and simulate the surface adsorption/desorption states over ferroelectric materials. Taking $PbTiO_3$ as a case study, the positively polarized electrons were beneficial for capturing reactants (*i.e.*, O_2 and NO molecules) for subsequent redox reactions (Fig. 13g–i).[319] Once the surface was saturated, the polarization states were not stable, and the products were easily desorbed, thus returning the polar surface to the pristine status. This fact not only ensured the long-term reaction cycles but also avoided the negative effect of poisoning molecules or overreaction towards undesired products.

Another potential role of ferroelectric materials is to provide high-density surface active sites as discussed in Section 1. The conversion of CO_2 into $CO_2^{\bullet-}$ bidentate radical is promoted by the electrons on positively polarized surfaces/sites.[147] Further, based on the $CO_2^{\bullet-}$ intermediate, the interaction between $CO_2^{\bullet-}$ and H^+ to form $HCOO^{\bullet-}$ and finally HCOOH is achieved

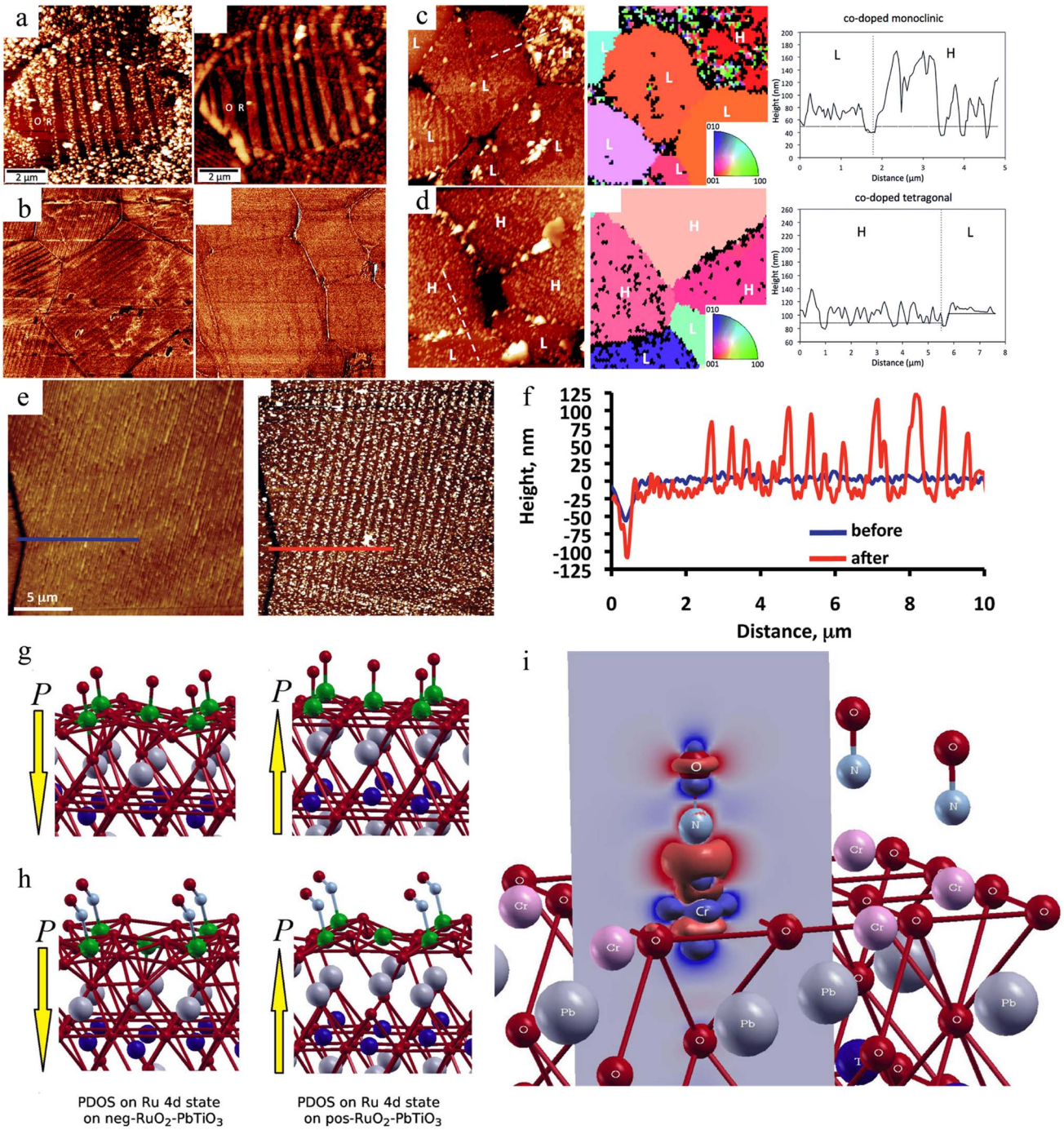

Fig. 13 (a) Surface topography after Ag^{+} reduction (left) and Mn^{2+} oxidation (right). (b) PFM phase images of monoclinic and tetragonal elemental-doped $BiVO_4$. Surface topographic images (left), inverse pole figure maps (mid), and topographic line profiles (right) of (c) monoclinic and (d) tetragonal elemental-doped $BiVO_4$.[317] Copyright © 2016 Royal Society of Chemistry. (e) AFM images of rutile TiO_2 supported by $BaTiO_3$ before (left) and after (right) a photochemical reaction, and (f) their heights.[318] Copyright © 2010 American Chemical Society. (g) O_2 dissociative binding and (h) NO binding on negatively (left) and positively (right) poled RuO_2–$PbTiO_3$. (i) Space electron redistribution, presenting covalent binding between NO and positively poled CrO_2–$PbTiO_3$.[319] Copyright © 2015 American Chemical Society.

via a proton-coupled electron mechanism.[154] Accordingly, CH_4 dissociation/cracking should tend to occur on negatively polarized surfaces/sites. In the case of ferroelectrics, the reduction and oxidation reactions will take place at different polarized surfaces/sites, inhibiting the recombination between photoexcited electrons and holes.

4. Ferroelectric-assisted photocatalytic methane conversion

4.1. Ferroelectric-assisted photocatalytic DRM

Recently, a Fe_2O_3-loaded $BaTiO_3$ photocatalyst (denoted as BF*xy*, where *xy* is the $BaTiO_3/Fe_2O_3$ molar ratio) is reported for

the DRM reaction.[320] The photoluminescence signals, a feature of the recombination rate of charge carriers, emitted by all the samples were measured (Fig. 14a). $BaTiO_3$ showed the lowest charge recombination rate due to its intrinsic ferroelectric property. On the contrary, Fe_2O_3 showed the maximum charge recombination rate due to the narrow band gap of Fe_2O_3. The heterostructure and charge transfer across to interface of BF were confirmed by PL spectra. In this case, the ferroelectric effect from $BaTiO_3$ endowed BF composites with a higher charge separation/transfer efficiency than Fe_2O_3. Thus, the DRM activity of BF31 showed the highest reactant conversion efficiency (Fig. 14b). Besides $BaTiO_3$, TaN as another ferroelectric material was also developed for photocatalytic DRM reaction.[146] In this work, Liu's group explored the effect of TaN as the photocatalyst substrate with a Pt NPs loading (Pt/TaN). Under visible light illumination, Pt/TaN showed improved photocatalytic DRM activity. The convergent beam electron diffraction (CBED) characterization exhibited the polarization phenomenon in the TaN substrate (Fig. 14a). Obviously, the polarity would lead to a built-in electric field, facilitating the photoexcited charge separation. On the contrary, TiN and ZrN as the reference samples did not show any polarized property and thus had lower activity than Pt/TaN (Fig. 14b and c). Accordingly, this study also proved the ineligible enhancement role of ferroelectrics with electrostatic field in photocatalytic efficiency.

Until now, a large number of ferroelectric materials have been developed in photocatalytic fields.[86,321] Unfortunately, in photocatalytic DRM implementations, the previous reports prefer to pay more attention to the impact of cocatalysts or the heterojunction with controllable energy band structure in the DRM process instead of investigating the ferroelectric effect and enhanced charge transfer dynamics. With the development of ferroelectric materials, the ferroelectric effect is expected to be maintained even under harsh reaction conditions (high temperatures or pressures),[154] meaning that ferroelectrics can be widely used in different photo(thermal) catalytic applications. Therefore, it is hoped to report more in-depth research on the improvement of DRM reactions from the view of the ferroelectric effects soon. Our previous literature also discussed and emphasized the role of the ferroelectric field especially in DRM applications, the potential interested audience is recommended to browse ref. 55.

4.2. Ferroelectric-assisted photocatalytic POM

As mentioned above, the permanent polarization generated from ferroelectrics creates a built-in electric field. The strong and reliable driving force in an electric field adjusts the transfer path of electrons and holes to different active sites, separately. As a result, more charge carriers tend to complete the redox reaction instead of recombination. An early work was reported by Yi's group in 2013,[322] where $NaNbO_3$ polar semiconductors

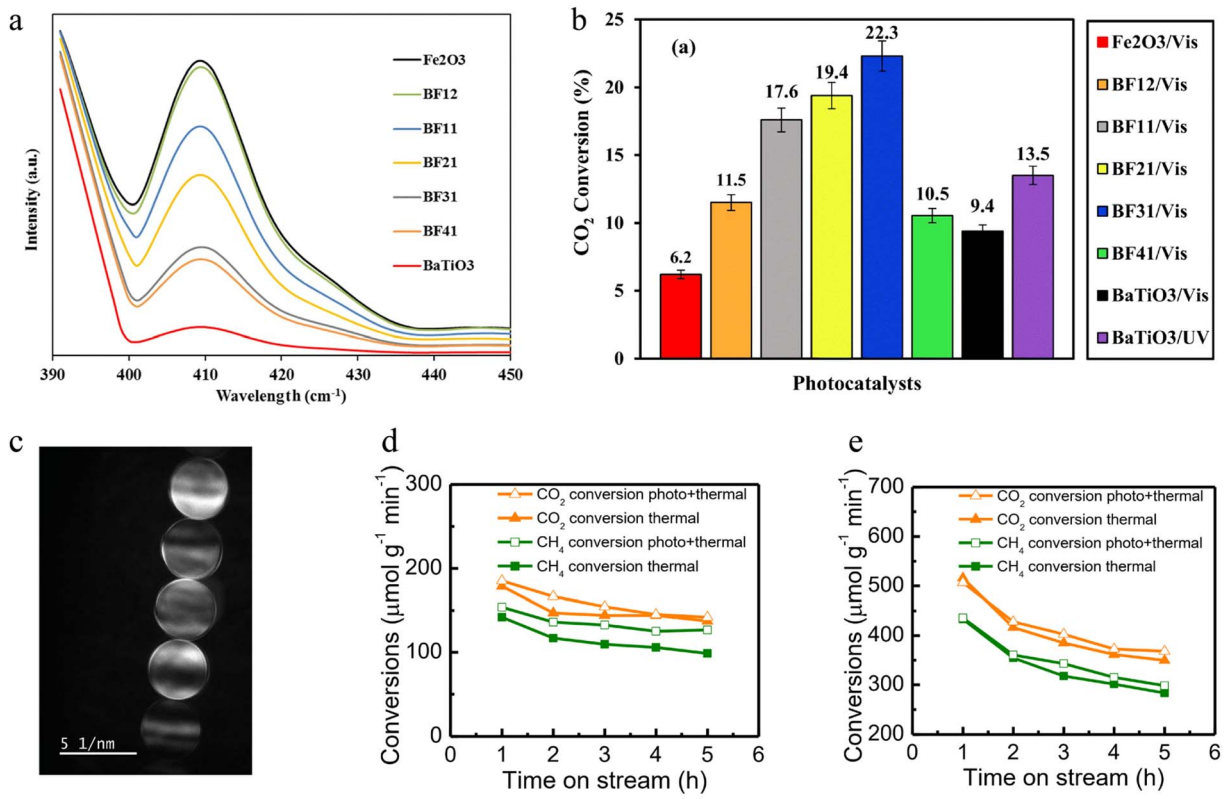

Fig. 14 (a) PL spectra and (b) CO_2 conversion efficiency of $BaTiO_3$, Fe_2O_3, and BF*xy*. Reaction conditions: 40 psi containing 45% CO_2, 45% CH_4, and 10% He, 125 W Hg lamp, 35 °C.[320] Copyright © 2019, Springer Nature. (a) CBED pattern of TaN. Catalytic DRM performance of (b) Pt/ZrN and (c) Pt/TiN. Reaction conditions: 300 W Xe lamp, $CH_4/CO_2 = 1$ (20.0 mL min^{-1}), 500 °C.[146] Copyright © 2018, Wiley.

were used to enhance the POM activity. Scanning electron microscopy (SEM) images showed the preparation of $NaNbO_3$ nanocuboids with ordered *b*-axis orientation (NNB-1, Fig. 15a and b). To investigate the role of ferroelectric property, the disordered random distribution of $NaNbO_3$ (NNB-8) was also obtained (Fig. 15c). In general, the $NaNbO_3$ crystal showed antiferroelectric and ferroelectric properties in the direction of the *c*-axis and *b*-axis, respectively, implying an internal polarization in $NaNbO_3$ nanocuboids along the *b*-axis.[323] Instead, $NaNbO_3$ nanocuboids with a disordered nanostructure would induce a randomly distributed local bias electric field. In photocatalytic CH_4 oxidation experiments, with Pt loading as cocatalyst *via* impregnation and photodeposition methods (denoted as Pt-NNB-1, Pt-NNB-1-LD, Pt-NNB-8, and Pt-NNB-8-LD), the CO_2 evolution rate of NNB-1 was much higher than that of NNB-8 (Fig. 15d). Interestingly, pure NNB-1 had higher activity than that Pt-NNB-1 and Pt-NNB-1-LD. The reason was investigated by SEM, which showed that the Pt loading process caused the destruction of the ordered structure of NNB-1 (Fig. 15e). Therefore, the structure orderliness was a crucial factor for CH_4 oxidation because it was a prerequisite for maintaining the strong ferroelectric effect (Fig. 15f). And the above results also confirmed the great ability of polar semiconductors with built-in electric fields to enhance CH_4 oxidation compared to conventional cocatalysts (*e.g.* Pt). To further investigate the ferroelectric effect, photoelectrochemical (PEC) measurements were used to detect the photocurrent responses of different $NaNbO_3$ samples. As shown in Fig. 15g and h, the authors used photoelectrochemical measurements, which displayed higher photovoltage and photocurrent response on ordered NNB-1 compared to disordered NNB-8, to confirm the built-in electric field of each crystal unit with consistent

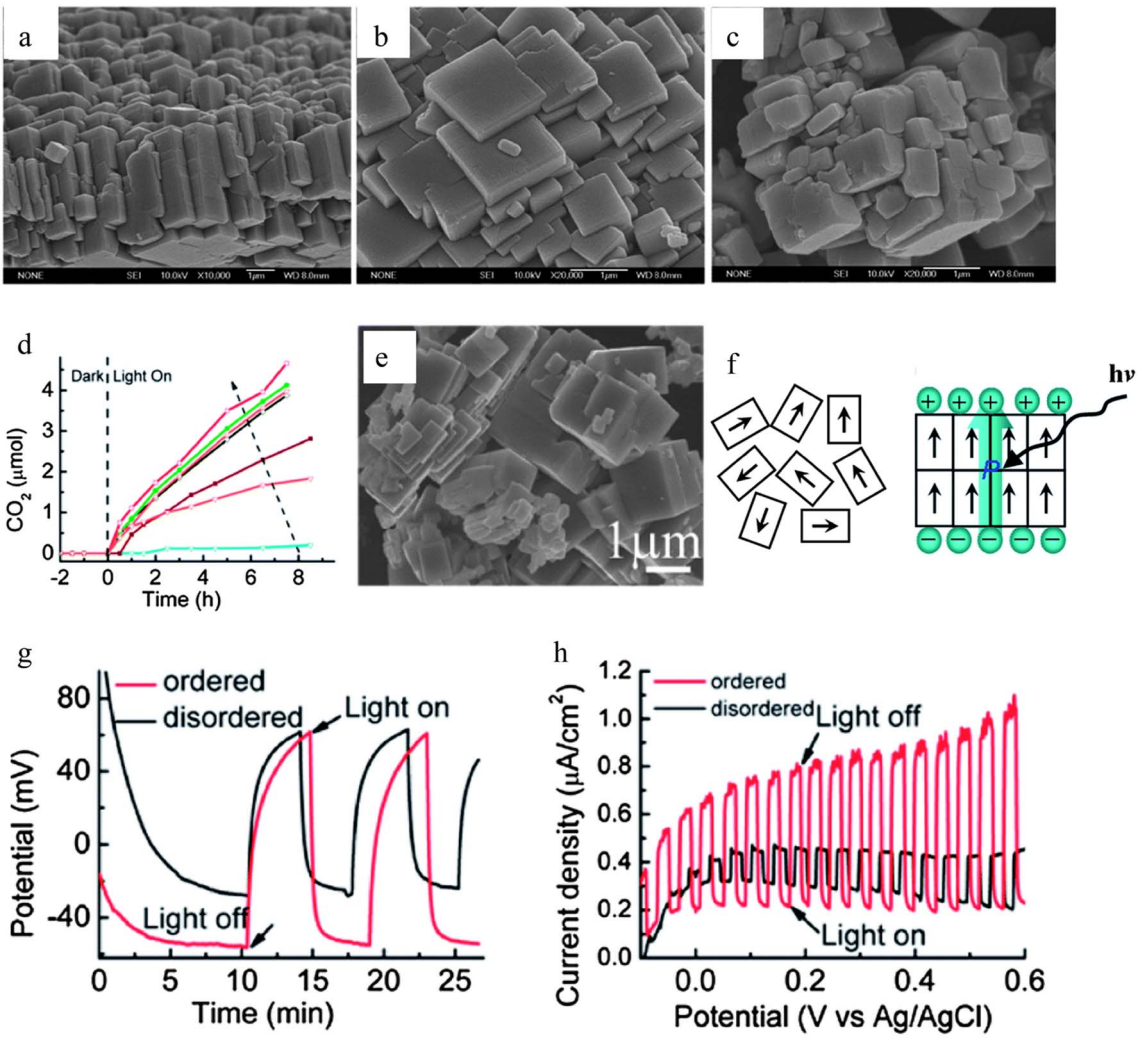

Fig. 15 SEM images of $NaNbO_3$ samples with (a) and (b) ordered, and (c) disordered nano cuboid assemblage. (d) CO_2 evolution from POM reaction. Reaction conditions: 1 mL mixture of 10% CH_4 and 90% O_2, 300 W Xe lamp. Along the direction of the arrow, the samples are without catalyst, Pt-NNB-1, Pt-NNB-1-LD, NNB-8, Pt-NNB-8, Pt-NNB-8-LD, and NNB-1, respectively. (e) SEM image of Pt–NNB-1 sample prepared by the impregnation method. (f) Illustration of charge distribution in single crystal with ordered and disordered arrangement structures. (g) Open circuit photovoltage curves. (h) Photocurrent responses of ordered NNB-1 and disordered NNB-8.[322] Copyright © 2014, Royal Society of Chemistry.

direction was beneficial for the directional charge transfer. Thus, the advantage of ordered ferroelectrics in charge separation/transfer dynamics was proved in this work.

Furthermore, to achieve the high selectivity of POM over photocatalysts, precise control of the surface polarity on ferroelectric materials is a credible strategy after the separation of electron–hole pairs is completed. In the CH_4 to CH_3OH conversion process, CH_4 can interact with $^{\bullet}OH$ on the oxidizing surface with negative polarity to produce CH_3OH.[22] The state of the surface is then switched to positive polarization with reducibility, allowing the O_2 molecules to complete the dissociation. Due to the addition of O_2, the surface is ready to oxide CH_4 again. The whole cycle is therefore advantageous for the partial oxidization of CH_4 to CH_3OH instead of other products. However, Arvin Kakekhani *et al.* suggested that this theory also has some potential challenges according to DFT results. Firstly, the surface oxygens could couple with the neighbouring oxygen to form O_2. In fact, the barrier to O_2 leaving the surface is much lower than that for direct oxidation of CH_4, suggesting that the dissociated oxygen may not participate in the oxidation reaction. Secondly, before CH_3OH leaves the ferroelectric materials, the products undergo a reverse reaction to dissociate back into CH_4 and surface oxygens when the surface state changes to positive polarization. Some groups have attempted to overcome these shortcomings in various photocatalytic applications by using monolayers of transition metal oxides.[324] As an example, ZnO monolayer on $PbTiO_3$ ferroelectric photocatalysts. Through the dynamically tuned catalysis mechanism, the energy barrier for CO_2 conversion was obviously lowered.[325] In addition, the CrO_2-based monolayer also promotes NO_x dissociation and CO oxidation over the $PbTiO_3$ substrate. And the switchable polarity between strong and weak binding achieved rapid dissociation and easy desorption simultaneously, avoiding oxygen and sulfur poisoning.[319] Recently, Yi *et al.* investigated the influence of polar and non-polar facets in methane oxidation based on ZnO ferroelectric photocatalysts.[326] The ZnO nanosheets and nanorods were prepared to compare the influence of facets with different polar states (Fig. 16a and b). Compared to nanosheets with polar facets, ZnO nanorods mostly contained non-polar facets (Fig. 16c). The photocatalytic oxidation of CH_4 showed distinct morphology dependence characteristics (Fig. 16d). Due to the polarization in ZnO nanosheets, the methane could be rapidly oxidated. However, ZnO nanorods showed a lower rate of photocatalytic CH_4 oxidation under the same conditions. The CH_4 oxidation followed the quasi-first-order reaction kinetics (Fig. 16e). The rate constants were 0.01 and 8.01×10^{-4} min^{-1} for ZnO nanosheets and nanorods, respectively. These results indicated the significant enhancement effect of polar facets over ZnO nanosheets in CH_4 oxidation. High-energy polar facets are thermodynamically more reactive than non-polar facets, inducing polarity in stable and symmetric CH_4 molecules. During the PEC measurements, ZnO nanosheets had higher photocurrent (Fig. 16f), which could be attributed to more polar facets in ZnO nanosheets. Furthermore, the authors proposed the relationship between CH_4 activation and polar facets in ZnO nanostructures. As a ferroelectric material, the polar semiconductor property of ZnO could be viewed as alternately stacking multilayers of Zn^{2+} and O^{2-} ions with tetrahedral coordination structure along the *c*-axis. This unique structure endowed ZnO with a built-in electric field. When CH_4 was

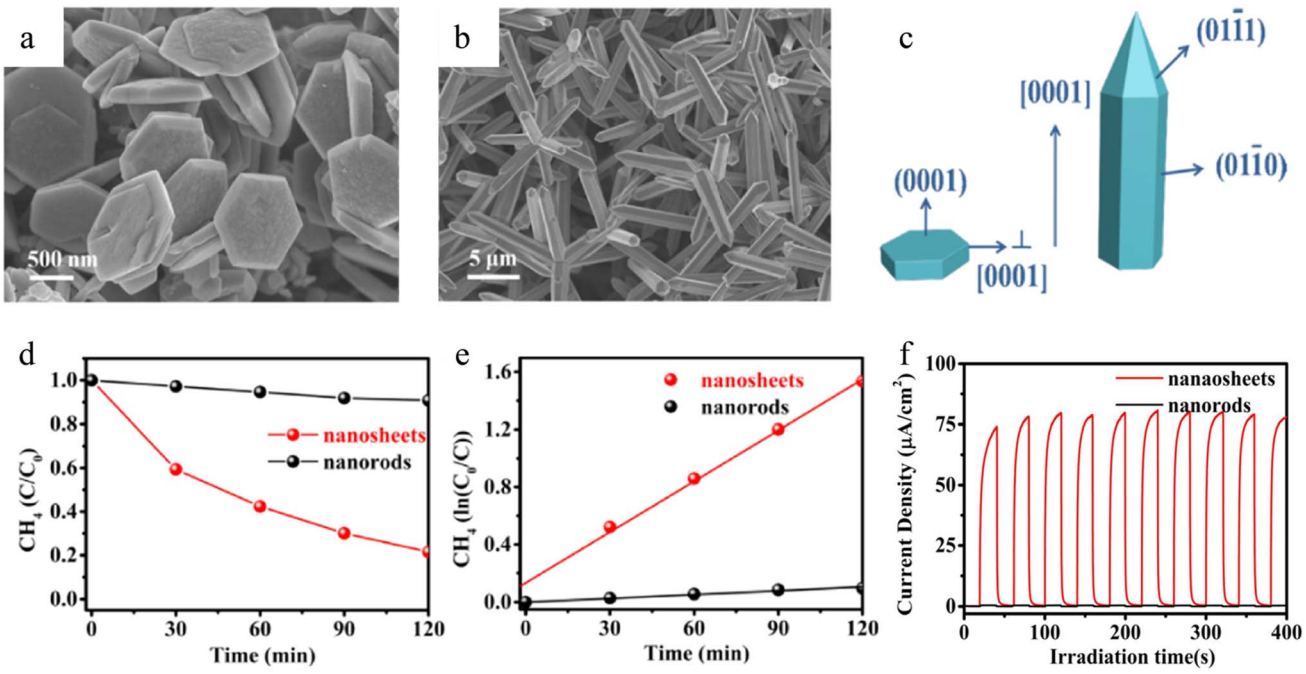

Fig. 16 FESEM of the ZnO (a) nanosheets and (b) nanorods. (c) Growth models of ZnO. (d) Time course and (e) reaction kinetic plots of POM under simulated solar light over the ZnO. Reaction conditions: 200 ppm CH_4, Xe lamp (200 mW cm^{-2}). (f) Photocurrent responses of ZnO.[326] Copyright © 2019, American Chemical Society.

adsorbed on the m-plane of ZnO, the $H_3C^{\delta-}$–$H^{\delta+}$ was polarized due to the interaction between $^{\bullet}CH_3$ and $^{\bullet}H$ and active sites over the m-facets. Meanwhile, the light illumination activated the C–H bond in CH_4, the formation of free $^{\bullet}CH_3$ and $^{\bullet}H$. On the other hand, the generation of oxygen species (activation of O_2 molecules) would take place on the polar (0001) plane, forming $^{\bullet}O_2^-$ radicals. Finally, $^{\bullet}O_2^-$ would oxidize the intermediate to produce the products (CO_2 and H_2O). Although the products in this work were not high value-added chemicals, the above work indeed demonstrates the potential of an epitaxial monolayer of a transition metal oxide in the activation of reactants over the specific facet with polarization. Thus, the development of specific surface layers is beneficial to fully exploit the ferroelectric photocatalysts in POM application.

4.3. Ferroelectric-assisted photocatalytic OCM

Compared to the conventional thermal catalytic OCM process, photocatalytic OCM focuses on the inhibition of competitive reaction and overoxidation under mild conditions. From this perspective, ferroelectric materials are a suitable candidate for enhancing photocatalytic OCM efficiency. However, few studies reported that ferroelectric materials are used in the thermal catalytic or photocatalytic OCM field. Thus, in this section, the feasibility and possible advantages of ferroelectric-assisted OCM systems will be discussed to encourage more ferroelectrics to be developed for OCM applications. Firstly, both ferroelectric-based photocatalysts and ferroelectric cocatalysts could form an electric field due to intrinsic spontaneous polarization. The electric field would function as the above noble metal cocatalysts that become the charge acceptor *via* adjusting the electrons and holes to transfer onto the surface with different polarized states. Secondly, ferroelectric polarization could avoid some unfavorable effects from O_2 by actively toggling the surface–absorbate interaction. Using $PbTiO_3$ as an example, after the dissociation of O_2 in the reactants, each oxygen adsorbate could bind to the surface oxygen atom, forming a surface O_2 molecule. In negative polarization, the surface O_2 molecules have very low dissociative binding energy. On the contrary, the interaction between positively polarized surface and surface O_2 molecules is strong. Table 2 exhibits the binding energies for the surface O_2 molecule.[22] A positive number means the binding is favourable. Conversely, a negative number indicates a metastable state that is more unfavourable than O_2. Indeed, this is meaningful for photocatalytic OCM applications because the overoxidation and inactivation from adsorbed O_2 could be eliminated by controlling the polar state on ferroelectric catalysts (or cocatalysts). Finally, similar to the above-mentioned plasma-assisted photocatalysts, some novel reaction pathways of the OCM process might be found in the ferroelectric-assisted photocatalytic systems.[231] Because the local surface state was changed by polarization, the localized electric field in ferroelectric materials probably led to some different intermediates or initiated OCM reactions by other oxidants except O_2 and H_2O_2. Thereby, it is feasible to efficiently convert CH_4 into high-value-added C_2 products over photocatalysts containing ferroelectric materials.

Table 2 Intact and dissociative binding energies toward one O_2 molecule on PTO as a function of polarization relative to O_2 in a vacuum[22]

Polarization status	Intact binding energy [eV]	Dissociative binding energy [eV]
Positive	2.4	2.6
Paraelectric	0.2	−0.8
Negative	0	0.4

4.4. Ferroelectric-assisted photocatalytic NOCM

Although photocatalytic NOCM has many advantages, unfortunately, the evolution rate of C_2H_6 from the photocatalytic NOCM reaction is almost an unexplored field. It is very urgent to design more efficient photocatalysts for NOCM. Several aspects should be considered for the reasonable development of NOCM photocatalysts. First, a strong local electric field may be needed to easily polarize and nucleophilically or electrophilically attack CH_4. From this perspective, ferroelectric material is a suitable candidate to improve the efficiency of photocatalytic NOCM. However, few studies used ferroelectric materials in the NOCM field. Second, metallic co-catalysts are dynamically necessary for the occurrence of the half-reaction of H_2 generation because the large overpotential inhibits the release of H_2 across the bare oxide surface. In order to simultaneously address the above challenges, an Au/ZnO porous nanosheet with a local electric field and polar facet was designed for photocatalytic NOCM by Long's group.[327] A ZnO crystal was tailored to expose [001] facet with polarized property, beneficial for the CH_4 activation (Fig. 17a). Au/m-ZnO showed a bandgap absorption at *ca.* 395 nm and a broad absorption peak from plasmonic Au NPs (Fig. 17b). The as-prepared Au/m-ZnO samples achieved the highest evolution rates of C_2H_6 and H_2. Further, the reaction mechanism of NOCM was investigated under different reactive atmospheres. Compared to the pure CH_4 atmosphere, the C_2H_6 production was increased by O_2 and H_2O and decreased by CO_2. However, the H_2 evolution rate was decreased in the order of pure CH_4 > $CH_4 + H_2O$ > $CH_4 + CO_2$ > $CH_4 + O_2$. Thus, it could be assumed that CO_2 did not favor the NOCM because CO_2 is competitive for photoelectrons and inhibits the dehydrogenation process, which is an important process for CH_4 activation. The decrease in H_2 production could be attributed to the side reaction $CH_4 + CO_2 \rightarrow CH_3COO^- + H^+$, which would cause the stoichiometric mismatch between H_2 and C_2H_6. Under O_2-free conditions, C_2H_6 and H_2 yields could remain stoichiometrically matched ($C_2H_6 : H_2 = 1:1$), indicating that the photocatalytic NOCM proceeds by a dehydrogenative process. *In situ* electron spin resonance (ESR) results showed the coupling between electron-occupied oxygen vacancy (V_O^+) and diamagnetic oxygen ion (O^-) according to the characteristic peaks at 1.960 and 1.957 (Fig. 17c and d). However, light illumination did not change the V_O^+ signal, indicating the lattice O atoms have no effect on the NOCM process. Thus, the dehydrogenative coupling occurred at the Zn^{2+} atoms. CH_4 was polarized by the Zn plane, resulting in $H^{\delta+}$–$CH_3^{\delta-}$ polarization to generate $^{\bullet}CH_3$ radical and H^+ *via* the

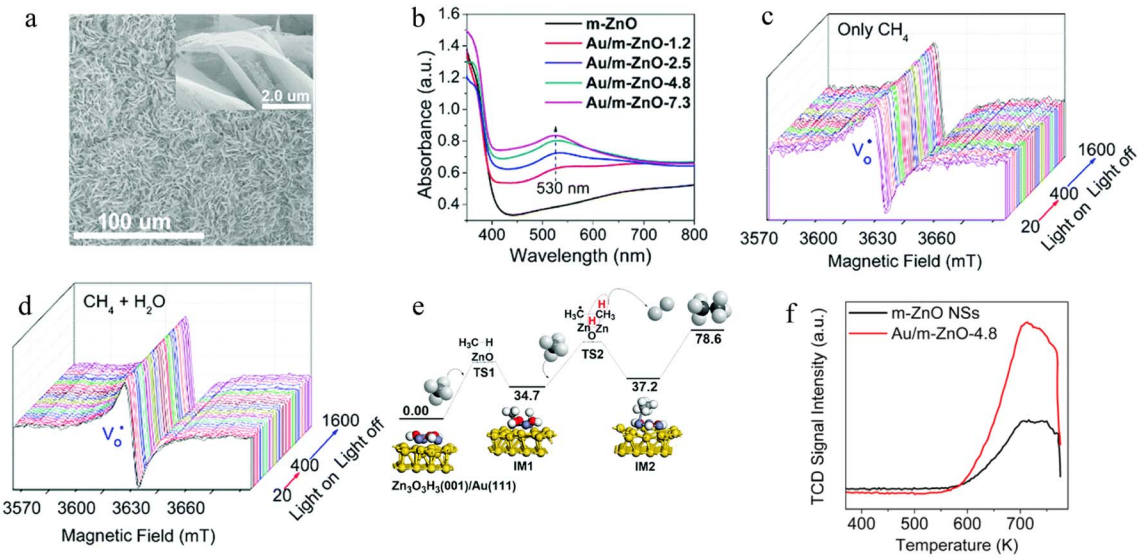

Fig. 17 (a) SEM image of Au/m-ZnO-4.8. (b) UV-vis spectra. *In situ* ESR spectra of (c) Au/m-ZnO-4.8 under CH_4 atmosphere and (d) O deficiency under CH_4/H_2O atmospheres. (e) Energy barrier of NOCM on $Zn_3O_3H_3$(001)/Au(111). (f) CH_4-TPD patterns.[327] Copyright © 2018, Royal Society of Chemistry.

photoelectron transfer between ZnO and CH_4. The plasmonic hot electrons on Au NPs promoted the H_2 formation. DFT studies calculated the energy barrier of NOCM on Au/ZnO photocatalyst (Fig. 17e). The results showed the advantage of the polar Zn(001) surface in the generation of C_2H_6. The charge analysis showed the interaction in charge transfer between ZnO and Au, which means that Au activated the ZnO surface and enhanced the CH_4 chemisorption. Meanwhile, the CH_4-TPD results proved the enhancement of the CH_4 dissociation on the (001) facet by the electric field coupling (Fig. 17f). Therefore, this work provided convincing evidence for the important role of the synergistic effect between ZnO ferroelectric material and Au plasma in accelerating the CH_4 activation and charge-carrier interaction.

5. Potential role of ferroelectric effect during photocatalytic methane conversion

Based on the previous studies with convincing evidence of the influence of ferroelectric materials on photocatalytic processes, the potential effects of ferroelectrics on the photocatalytic methane conversion field can be summarized as follows:

5.1. Promoting charge transfer

As a general effect, the polarization and corresponding built-in electric field are always mentioned and widely utilized when researchers purposely introduce ferroelectric materials into different photocatalytic systems. Considering that photocatalytic methane conversion systems must follow the general steps of photocatalysis, the sustainable internal electric field derived from ferroelectric properties should enhance charge-carrier transfer kinetics in this specific process.[328] Meanwhile, as mentioned before (Section 3.3.2), different polar surfaces will lead to the separation of reduction and oxidation processes. This also adjusts the transfer routes of electrons and holes towards different surface sites, decreasing the recombination possibility. In addition, the spatial selectivity of charges over the ferroelectrics surface leads to energy band bending at the interface when the polarized surface contacts with solution.[329] This characteristic has been widely used in both photocatalytic and electrocatalytic systems, because the negative surface/electrode causes upward band bending, promoting the charge migration from electrolyte/reactants to catalysts. On the contrary, the positive surface/electrode leads to downward band bending, enhancing charge transfer from ferroelectric catalysts to electrolyte/reactants.[330]

5.2. Promoting reactant adsorption/activation

Although light illumination can directly promote chemical bond cracking, the high C–H bond energy of this small hydrocarbon molecule (CH_4: ~440 kJ mol^{-1}) might arouse a suspicion: is the light energy enough to complete the CH_4 association? In this case, the photoexcited radical species ($^{\bullet}OH$ and h^+) should be more reliable in order to activate CH_4 molecules. From this view, ferroelectric materials are able to create a negatively polarized surface, which is beneficial to oxygen-containing active species, and further oxidizes CH_4 to intermediates or CH_3OH.[147] Depending on the atmosphere in the reaction systems, the intermediates (*i.e.* $^{\bullet}CH_3$) will take part in the NOCM or OCM to obtain CO, CH_3OH, or C_2 products like C_2H_6 as reviewed in the previous sections. Another potential effect for accelerating reactant activation over ferroelectric surfaces might be the adsorption–desorption enhancement. It has been reported that the adsorption–desorption properties of ferroelectric materials can be tuned according to the molecules

polarity.[331,332] Even if CH_4 is a non-polar molecule, products like CO and CH_3OH are polar molecules. This suggests the surface states can be automatically switched during CH_4 conversion processes, promoting reactant adsorption and subsequent activation, ensuring long-term reaction cycles. Further, DFT calculations have confirmed that 2D ferroelectric materials are able to control the adsorption energies, electron transfer, and magnetic moment of adsorbed reactant molecules so that there was a polarization-dependent gas adsorption behaviour over the monolayer surface.[333]

5.3. Improving selectivity

Ferroelectric materials are able to switch reaction pathways to obtain desired products without stopping the reaction process and changing catalysts, demonstrating the great potential for achieving high selectivity during methane conversion systems.[334] One approach to control the selectivity is the surface polarization. When the absorbance is saturated, the negative surface state will be switched to a positive state reducing oxygen species so that the overoxidation can be inhibited. Therefore, complex methane conversions can achieve high selectivity over a polarized surface.[335] Besides, the selective adsorption of reactants on the polarized surface can effectively lift the limitations imposed by Sabatier's principle.[336] For instance, the ferroelectric $BiFeO_3$ could reduce the charge recombination rate from 17 to 0.6 s^{-1} so that increased 4.4 times the photoelectric efficiency.[337] The improvement should be attributed to the compensation effect through electronic reconstruction when a built-in electric field promotes electron–hole separation.[319,338] The changes in electron distribution lead to different abilities of polarized surfaces towards oxidation or reduction reactions. Thus, the switchable ferroelectric polarization allows us to control the surface affinity to desired redox reactions. Because ferroelectric materials always have large band gaps and dielectric constants, using ferroelectrics as triggers to control the dissociation of specific small hydrocarbon molecules has been reported as a strategy to tune the chemical selectivity.[325] The ferroelectric matrix could dynamically reduce the reaction barrier through polarization manipulation to affect the local reaction pathways.[339] In addition to changing the surface properties and reaction routes, recently, a novel idea to control the selectivity based on ferroelectric materials is using a ferroelectric field to immobilize active sites (*i.e.* cocatalyst on photocatalyst).[340,341] To be specific, during methane conversion reactions, depositing at cocatalyst with a strong ability towards CH_4 cracking over a holes-accumulated surface under the assistance of a ferroelectric field promoted the directional oxidation of CH_4 molecules and the reversible reactions could be inhibited. However, the real implementation of ferroelectric photocatalysts with ideal selectivity is still challenging due to the large gap between theoretical predictions and practical paradigms. Up to now, these predictions have been mainly realized in CO_2RR and NRR systems or ferroelectric electrocatalysts. These works make us hold strong confidence that ferroelectric systems should be widely and practically utilized in photocatalytic methane conversion reactions in the near future.

6. Conclusions and outlook

The utilization of CH_4 is one of the crucial steps in the transition from a fossil fuel energy system to a sustainable energy system. The mainstream sources for renewably obtaining CH_4 are currently based on anaerobic digesters, which convert cow manure into natural gas, and CO_2-based green chemistry transfer routes, such as biochemical, (photo)electrochemical, and photo(thermal) catalytic methods.[342] Globally, more than 50% of H_2 is produced through the reforming of CH_4.[343] Additionally, by producing higher hydrocarbons, various conversion routes of methane are crucial to reducing the greenhouse gas and achieving carbon neutralization. Therefore, clean production and sustainable utilization of CH_4 seem like a complete and ideal strategy to deal with energy shortages and environmental problems.

However, the C–H bond strength in CH_4 is the biggest obstacle to converting CH_4 into added-value products. As mentioned above, many thermal catalysts have been developed to overcome this thermodynamic challenge. Kinetic models and reaction pathways in these thermal catalytic systems are continuously being elucidated. Nevertheless, the high temperature needed for CH_4 conversion processes leads to the inactivation of thermal catalysts and even causes excessive CO_2 emissions. Fortunately, with the extensive studies of environmentally friendly photocatalysts, the harsh reaction conditions needed in thermal catalytic methane conversion are being gradually reduced, indicating that carbon neutralization becomes possible. Currently, an important problem to be solved in photocatalytic methane conversion is the insufficient efficiency mainly due to the slow charge transfer. In this regard, the ferroelectric-based photocatalysts are envisioned to play a key role in manipulating the evolution efficiency and selectivity of products from CH_4 conversion by regulating the transfer kinetics. Many efforts have been made in this interdisciplinary field so far, but some obstacles and deficiencies still exist as follows.

6.1. Development of novel photocatalysts using ferroelectric materials

An increasing number of ferroelectric-assisted photocatalytic systems have been designed and fabricated to participate in reactions that produce the desired chemicals and clean energy fuels (*e.g.*, H_2 from overall water splitting and CO from CO_2 reduction). However, in the catalytic methane conversion field, research based on ferroelectric materials is still rare. Thus, the excellent ability of ferroics should be further developed for improving CH_4 conversion efficiency. One of the possible reasons is that some ferroelectric-based semiconductors do not have suitable energy band structures to generate photoinduced charge carriers with high redox capability. In addition, the work function of certain ferroelectric materials is not sufficient to promote the reduction process when electrons are transferred

to the ferroelectric co-catalyst surface. Thus, energy band engineering is important for the design of ferroelectrics-supported photocatalytic systems. However, it is not practical to synthesize and experimentally test all candidate ferroelectrics to obtain the details of the energy band and work function. DFT calculations and hybrid functional calculations are useful to determine the electronic structure and predict ideal ferroelectric materials with sufficient redox ability and polarized state. However, the high computational cost of these methods should be considered for high throughput calculations. In addition, machine learning (ML) has recently become a highly efficient technique in materials data engineering to estimate various parameters (*e.g.*, E_g, CB, and VB) in materials. Thus, with the improvement and supplementation of organic/inorganic databases, the ML method could provide guidance for the discovery and design of novel energy materials.

6.2. Emphasize the role of the ferroelectric effect

Ferroelectric materials have been widely used in various photo(thermal)catalytic applications, but some works paid too much attention to other properties (*e.g.*, optical properties, absorption/desorption abilities) in as-designed ferroic-based photocatalysts instead of their intrinsic ferroelectric effect. In particular, some outstanding works shown in this review also used ferroelectric materials such as $BiVO_4$ and $SrTiO_3$,[86,192] but the authors only systematically investigated the influence of loaded co-catalyst or elemental doping on the photocatalytic activity or selectivity. To some extent, the reason for this problem is that the ferroelectric effect was not considered in the key points during the initial design process. However, it is known that the photocatalytic activity could be affected by various factors, and even a small factor could have a non-negligible effect on the overall photocatalytic efficiency. Therefore, the function of the natural ferroelectric effect and the accompanying built-in electric field should gain more interest when using ferroelectric materials not only for methane conversion reactions but also for photocatalytic applications in general.

6.3. Exploring new effects from ferroelectric materials

During the photocatalytic reactions, the electron spin phenomenon plays an important role in electron migration and thus photocatalytic efficiency. The electron spin could be regulated by external fields like magnetic and electric fields.[344] In detail, the spin–orbit coupling is able to change the spin orientation of both electrons and holes from semiconductors. Then the recombination between photoinduced charges will be inhibited. The electrons scatter can gradually decrease the impact from spin polarization, meaning that the spin polarization with a longer lifetime can effectively promote charge separation and transfer. From this perspective, a series of ferroelectrics with a magnetic response called the magnetoelectric effect, could be a new path toward ferroelectrics-based control of electron spin. It has been confirmed that some single-phase ferroelectric materials like $BiFeO_3$ could adjust the spin behaviour *via* the interaction between intrinsic coupling between electric and magnetic order parameters.[345,346] Some works also discussed the influence of spin polarization in the photocatalytic process.[344] However, in the photocatalytic field, the investigation on the control of photoexcited electrons spin *via* ferroelectric materials is still scarce, and this blank is no exception in methane conversion areas. With the development of theories about ferroelectric materials, the spin-related mechanisms in ferroelectrics should obtain more attention for full utilization in practical photocatalytic reactions.

6.4. Design of advanced reaction vectors

To further exploit the advantage of ferroelectric materials for boosting photocatalytic methane conversion, the design or update of reactors must be as important as the development of ferroelectric materials. It has been confirmed that different polarization states lead to the variation of adsorption/desorption behaviour towards reactants on ferroelectric materials. Thus, if the updated reactors are able to periodically control the surface state of ferroelectric photocatalysts, the activity, and selectivity for specific hydrocarbon products, especially C_2 products, will be significantly improved. Similarly, there are some successful examples of piezoelectric/pyroelectric-assisted photocatalytic systems, proving that this proposal is reasonable and feasible. For example, the introduction of an external ultrasonic device to excite the piezoelectric effect, which forms a strong electric field in photocatalysts and thus improves the photocatalytic efficiency. In addition to the external auxiliary device, advanced flow reactors are more effective than conventional batch reactors. Although the operation, cost, and safety are major challenges for the design of flow reactors, some mature flow systems in thermal catalysis are ideal references for photocatalytic gas–solid two-phase reactions. Additionally, some membrane reactors also have unique advantages in separating catalysts from products after reaction, lowering the operating temperature, breaking the restriction of thermodynamic balance, and improving the selectivity and activity. Membrane reactors are expected to achieve the coupling of different photocatalytic applications. Therefore, if more effort is devoted to the development of reactors and assisted devices, ferroelectric-assisted photocatalytic CH_4 conversion will realize industrial application at an early date.

6.5. Coupling of other photocatalytic reactions

Nowadays, (i) most products of methane conversion are raw materials for downstream reactions, and (ii) ferroelectric-based materials have been widely used for photocatalytic applications beyond methane conversion. Taking these two points into account, if some advanced reactors could separate specific products of methane conversion, at least two photocatalytic reactions including methane conversion could be simultaneously and continuously conducted on ferroelectric photocatalysts. In this case, the cost of industrial production could be significantly reduced by eliminating the transportation and storage of intermediate raw materials. Meanwhile, other labour costs and space occupied by chemical production equipment,

which are difficult to calculate, could also be saved by reaction coupling. However, to realize this goal, it is necessary to fabricate excellent (ferroelectric-based)photocatalysts and the aforementioned novel reaction vectors to overcome the complex requirements of various catalytic reactions.

6.6. Investigation of enhancement and reaction mechanism

Compared with much scientific research focused on the development of novel photocatalysts, few mechanisms are known about each methane conversion technology. The transient intermediates and local reaction pathways need to be studied in detail because the surface state of ferroelectric materials may be changed during CH_4 conversion. Beyond the reaction mechanism, little evidence has been provided to directly show the effect of polarization on charge transfer dynamics at the nano or micro-scale. Although some works claimed that electrons and holes would separate to different locations under the influence of the ferroelectric effect, more characterization data should be provided to demonstrate the migration or bias of photoexcited charge carriers. For this problem, a series of advanced characterization methods, such as *in situ* Fourier transform infrared spectroscopy (FT-IR), *in situ* X-ray photoelectron spectroscopy, piezoresponse force microscopy (PMF), and molecular probe technology, were integrated with DFT-based calculations to clarify both the enhancement and the reaction mechanism in the photocatalytic field. It is expected these advanced characterization methods will provide a deeper insight into the ferroelectric-assisted methane conversion field.

It is undeniable that some high-level methane conversion routes are still at a very early stage and that ferroelectric-assisted catalysis, especially in the photocatalytic field, is far from industrial applications. However, this multidisciplinary field could develop rapidly with the presence of a new generation of advanced characterization techniques and chemical synthesis strategies. It is expected that more studies on ferroelectric-assisted photocatalytic methane conversion will be carried out in the coming years.

Data availability

No primary research results, software or code have been included and no new data were generated or analysed as part of this review.

Conflicts of interest

There are no conflicts to declare.

Acknowledgements

Y. L. acknowledges the program of China Scholarships Council (No. 202206250016). X. S. thanks ICREA for the ICREA Academia Prize 2020. X. S. and J. G.-A. thank MINECO/FEDER for financial support (PID2019-104171RB-I00). J. M. is indebted to the Ramón y Cajal Program (RYC2021-033820-I fellowship) funded by MCIN/AEI/10.13039/501100011033 and by the European Union "NextGenerationEU/PRTR".

References

1 X. Jiang, X. Nie, X. Guo, C. Song and J. G. Chen, *Chem. Rev.*, 2020, **120**, 7984.
2 S. N. Habisreutinger, L. Schmidt-Mende and J. K. Stolarczyk, *Angew. Chem., Int. Ed.*, 2013, **52**, 7372.
3 H. Weldekidan, V. Strezov and G. Town, *Renewable Sustainable Energy Rev.*, 2018, **88**, 184.
4 J. O. Metzger and A. Hüttermann, *Naturwissenschaften*, 2009, **96**, 279.
5 S. Morales, R. Miranda, D. Bustos, T. Cazares and H. Tran, *J. Anal. Appl. Pyrolysis*, 2014, **109**, 65.
6 J. Ran, H. Zhang, J. Qu, J. Shan, K. Davey, J. M. Cairney, L. Jing and S. Qiao, *Small*, 2021, **17**, 2100296.
7 B. Xia, Y. Zhang, J. Ran, M. Jaroniec and S. Qiao, *ACS Cent. Sci.*, 2021, **7**, 39.
8 B. L. Farrell, V. O. Igenegbai and S. Linic, *ACS Catal.*, 2016, **6**, 4340.
9 E. McFarland, *Science*, 2012, **338**, 340.
10 U.S., Energy Information Administration (EIA), Annual Energy Outlook 2019, 2019.
11 X. Meng, X. Cui, N. P. Rajan, L. Yu, D. Deng and X. Bao, *Chem*, 2019, **5**, 2296.
12 D. E. Holmes and J. A. Smith, *Adv. Appl. Microbiol.*, 2016, 1–61.
13 X. Li, C. Wang and J. Tang, *Nat. Rev. Mater.*, 2022, **7**, 617.
14 P. Schwach, X. Pan and X. Bao, *Chem. Rev.*, 2017, **117**, 8497.
15 H. Song, X. Meng, Z. J. Wang, Z. Wang, H. Chen, Y. Weng, F. Ichihara, M. Oshikiri, T. Kako and J. Ye, *ACS Catal.*, 2018, **8**, 7556.
16 X. Yu, V. De Waele, A. Löfberg, V. Ordomsky and A. Y. Khodakov, *Nat. Commun.*, 2019, **10**, 700.
17 M. A. Gondal, A. Hameed, Z. H. Yamani and A. Arfaj, *Chem. Phys. Lett.*, 2004, **392**, 372.
18 H. Yoshida, K. Hirao, J. I. Nishimoto, K. Shimura, S. Kato, H. Itoh and T. Hattori, *J. Phys. Chem. C*, 2008, **112**, 5542.
19 W. Zhang, Y. Yu and Z. Yi, *J. Mater. Sci.*, 2017, **52**, 5106.
20 N. J. Gunsalus, A. Koppaka, S. H. Park, S. M. Bischof, B. G. Hashiguchi and R. A. Periana, *Chem. Rev.*, 2017, **117**, 8521.
21 L. Yuliati and H. Yoshida, *Chem. Soc. Rev.*, 2008, **37**, 1592.
22 A. Kakekhani and S. Ismail-Beigi, *Phys. Chem. Chem. Phys.*, 2016, **18**, 19676.
23 Y. Song, E. Ozdemir, S. Ramesh, A. Adishev, S. Subramanian, A. Harale, M. Albuali, B. A. Fadhel, A. Jamal, D. Moon, S. H. Choi and C. T. Yavuz, *Science*, 2020, **367**, 777.
24 D. Kong, Y. Zheng, M. Kobielusz, Y. Wang, Z. Bai, W. Macyk, X. Wang and J. Tang, *Mater. Today*, 2018, **21**, 897.
25 C. Jiang, S. J. A. Moniz, A. Wang, T. Zhang and J. Tang, *Chem. Soc. Rev.*, 2017, **46**, 4645.
26 S. J. A. Moniz, S. A. Shevlin, D. J. Martin, Z.-X. Guo and J. Tang, *Energy Environ. Sci.*, 2015, **8**, 731.
27 K. Shimura and H. Yoshida, *Catal. Surv. Asia*, 2014, **18**, 24.
28 J. Xie, R. Jin, A. Li, Y. Bi, Q. Ruan, Y. Deng, Y. Zhang, S. Yao, G. Sankar, D. Ma and J. Tang, *Nat. Catal.*, 2018, **1**, 889.

29 Y. Wang, H. Suzuki, J. Xie, O. Tomita, D. J. Martin, M. Higashi, D. Kong, R. Abe and J. Tang, *Chem. Rev.*, 2018, **118**, 5201.
30 H. Li, J. Shang, Z. Ai and L. Zhang, *J. Am. Chem. Soc.*, 2018, **140**, 526.
31 Y. Lei, Z. Jia, H. Hu, L. Liu, J. Ye and D. Wang, *Catalysts*, 2022, **12**, 1323.
32 J. Wen, J. Xie, X. Chen and X. Li, *Appl. Surf. Sci.*, 2017, **391**, 72.
33 H. Tong, S. Ouyang, Y. Bi, N. Umezawa, M. Oshikiri and J. Ye, *Adv. Mater.*, 2012, **24**, 229.
34 T. M. Khedr, K. Wang, D. Kowalski, S. M. El-Sheikh, H. M. Abdeldayem, B. Ohtani and E. Kowalska, *J. Environ. Chem. Eng.*, 2022, **10**, 107838.
35 P. Jiménez-Calvo, V. Caps and V. Keller, Plasmonic Au-based junctions onto TiO2, gC3N4, and TiO2-gC3N4 systems for photocatalytic hydrogen production: Fundamentals and challenges, *Renewable Sustainable Energy Rev.*, 2021, **149**, 111095.
36 Z. Zhao, H. Tan, H. Zhao, Y. Lv, L. J. Zhou, Y. Song and Z. Sun, *Chem. Commun.*, 2014, **50**, 2755.
37 R. Leary and A. Westwood, *Carbon*, 2011, **49**, 741.
38 B. Dai, J. Fang, Y. Yu, M. Sun, H. Huang, C. Lu, J. Kou, Y. Zhao and Z. Xu, *Adv. Mater.*, 2020, **32**, 1906361.
39 L. Liu, S. Ouyang and J. Ye, *Angew. Chem., Int. Ed.*, 2013, **52**, 6689.
40 X. Xu, F. Luo, W. Tang, J. Hu, H. Zeng and Y. Zhou, *Adv. Funct. Mater.*, 2018, **28**, 1804055.
41 L. Yin, M. Zhao, H. Hu, J. Ye and D. Wang, *Chin. J. Catal.*, 2017, **38**, 1307.
42 J. Tan, X. Wang, W. Hou, X. Zhang, L. Liu, J. Ye and D. Wang, *J. Alloys Compd.*, 2019, **792**, 918.
43 M. Ye, X. Wang, E. Liu, J. Ye and D. Wang, *ChemSusChem*, 2018, **11**, 1606.
44 J. Li, Z. Wang, H. Chen, Q. Zhang, H. Hu, L. Liu, J. Ye and D. Wang, *Catal. Sci. Technol.*, 2021, **11**, 4953.
45 P. Li, L. Liu, W. An, H. Wang, H. Guo, Y. Liang and W. Cui, *Appl. Catal., B*, 2020, **266**, 118618.
46 A. Meng, L. Zhang, B. Cheng and J. Yu, *Adv. Mater.*, 2019, **31**, 1807660.
47 C. C. Hu and H. Teng, *J. Catal.*, 2010, **272**, 1.
48 C. Liu, J. Qian, Y. Ye, H. Zhou, C.-J. Sun, C. Sheehan, Z. Zhang, G. Wan, Y.-S. Liu, J. Guo, S. Li, H. Shin, S. Hwang, T. B. Gunnoe, W. A. Goddard and S. Zhang, *Nat. Catal.*, 2020, **4**, 36.
49 Z. Jia, S. Ning, Y. Tong, X. Chen, H. Hu, L. Liu, J. Ye and D. Wang, *ACS Appl. Nano Mater.*, 2021, **4**, 10485.
50 H. Zhao, P. Jiang and W. Cai, *Chem.–Asian J.*, 2017, **12**, 361.
51 C. Han, L. Ge, C. Chen, Y. Li, X. Xiao, Y. Zhang and L. Guo, *Appl. Catal., B*, 2014, **147**, 546.
52 Q. Yu, Y. Dai, Y. Ling, Q. Wu, Z. Zhang and B. Feng, *J. Environ. Chem. Eng.*, 2022, **10**, 108693.
53 J. Yang, T. Liu, H. Zhou, W. Cao, C. Chen, X. He, C. Jiang, Y. Li and Y. Wang, *J. Alloys Compd.*, 2022, **900**, 163440.
54 H. Gao, P. Zhang, J. Hu, J. Pan, J. Fan and G. Shao, *Appl. Surf. Sci.*, 2017, **391**, 211.
55 Y. Lei, J. Ye, J. García-Antón and H. Liu, *Chin. J. Catal.*, 2023, **53**, 72.
56 P. S. Bednyakov, T. Sluka, A. K. Tagantsev, D. Damjanovic and N. Setter, *Sci. Rep.*, 2015, **5**, 15819.
57 X. Liu, F. Zhang, P. Long, T. Lu, H. Zeng, Y. Liu, R. L. Withers, Y. Li and Z. Yi, *Adv. Mater.*, 2018, **30**, 1801619.
58 H. Li, X. Quan, S. Chen and H. Yu, *Appl. Catal., B*, 2017, **209**, 591.
59 H. Simons, A. B. Haugen, A. C. Jakobsen, S. Schmidt, F. Stöhr, M. Majkut, C. Detlefs, J. E. Daniels, D. Damjanovic and H. F. Poulsen, *Nat. Mater.*, 2018, **17**, 814.
60 B. Dai, Y. Yu, Y. Chen, H. Huang, C. Lu, J. Kou, Y. Zhao and Z. Xu, *Adv. Funct. Mater.*, 2019, **29**, 1970105.
61 X. Chen, Y. Li, X. Pan, D. Cortie, X. Huang and Z. Yi, *Nat. Commun.*, 2016, **7**, 12273.
62 H. Kato, K. Asakura and A. Kudo, *J. Am. Chem. Soc.*, 2003, **125**, 3082.
63 J. C. Yang, Y. L. Huang, Q. He and Y. H. Chu, *J. Appl. Phys.*, 2014, **116**, 066801.
64 A. S. Pisat, G. S. Rohrer and P. A. Salvador, *Semicond. Sci. Technol.*, 2017, **32**, 103001.
65 Y. Cui, J. Briscoe and S. Dunn, *Chem. Mater.*, 2013, **25**, 4215.
66 H. Kanda, N. Shibayama, A. J. Huckaba, Y. Lee, S. Paek, N. Klipfel, C. Roldán-Carmona, V. I. E. Queloz, G. Grancini, Y. Zhang, M. Abuhelaiqa, K. T. Cho, M. Li, M. D. Mensi, S. Kinge and M. K. Nazeeruddin, *Energy Environ. Sci.*, 2020, **13**, 1222.
67 H. Huang, S. Tu, X. Du and Y. Zhang, *J. Colloid Interface Sci.*, 2018, **509**, 113.
68 C. Paillard, X. Bai, I. C. Infante, M. Guennou, G. Geneste, M. Alexe, J. Kreisel and B. Dkhil, *Adv. Mater.*, 2016, **28**, 5153.
69 F. Chen, H. Huang, L. Guo, Y. Zhang and T. Ma, *Angew. Chem.*, 2019, **131**, 10164.
70 W. Song, P. A. Salvador and G. S. Rohrer, *ACS Appl. Mater. Interfaces*, 2018, **10**, 41450.
71 O. Kwon, D. Seol, D. Lee, H. Han, I. Lindfors-Vrejoiu, W. Lee, S. Jesse, H. N. Lee, S. V. Kalinin, M. Alexe and Y. Kim, *Adv. Mater.*, 2018, **30**, 1703675.
72 J. He, Y. Zhao, S. Jiang and S. Song, *Sol. RRL*, 2021, **5**, 2000446.
73 P. Wang, R. Shi, J. Zhao and T. Zhang, *Adv. Sci.*, 2024, **11**, 2305471.
74 J. Wang and S. Wang, *Coord. Chem. Rev.*, 2022, **453**, 214338.
75 Q. Luo, C. Lu, L. Liu and M. Zhu, *Green Energy Environ.*, 2023, **8**, 406.
76 X. Yu, V. L. Zholobenko, S. Moldovan, D. Hu, D. Wu, V. V. Ordomsky and A. Y. Khodakov, *Nat. Energy*, 2020, **5**, 511.
77 H. Song, X. Meng, S. Wang, W. Zhou, X. Wang, T. Kako and J. Ye, *J. Am. Chem. Soc.*, 2019, **141**, 20507.
78 K. Wang, L. Luo, C. Wang and J. Tang, *Chin. J. Catal.*, 2023, **46**, 103.
79 G.-X. Dong, M.-R. Zhang, K. Su, Z.-L. Liu, M. Zhang and T.-B. Lu, *J. Mater. Chem. A*, 2023, **11**, 9989.
80 S. Murcia-López, K. Villa, T. Andreu and J. R. Morante, *ACS Catal.*, 2014, **4**, 3013.

81 J. Yang, J. Hao, J. Wei, J. Dai and Y. Li, *Fuel*, 2020, **266**, 117104.
82 S. Murcia-López, K. Villa, T. Andreu and J. R. Morante, *ACS Catal.*, 2014, **4**, 3013.
83 H. Wei, J. Cai, Y. Zhang, X. Zhang, E. A. Baranova, J. Cui, Y. Wang, X. Shu, Y. Qin, J. Liu and Y. Wu, *RSC Adv.*, 2020, **10**, 42619.
84 F. P. Koffyberg and F. A. Benko, *J. Appl. Phys.*, 1982, **53**, 1173.
85 X. Li, J. Xie, H. Rao, C. Wang and J. Tang, *Angew. Chem., Int. Ed.*, 2020, **59**, 19702.
86 S. Shoji, X. Peng, A. Yamaguchi, R. Watanabe, C. Fukuhara, Y. Cho, T. Yamamoto, S. Matsumura, M.-W. Yu, S. Ishii, T. Fujita, H. Abe and M. Miyauchi, *Nat. Catal.*, 2020, **3**, 148.
87 G. A. Ozin and F. Hugues, *J. Phys. Chem.*, 1982, **86**, 5174.
88 W. Hill, B. N. Shelimov and V. B. Kazansky, *J. Chem. Soc., Faraday Trans. 1*, 1987, **83**, 2381.
89 L. Yuliati, T. Hattori, H. Itoh and H. Yoshida, *J. Catal.*, 2008, **257**, 396.
90 J. Wen, J. Xie, X. Chen and X. Li, *Appl. Surf. Sci.*, 2017, **391**, 72.
91 D. Masih, Y. Ma and S. Rohani, *Appl. Catal., B*, 2017, **206**, 556.
92 N. Li, Y. Li, R. Jiang, J. Zhou and M. Liu, *Appl. Surf. Sci.*, 2019, **498**, 143861.
93 A. Muhammad, M. Tahir, S. S. Al-Shahrani, A. Mahmood Ali and S. U. Rather, *Appl. Surf. Sci.*, 2020, **504**, 144177.
94 S. Shi, Z. Sun, C. Bao, T. Gao and Y. H. Hu, *Int. J. Energy Res.*, 2020, **44**, 2740.
95 Y. Zhou, L. Zhang and W. Wang, *Nat. Commun.*, 2019, **10**, 506.
96 L. Li, S. Fan, X. Mu, Z. Mi and C.-J. Li, *J. Am. Chem. Soc.*, 2014, **136**, 7793.
97 H. Song, X. Meng, Z. Jun Wang, H. Liu and J. Ye, *Joule*, 2019, **3**, 1606.
98 K. Wittich, M. Krämer, N. Bottke and S. A. Schunk, *ChemCatChem*, 2020, **12**, 2130.
99 G. C. Behera, K. Parida, N. F. Dummer, G. Whiting, N. Sahu, A. F. Carley, M. Conte, G. J. Hutchings and J. K. Bartley, *Catal. Sci. Technol.*, 2013, **3**, 1558.
100 E. Ramírez, R. Soto, R. Bringué, M. Iborra and J. Tejero, *Ind. Eng. Chem. Res.*, 2020, **59**, 20676.
101 J. Li, Y. He, L. Tan, P. Zhang, X. Peng, A. Oruganti, G. Yang, H. Abe, Y. Wang and N. Tsubaki, *Nat. Catal.*, 2018, **1**, 787.
102 C. D. Thomas, A. Cameron, R. E. Green, M. Bakkenes, L. J. Beaumont, Y. C. Collingham, B. F. N. Erasmus, M. F. de Siqueira, A. Grainger, L. Hannah, L. Hughes, B. Huntley, A. S. van Jaarsveld, G. F. Midgley, L. Miles, M. A. Ortega-Huerta, A. Townsend Peterson, O. L. Phillips and S. E. Williams, *Nature*, 2004, **427**, 145.
103 C. Hepburn, E. Adlen, J. Beddington, E. A. Carter, S. Fuss, N. Mac Dowell, J. C. Minx, P. Smith and C. K. Williams, *Nature*, 2019, **575**, 87.
104 S. D. Angeli, G. Monteleone, A. Giaconia and A. A. Lemonidou, *Int. J. Hydrogen Energy*, 2014, **39**, 1979.
105 Y.-L. Lee, K. Lee, C. Hyun Ko and H.-S. Roh, *Chem. Eng. J.*, 2022, **431**, 134299.
106 S. Z. Abbas, V. Dupont and T. Mahmud, *Int. J. Hydrogen Energy*, 2017, **42**, 2889.
107 J. Xu and G. F. Froment, *AIChE J.*, 1989, **35**, 97.
108 G. Arzamendi, P. M. Diéguez, M. Montes, J. A. Odriozola, E. F. Sousa-Aguiar and L. M. Gandía, *Chem. Eng. J.*, 2009, **154**, 168.
109 P. N. Kechagiopoulos, S. D. Angeli and A. A. Lemonidou, *Appl. Catal., B*, 2017, **205**, 238.
110 D. Pashchenko and I. Makarov, *Energy*, 2021, **222**, 119993.
111 D. Pashchenko, *Int. J. Energy Res.*, 2020, **44**, 438.
112 Z. Zhu, W. Guo, Y. Zhang, C. Pan, J. Xu, Y. Zhu and Y. Lou, *Carbon Energy*, 2021, **3**, 519.
113 W. Li, J. Zhang and W. Wang, *Coord. Chem. Rev.*, 2024, **503**, 215638.
114 P. Gronchi, P. Centola and R. D. Rosso, *Appl. Catal., A*, 1997, **152**, 83.
115 B. Christian Enger, R. Lødeng and A. Holmen, *Appl. Catal., A*, 2008, **346**, 1.
116 C. Papadopoulou, H. Matralis and X. Verykios, in *Catalysis for Alternative Energy Generation*, 2012, pp. 57–127.
117 A. Álvarez, M. Borges, J. J. Corral-Pérez, J. G. Olcina, L. Hu, D. Cornu, R. Huang, D. Stoian and A. Urakawa, *ChemPhysChem*, 2017, **18**, 3135.
118 L. F. Bobadilla, V. Garcilaso, M. A. Centeno and J. A. Odriozola, *ChemSusChem*, 2017, **10**, 1193.
119 S. Xie, Q. Zhang, G. Liu and Y. Wang, *Chem. Commun.*, 2016, **52**, 35.
120 R. O. da Fonseca, R. C. Rabelo-Neto, R. C. C. Simões, L. V. Mattos and F. B. Noronha, *Int. J. Hydrogen Energy*, 2020, **45**, 5182.
121 B. Faroldi, J. Múnera, J. M. Falivene, I. R. Ramos, Á. G. García, L. T. Fernández, S. G. Carrazán and L. Cornaglia, *Int. J. Hydrogen Energy*, 2017, **42**, 16127.
122 J. Yang, J. Wang, J. Zhao, Y. Bai, H. Du, Q. Wang, B. Jiang and H. Li, *J. CO_2 Util.*, 2022, **57**, 101893.
123 C. Agrafiotis, H. von Storch, M. Roeb and C. Sattler, *Renewable Sustainable Energy Rev.*, 2014, **29**, 656.
124 M. F. Mark, W. F. Maier and F. Mark, *Chem. Eng. Technol.*, 1997, **20**, 361.
125 Y. Kathiraser, U. Oemar, E. T. Saw, Z. Li and S. Kawi, *Chem. Eng. J.*, 2015, **278**, 62.
126 E. le Saché and T. R. Reina, *Prog. Energy Combust. Sci.*, 2022, **89**, 100970.
127 C. Carrara, J. Múnera, E. A. Lombardo and L. M. Cornaglia, *Top. Catal.*, 2008, **51**, 98.
128 J.-H. Park and T.-S. Chang, *Catal. Lett.*, 2019, **149**, 3148.
129 I. de Dios García, A. Stankiewicz and H. Nigar, *Catal. Today*, 2021, **362**, 72.
130 K. Nagaoka, *Appl. Catal., A*, 2004, **268**, 151.
131 B. Pawelec, S. Damyanova, K. Arishtirova, J. L. G. Fierro and L. Petrov, *Appl. Catal., A*, 2007, **323**, 188.
132 M. García-Diéguez, I. S. Pieta, M. C. Herrera, M. A. Larrubia and L. J. Alemany, *Catal. Today*, 2011, **172**, 136.
133 B. Steinhauer, M. R. Kasireddy, J. Radnik and A. Martin, *Appl. Catal., A*, 2009, **366**, 333.
134 F. Menegazzo, M. Signoretto, F. Pinna, P. Canton and N. Pernicone, *Appl. Catal., A*, 2012, **439–440**, 80.

135 S. Zhang, M. Ying, J. Yu, W. Zhan, L. Wang, Y. Guo and Y. Guo, *Appl. Catal., B*, 2021, **291**, 120074.
136 K. Y. Kim, J. H. Lee, H. Lee, W. Y. Noh, E. H. Kim, E. C. Ra, S. K. Kim, K. An and J. S. Lee, *ACS Catal.*, 2021, **11**, 11091.
137 A. Abdulrasheed, A. A. Jalil, Y. Gambo, M. Ibrahim, H. U. Hambali and M. Y. Shahul Hamid, *Renewable Sustainable Energy Rev.*, 2019, **108**, 175.
138 O. Muraza and A. Galadima, *Int. J. Energy Res.*, 2015, **39**, 1196.
139 Y. Gao, J. Jiang, Y. Meng, F. Yan and A. Aihemaiti, *Energy Convers. Manage.*, 2018, **171**, 133.
140 A. Tavasoli and G. Ozin, *Joule*, 2018, **2**, 571.
141 A. V. Tavasoli, M. Preston and G. Ozin, *Energy Environ. Sci.*, 2021, **14**, 3098.
142 F. Pan, X. Xiang, W. Deng, H. Zhao, X. Feng and Y. Li, *ChemCatChem*, 2018, **10**, 940.
143 M. Mao, Q. Zhang, Y. Yang, Y. Li, H. Huang, Z. Jiang, Q. Hu and X. Zhao, *Green Chem.*, 2018, **20**, 2857.
144 L. Zhu, T. Ding, M. Gao, C. K. N. Peh and G. W. Ho, *Adv. Energy Mater.*, 2019, **9**, 1900250.
145 B. Han, W. Wei, L. Chang, P. Cheng and Y. H. Hu, *ACS Catal.*, 2016, **6**, 494.
146 H. Liu, H. Song, W. Zhou, X. Meng and J. Ye, *Angew. Chem., Int. Ed.*, 2018, **57**, 16781.
147 M. A. Boda, R. L. Withers, Y. Liu, J. Ye and Z. Yi, *J. Mater. Chem. A*, 2022, **10**, 22977.
148 Y. Li, D. Li, H. Liu, Y. Lei, R. Zhao, D. He, Z. Zheng, H. Luo and A. Liu, *Catal. Sci. Technol.*, 2024, **14**, 2722.
149 H. Liu, X. Meng, W. Yang, G. Zhao, D. He and J. Ye, *Chin. J. Catal.*, 2021, **42**, 1976.
150 N. Ma, N. Tanen, A. Verma, Z. Guo, T. Luo, H. (Grace) Xing and D. Jena, *Appl. Phys. Lett.*, 2016, **109**, 212101.
151 Y. Zhao, J. Qiao, Z. Yu, P. Yu, K. Xu, S. P. Lau, W. Zhou, Z. Liu, X. Wang, W. Ji and Y. Chai, *Adv. Mater.*, 2017, **29**, 1604230.
152 H. Song and J. Ye, *Trends Chem.*, 2022, **4**, 1094.
153 X. Meng, X. Cui, N. P. Rajan, L. Yu, D. Deng and X. Bao, *Chem*, 2019, **5**, 2296.
154 C. Peng, G. Reid, H. Wang and P. Hu, *J. Chem. Phys.*, 2017, **147**, 030901.
155 D. Hu, V. V. Ordomsky and A. Y. Khodakov, *Appl. Catal., B*, 2021, **286**, 119913.
156 S. Yuan, Y. Li, J. Peng, Y. M. Questell-Santiago, K. Akkiraju, L. Giordano, D. J. Zheng, S. Bagi, Y. Román-Leshkov and Y. Shao-Horn, *Adv. Energy Mater.*, 2020, **10**, 2002154.
157 R. A. Periana, D. J. Taube, S. Gamble, H. Taube, T. Satoh and H. Fujii, *Science*, 1998, **280**, 560.
158 R. Horn and R. Schlögl, *Catal. Lett.*, 2015, **145**, 23.
159 A. A. Latimer, A. R. Kulkarni, H. Aljama, J. H. Montoya, J. S. Yoo, C. Tsai, F. Abild-Pedersen, F. Studt and J. K. Nørskov, *Nat. Mater.*, 2017, **16**, 225.
160 A. A. Latimer, H. Aljama, A. Kakekhani, J. S. Yoo, A. Kulkarni, C. Tsai, M. Garcia-Melchor, F. Abild-Pedersen and J. K. Nørskov, *Phys. Chem. Chem. Phys.*, 2017, **19**, 3575.
161 N. J. Gunsalus, A. Koppaka, S. H. Park, S. M. Bischof, B. G. Hashiguchi and R. A. Periana, *Chem. Rev.*, 2017, **117**, 8521.
162 J. A. Labinger and J. E. Bercaw, *Nature*, 2002, **417**, 507.
163 A. I. Olivos-Suarez, À. Szécsényi, E. J. M. Hensen, J. Ruiz-Martinez, E. A. Pidko and J. Gascon, *ACS Catal.*, 2016, **6**, 2965.
164 Á. Szécsényi, G. Li, J. Gascon and E. A. Pidko, *ACS Catal.*, 2018, **8**, 7961.
165 J. Kim, M. S. Abbott, D. B. Go and J. C. Hicks, *ACS Energy Lett.*, 2016, **1**, 94.
166 C. R. H. de Smet, M. H. J. M. de Croon, R. J. Berger, G. B. Marin and J. C. Schouten, *Appl. Catal., A*, 1999, **187**, 33.
167 D. Hickman, *J. Catal.*, 1992, **138**, 267.
168 J. Haber and E. M. Serwicka, *React. Kinet. Catal. Lett.*, 1987, **35**, 369.
169 G. Groppi, W. Ibashi, M. Valentini and P. Forzatti, *Chem. Eng. Sci.*, 2001, **56**, 831.
170 K. Delgado, L. Maier, S. Tischer, A. Zellner, H. Stotz and O. Deutschmann, *Catalysts*, 2015, **5**, 871.
171 R. Schwiedernoch, S. Tischer, C. Correa and O. Deutschmann, *Chem. Eng. Sci.*, 2003, **58**, 633.
172 V. R. Choudhary, A. M. Rajput and B. Prabhakar, *J. Catal.*, 1993, **139**, 326.
173 D. Dissanayake, *J. Catal.*, 1991, **132**, 117.
174 G. A. Karim and G. Zhou, *Int. J. Hydrogen Energy*, 1993, **18**, 125.
175 A. Mosayebi, *J. Taiwan Inst. Chem. Eng.*, 2020, **114**, 36.
176 K. J. Warren and J. R. Scheffe, *Mater. Today Energy*, 2018, **9**, 39.
177 A. V. de Vekki and S. T. Marakaev, *Russ. J. Appl. Chem.*, 2009, **82**, 521.
178 K. T. Dinh, M. M. Sullivan, P. Serna, R. J. Meyer, M. Dincă and Y. Román-Leshkov, *ACS Catal.*, 2018, **8**, 8306.
179 M. H. Groothaert, P. J. Smeets, B. F. Sels, P. A. Jacobs and R. A. Schoonheydt, *J. Am. Chem. Soc.*, 2005, **127**, 1394.
180 C. Berger-Karin, J. Radnik and E. V. Kondratenko, *J. Catal.*, 2011, **280**, 116.
181 L. Li, S. He, Y. Song, J. Zhao, W. Ji and C.-T. Au, *J. Catal.*, 2012, **288**, 54.
182 Y. Hu and E. Ruckenstein, *J. Catal.*, 1996, **158**, 260.
183 T. V. Choudhary and V. R. Choudhary, *Angew. Chem., Int. Ed.*, 2008, **47**, 1828.
184 C. T. Au, H. Y. Wang and H. L. Wan, *J. Catal.*, 1996, **158**, 343.
185 R. K. Singha, A. Shukla, A. Yadav, L. N. Sivakumar Konathala and R. Bal, *Appl. Catal., B*, 2017, **202**, 473.
186 J. Saupsor, C. Pei, H. Li, S. Wongsakulphasatch, P. Kim-Lohsoontorn, S. Ratchahat, W. Kiatkittipong, S. Assabumrungrat and J. Gong, *Energy Fuels*, 2021, **35**, 11580.
187 Y. Feng, N. Wang and X. Guo, *Fuel*, 2021, **290**, 120094.
188 L. Zeng, Z. Cheng, J. A. Fan, L.-S. Fan and J. Gong, *Nat. Rev. Chem.*, 2018, **2**, 349.
189 S. Kim, J. Lauterbach and E. Sasmaz, *ACS Catal.*, 2021, **11**, 8247.
190 I. Grčić, J. Marčec, L. Radetić, A.-M. Radovan, I. Melnjak, I. Jajčinović and I. Brnardić, *Environ. Sci. Pollut. Res.*, 2021, **28**, 18354.

191 S. Sugiyama, Y. Hayashi, I. Okitsu, N. Shimoda, M. Katoh, A. Furube, Y. Kato and W. Ninomiya, *Catalysts*, 2020, **10**, 559.
192 S. Murcia-López, K. Villa, T. Andreu and J. R. Morante, *Chem. Commun.*, 2015, **51**, 7249.
193 H. Jiang, X. Peng, A. Yamaguchi, S. Ueda, T. Fujita, H. Abe and M. Miyauchi, *Sol. RRL*, 2019, **3**, 1900076.
194 K. R. Thampi, J. Kiwi and M. Grätzel, *Catal. Lett.*, 1988, **1**, 109.
195 F. Schüth, *Science*, 2019, **363**, 1282.
196 C. Mesters, *Annu. Rev. Chem. Biomol. Eng.*, 2016, **7**, 223.
197 H. Cruchade, I. C. Medeiros-Costa, N. Nesterenko, J.-P. Gilson, L. Pinard, A. Beuque and S. Mintova, *ACS Catal.*, 2022, **12**, 14533.
198 B. Beck, V. Fleischer, S. Arndt, M. G. Hevia, A. Urakawa, P. Hugo and R. Schomäcker, *Catal. Today*, 2014, **228**, 212.
199 C. Karakaya, H. Zhu, C. Loebick, J. G. Weissman and R. J. Kee, *Catal. Today*, 2018, **312**, 10.
200 J. Sun, J. Thybaut and G. Marin, *Catal. Today*, 2008, **137**, 90.
201 J. H. Lunsford, *Angew. Chem., Int. Ed. Engl.*, 1995, **34**, 970.
202 E. E. Wolf, *J. Phys. Chem. Lett.*, 2014, **5**, 986.
203 P. Schwach, X. Pan and X. Bao, *Chem. Rev.*, 2017, **117**, 8497.
204 Y. Gao, L. Neal, D. Ding, W. Wu, C. Baroi, A. M. Gaffney and F. Li, *ACS Catal.*, 2019, **9**, 8592.
205 Y. Simon, F. Baronnet, G. M. Côme and P. M. Marquaire, *Stud. Surf. Sci. Catal.*, 2004, **147**, 571.
206 P. M. Couwenberg, Q. Chen and G. B. Marin, *Ind. Eng. Chem. Res.*, 1996, **35**, 3999.
207 Z. Stansch, L. Mleczko and M. Baerns, *Ind. Eng. Chem. Res.*, 1997, **36**, 2568.
208 S. Da Ros, T. Barbalho Fontoura, M. Schwaab, N. Castro de Jesus and J. Pinto, *Processes*, 2021, **9**, 2196.
209 M. Y. Sinev, Z. T. Fattakhova, V. I. Lomonosov and Y. A. Gordienko, *J. Nat. Gas Chem.*, 2009, **18**, 273.
210 H. Zanthoff and M. Baerns, *Ind. Eng. Chem. Res.*, 1990, **29**, 2.
211 Q. Chen, P. M. Couwenberg and G. B. Marin, *Catal. Today*, 1994, **21**, 309.
212 Q. Chen, J. H. B. J. Hoebink and G. B. Marin, *Ind. Eng. Chem. Res.*, 1991, **30**, 2088.
213 Q. Chen, P. M. Couwenberg and G. B. Marin, *AIChE J.*, 1994, **40**, 521.
214 O. V. Buyevskaya, M. Rothaemel, H. W. Zanthoff and M. Baerns, *J. Catal.*, 1994, **146**, 346.
215 P. N. Kechagiopoulos, J. W. Thybaut and G. B. Marin, *Ind. Eng. Chem. Res.*, 2014, **53**, 1825.
216 R. H. Nibbelke, J. Scheerova, M. H. J. M. Decroon and G. B. Marin, *J. Catal.*, 1995, **156**, 106.
217 J. Sun, J. Thybaut and G. Marin, *Catal. Today*, 2008, **137**, 90.
218 T. Ito and J. H. Lunsford, *Nature*, 1985, **314**, 721–722.
219 B. Wood, *J. Catal.*, 2004, **225**, 300.
220 C. Hammond, N. Dimitratos, J. A. Lopez-Sanchez, R. L. Jenkins, G. Whiting, S. A. Kondrat, M. H. ab Rahim, M. M. Forde, A. Thetford, H. Hagen, E. E. Stangland, J. M. Moulijn, S. H. Taylor, D. J. Willock and G. J. Hutchings, *ACS Catal.*, 2013, **3**, 1835.
221 J.-F. Wu, X.-D. Gao, L.-M. Wu, W. D. Wang, S.-M. Yu and S. Bai, *ACS Catal.*, 2019, **9**, 8677.
222 Z. Liang, T. Li, M. Kim, A. Asthagiri and J. F. Weaver, *Science*, 2017, **356**, 299.
223 N. Basickes, T. E. Hogan and A. Sen, *J. Am. Chem. Soc.*, 1996, **118**, 13111.
224 T. Zimmermann, M. Soorholtz, M. Bilke and F. Schüth, *J. Am. Chem. Soc.*, 2016, **138**, 12395.
225 I. H. Hristov and T. Ziegler, *Organometallics*, 2003, **22**, 1668.
226 T. M. Gilbert, I. Hristov and T. Ziegler, *Organometallics*, 2001, **20**, 1183.
227 S. Chempath and A. T. Bell, *J. Am. Chem. Soc.*, 2006, **128**, 4650.
228 S. Song, H. Song, L. Li, S. Wang, W. Chu, K. Peng, X. Meng, Q. Wang, B. Deng, Q. Liu, Z. Wang, Y. Weng, H. Hu, H. Lin, T. Kako and J. Ye, *Nat. Catal.*, 2021, **4**, 1032.
229 H. Song, X. Meng, Z. Wang, H. Liu and J. Ye, *Joule*, 2019, **3**, 1606.
230 H. Li, J. Li, Z. Ai, F. Jia and L. Zhang, *Angew. Chem., Int. Ed.*, 2018, **57**, 122.
231 N. Li, R. Jiang, Y. Li, J. Zhou, Q. Ma, S. Shen and M. Liu, *ACS Sustain. Chem. Eng.*, 2019, **7**, 11455.
232 D. Gerceker, A. H. Motagamwala, K. R. Rivera-Dones, J. B. Miller, G. W. Huber, M. Mavrikakis and J. A. Dumesic, *ACS Catal.*, 2017, **7**, 2088.
233 K. Dutta, M. Shahryari, C.-J. Li and J. Kopyscinski, *Appl. Catal. A Gen.*, 2023, **663**, 119319.
234 D. Bajec, A. Kostyniuk, A. Pohar and B. Likozar, *Chem. Eng. J.*, 2020, **396**, 125182.
235 M. Kottwitz, Y. Li, R. M. Palomino, Z. Liu, G. Wang, Q. Wu, J. Huang, J. Timoshenko, S. D. Senanayake, M. Balasubramanian, D. Lu, R. G. Nuzzo and A. I. Frenkel, *ACS Catal.*, 2019, **9**, 8738.
236 S. K. Kim, H. W. Kim, S. J. Han, S. W. Lee, J. Shin and Y. T. Kim, *Commun. Chem.*, 2020, **3**, 58.
237 S. F. Moya, R. L. Martins, A. Ota, E. L. Kunkes, M. Behrens and M. Schmal, *Appl. Catal., A*, 2012, **411–412**, 105.
238 H. Sheng, E. P. Schreiner, W. Zheng and R. F. Lobo, *ChemPhysChem*, 2018, **19**, 504.
239 L. Wang, L. Tao, M. Xie, G. Xu, J. Huang and Y. Xu, *Catal. Lett.*, 1993, **21**, 35.
240 D. Soulivong, S. Norsic, M. Taoufik, C. Coperet, J. Thivolle-Cazat, S. Chakka and J.-M. Basset, *J. Am. Chem. Soc.*, 2008, **130**, 5044.
241 X. Guo, G. Fang, G. Li, H. Ma, H. Fan, L. Yu, C. Ma, X. Wu, D. Deng, M. Wei, D. Tan, R. Si, S. Zhang, J. Li, L. Sun, Z. Tang, X. Pan and X. Bao, *Science*, 2014, **344**, 616–619.
242 Y. Xiao and A. Varma, *ACS Catal.*, 2018, **8**, 2735.
243 Z. Li, Y. Xiao, P. R. Chowdhury, Z. Wu, T. Ma, J. Z. Chen, G. Wan, T.-H. Kim, D. Jing, P. He, P. J. Potdar, L. Zhou, Z. Zeng, X. Ruan, J. T. Miller, J. P. Greeley, Y. Wu and A. Varma, *Nat. Catal.*, 2021, **4**, 882.
244 Y. Kato, H. Yoshida and T. Hattori, *Chem. Commun.*, 1998, 2389–2390.
245 S. Murcia-López, M. C. Bacariza, K. Villa, J. M. Lopes, C. Henriques, J. R. Morante and T. Andreu, *ACS Catal.*, 2017, **7**, 2878.
246 Y. Kato, N. Matsushita, H. Yoshida and T. Hattori, *Catal. Commun.*, 2002, **3**, 99.

247 S. Wu, L. Wang and J. Zhang, *J. Photochem. Photobiol., C*, 2021, **46**, 100400.
248 W. Zhang, C. Fu, J. Low, D. Duan, J. Ma, W. Jiang, Y. Chen, H. Liu, Z. Qi, R. Long, Y. Yao, X. Li, H. Zhang, Z. Liu, J. Yang, Z. Zou and Y. Xiong, *Nat. Commun.*, 2022, **13**, 2806.
249 T. Sakthivel, G. Venugopal, A. Durairaj, S. Vasanthkumar and X. Huang, *J. Ind. Eng. Chem.*, 2019, **72**, 18.
250 M. M. Vijatovic Petrovic and J. D. Bobic, in *Magnetic, Ferroelectric, and Multiferroic Metal Oxides*, Elsevier, 2018, pp. 35–49.
251 X. Deng, Y. Wu, Z. Gao and G. Zhou, *J. Mater. Chem. A*, 2024, **12**, 567.
252 A. G. Chynoweth, *Phys. Rev.*, 1956, **102**, 705.
253 A. M. Glass, D. von der Linde, D. H. Auston and T. J. Negran, *J. Electron. Mater.*, 1975, **4**, 915.
254 A. M. Glass, D. von der Linde and T. J. Negran, *Appl. Phys. Lett.*, 1974, **25**, 233.
255 S. Tu, Y. Zhang, A. H. Reshak, S. Auluck, L. Ye, X. Han, T. Ma and H. Huang, *Nano Energy*, 2019, **56**, 840.
256 Y. Wang, M. Zhang, J. Liu, H. Zhang, F. Li, C. Tseng, B. Yang, G. Smith, J. Zhai, Z. Zhang, S. Dunn and H. Yan, *Adv. Energy Mater.*, 2020, **10**, 2001802.
257 Y. AlSalka, L. I. Granone, W. Ramadan, A. Hakki, R. Dillert and D. W. Bahnemann, *Appl. Catal., B*, 2019, **244**, 1065.
258 I. Dierking and S. Al-Zangana, *Nanomaterials*, 2017, **7**, 305.
259 I. Dierking, *Nanomaterials*, 2018, **8**, 453.
260 S. K. Gupta, D. Budaszewski and D. P. Singh, *Eur. Phys. J.: Spec. Top.*, 2022, **231**, 673.
261 R. B. Meyer, L. Liebert, L. Strzelecki and P. Keller, *J. Phys., Lett.*, 1975, **36**, 69.
262 S. K. Gupta, Z. Sun, H.-S. Kwok and A. K. Srivastava, *Liq. Cryst.*, 2020, **47**, 1162.
263 S. Mukherjee, Z. Yuan, Z. Sun, A. Li, C. Kang, H.-S. Kwok and A. K. Srivastava, *Opt. Express*, 2021, **29**, 8258.
264 P. Berthele, E. Gros, B. Fracasso and J.-L. de B. de la Tocnaye, *Ferroelectrics*, 1998, **214**, 117.
265 S. Al-Zangana, M. Turner and I. Dierking, *J. Appl. Phys.*, 2017, **121**, 085105.
266 A. Mertelj, D. Lisjak, M. Drofenik and M. Čopič, *Nature*, 2013, **504**, 237.
267 Y. Yuan, T. J. Reece, P. Sharma, S. Poddar, S. Ducharme, A. Gruverman, Y. Yang and J. Huang, *Nat. Mater.*, 2011, **10**, 296.
268 B. B. Tian, J. L. Wang, S. Fusil, Y. Liu, X. L. Zhao, S. Sun, H. Shen, T. Lin, J. L. Sun, C. G. Duan, M. Bibes, A. Barthélémy, B. Dkhil, V. Garcia, X. J. Meng and J. H. Chu, *Nat. Commun.*, 2016, **7**, 11502.
269 Y. Liu, H. Aziguli, B. Zhang, W. Xu, W. Lu, J. Bernholc and Q. Wang, *Nature*, 2018, **562**, 96.
270 B. Neese, B. Chu, S.-G. Lu, Y. Wang, E. Furman and Q. M. Zhang, *Science*, 2008, **321**, 821.
271 H. Li, F. Liu, B. Fan, D. Ai, Z. Peng and Q. Wang, *Small Methods*, 2018, **2**, 1700399.
272 Y. Cui, Z. Wang, B. Li, Y. Yan, R. Xu, M. Meng and Y. Yan, *Nano Energy*, 2022, **99**, 107429.
273 Z. Wei, T. Ji, X. Zhou, J. Guo, X. Yu, H. Liu and J. Wang, *Small*, 2023, **19**, 2304202.
274 C. Yang, P. Wang, J. Li, Q. Wang, P. Xu, S. You, Q. Zheng and G. Zhang, *Chem. Eng. J.*, 2021, **417**, 129340.
275 S. Horiuchi and Y. Tokura, *Nat. Mater.*, 2008, **7**, 357.
276 A. L. Solomon, *Phys. Rev.*, 1956, **104**, 1191.
277 D. Bordeaux, J. Bornarel, A. Capiomont, J. Lajzerowicz-Bonneteau, J. Lajzerowicz and J. F. Legrand, *Phys. Rev. Lett.*, 1973, **31**, 314.
278 P. Gruner-Bauer and E. Dormann, *J. Phys.: Condens. Matter*, 1992, **4**, 5599.
279 J. Valasek, *Phys. Rev.*, 1921, **17**, 475.
280 Y. Sekine, R. Akiyoshi and S. Hayami, *Coord. Chem. Rev.*, 2022, **469**, 214663.
281 T. Hang, W. Zhang, H.-Y. Ye and R.-G. Xiong, *Chem. Soc. Rev.*, 2011, **40**, 3577.
282 T. Zhang, K. Xu, J. Li, L. He, D. W. Fu, Q. Ye and R. G. Xiong, *Natl. Sci. Rev.*, 2023, **10**, nwac240.
283 R. Naaman, Y. Paltiel and D. H. Waldeck, *Nat. Rev. Chem.*, 2019, **3**, 250.
284 X.-B. Han, C.-Y. Chai, B.-D. Liang, C.-C. Fan and W. Zhang, *CrystEngComm*, 2022, **24**, 1507.
285 N. A. Spaldin, *J. Solid State Chem.*, 2012, **195**, 2.
286 H. Huyan, L. Li, C. Addiego, W. Gao and X. Pan, *Natl. Sci. Rev.*, 2019, **6**, 669.
287 W. Zheng, X. Wang, X. Zhang, B. Chen, H. Suo, Z. Xing, Y. Wang, H. Wei, J. Chen, Y. Guo and F. Wang, *Adv. Mater.*, 2023, **35**, 2205410.
288 D. Li, J. Shi, Y. Xu, Y. Luo, H. Wu and Q. Meng, *Natl. Sci. Rev.*, 2018, **5**, 559.
289 Z. Sun, X. Liu, T. Khan, C. Ji, M. A. Asghar, S. Zhao, L. Li, M. Hong and J. Luo, *Angew. Chem., Int. Ed.*, 2016, **55**, 6545.
290 J.-X. Gao, W.-Y. Zhang, Z.-G. Wu, Y.-X. Zheng and D.-W. Fu, *J. Am. Chem. Soc.*, 2020, **142**, 4756.
291 C. Ji, S. Wang, L. Li, Z. Sun, M. Hong and J. Luo, *Adv. Funct. Mater.*, 2019, **29**, 1805038.
292 K. T. Butler, J. M. Frost and A. Walsh, *Energy Environ. Sci.*, 2015, **8**, 838.
293 Y. Sun, G. Niu, W. Ren, X. Meng, J. Zhao, W. Luo, Z.-G. Ye and Y.-H. Xie, *ACS Nano*, 2021, **15**, 10982.
294 C. Wang, Y. Ding, B. Liu, B. Weng, J. Hofkens and M. B. J. Roeffaers, *Chem. Commun.*, 2023, **59**, 3122.
295 K. Li, S. Li, W. Zhang, Z. Shi, D. Wu, X. Chen, P. Lin, Y. Tian and X. Li, *J. Colloid Interface Sci.*, 2021, **596**, 376.
296 J. San Martin, N. Dang, E. Raulerson, M. C. Beard, J. Hartenberger and Y. Yan, *Angew. Chem., Int. Ed.*, 2022, **61**, e202205572.
297 X. Zhu, Y. Lin, J. San Martin, Y. Sun, D. Zhu and Y. Yan, *Nat. Commun.*, 2019, **10**, 2843.
298 K. Chang, J. Liu, H. Lin, N. Wang, K. Zhao, A. Zhang, F. Jin, Y. Zhong, X. Hu, W. Duan, Q. Zhang, L. Fu, Q.-K. Xue, X. Chen and S.-H. Ji, *Science*, 2016, **353**, 274.
299 W. Ding, J. Zhu, Z. Wang, Y. Gao, D. Xiao, Y. Gu, Z. Zhang and W. Zhu, *Nat. Commun.*, 2017, **8**, 14956.
300 A. Chandrasekaran, A. Mishra and A. K. Singh, *Nano Lett.*, 2017, **17**, 3290.
301 J. Muñoz, *Adv. Mater.*, 2024, **36**, 2305546.
302 Q. Yang, W. Xiong, L. Zhu, G. Gao and M. Wu, *J. Am. Chem. Soc.*, 2017, **139**, 11506.

303 K. L. Seyler, D. Zhong, D. R. Klein, S. Gao, X. Zhang, B. Huang, E. Navarro-Moratalla, L. Yang, D. H. Cobden, M. A. McGuire, W. Yao, D. Xiao, P. Jarillo-Herrero and X. Xu, *Nat. Phys.*, 2018, **14**, 277.
304 B. Huang, G. Clark, E. Navarro-Moratalla, D. R. Klein, R. Cheng, K. L. Seyler, D. Zhong, E. Schmidgall, M. A. McGuire, D. H. Cobden, W. Yao, D. Xiao, P. Jarillo-Herrero and X. Xu, *Nature*, 2017, **546**, 270.
305 C. Gong, L. Li, Z. Li, H. Ji, A. Stern, Y. Xia, T. Cao, W. Bao, C. Wang, Y. Wang, Z. Q. Qiu, R. J. Cava, S. G. Louie, J. Xia and X. Zhang, *Nature*, 2017, **546**, 265.
306 L. Kou, Y. Ma, T. Liao, A. Du and C. Chen, *Phys. Rev. Appl.*, 2018, **10**, 024043.
307 Y. Lei, X. Sala, J. García-Antón and J. Muñoz, *Small Methods*, 2024.
308 Y. Lei, Á. Campos-Lendínez, X. Sala, J. García-Antón and J. Muñoz, *Small Struct.*, 2025, **6**, 2400240.
309 J. Muñoz, M. Palacios-Corella, I. J. Gómez, L. Zajíčková and M. Pumera, *Adv. Mater.*, 2022, **34**, 2206382.
310 J. L. Giocondi and G. S. Rohrer, *Top. Catal.*, 2008, **49**, 18.
311 G. F. Nataf, M. Guennou, J. Kreisel, P. Hicher, R. Haumont, O. Aktas, E. K. H. Salje, L. Tortech, C. Mathieu, D. Martinotti and N. Barrett, *Phys. Rev. Mater.*, 2017, **1**, 074410.
312 K. Garrity, A. M. Kolpak, S. Ismail-Beigi and E. I. Altman, *Adv. Mater.*, 2010, **22**, 2969.
313 M. Du, W. Liu, N. Liu, Y. Ling and S. Kang, *Nano Energy*, 2024, **124**, 109495.
314 S. Park, C. W. Lee, M.-G. Kang, S. Kim, H. J. Kim, J. E. Kwon, S. Y. Park, C.-Y. Kang, K. S. Hong and K. T. Nam, *Phys. Chem. Chem. Phys.*, 2014, **16**, 10408.
315 F. Wu, Y. Yu, H. Yang, L. N. German, Z. Li, J. Chen, W. Yang, L. Huang, W. Shi, L. Wang and X. Wang, *Adv. Mater.*, 2017, **29**, 1701432.
316 W. Li, F. Wang, M. Li, X. Chen, Z. Ren, H. Tian, X. Li, Y. Lu and G. Han, *Nano Energy*, 2018, **45**, 304.
317 R. Munprom, P. A. Salvador and G. S. Rohrer, *J. Mater. Chem. A*, 2016, **4**, 2951.
318 N. V. Burbure, P. A. Salvador and G. S. Rohrer, *Chem. Mater.*, 2010, **22**, 5831.
319 A. Kakekhani and S. Ismail-Beigi, *ACS Catal.*, 2015, **5**, 4537.
320 N. P. Zangeneh, S. Sharifnia and E. Karamian, *Environ. Sci. Pollut. Res.*, 2020, **27**, 5912.
321 Z. Du, C. Petru, X. Yang, F. Chen, S. Fang, F. Pan, Y. Gang, H.-C. Zhou, Y. H. Hu and Y. Li, *J. CO_2 Util.*, 2023, **67**, 102317.
322 L. Jiang, Y. Zhang, Y. Qiu and Z. Yi, *RSC Adv.*, 2014, **4**, 3165.
323 R. Von der Mühll, A. Sadel and P. Hagenmuller, *J. Solid State Chem.*, 1984, **51**, 176.
324 K. Garrity, A. Kakekhani, A. Kolpak and S. Ismail-Beigi, *Phys. Rev. B: Condens. Matter Mater. Phys.*, 2013, **88**, 045401.
325 B. O. Alawode and A. M. Kolpak, *J. Phys. Chem. Lett.*, 2016, **7**, 1310.
326 Z. Li, M. A. Boda, X. Pan and Z. Yi, *ACS Sustain. Chem. Eng.*, 2019, **7**, 19042.
327 L. Meng, Z. Chen, Z. Ma, S. He, Y. Hou, H.-H. Li, R. Yuan, X.-H. Huang, X. Wang, X. Wang and J. Long, *Energy Environ. Sci.*, 2018, **11**, 294.
328 B. Dai, Y. Chen, S. Hao, H. Huang, J. Kou, C. Lu, Z. Lin and Z. Xu, *J. Phys. Chem. Lett.*, 2020, **11**, 7407.
329 A. M. Schultz, Y. Zhang, P. A. Salvador and G. S. Rohrer, *ACS Appl. Mater. Interfaces*, 2011, **3**, 1562.
330 H. S. Kushwaha, A. Halder and R. Vaish, *J. Mater. Sci.*, 2018, **53**, 1414.
331 Y. Yun and E. I. Altman, *J. Am. Chem. Soc.*, 2007, **129**, 15684.
332 M. H. Zhao, D. A. Bonnell and J. M. Vohs, *Surf. Sci.*, 2008, **602**, 2849.
333 X. Tang, J. Shang, Y. Ma, Y. Gu, C. Chen and L. Kou, *ACS Appl. Mater. Interfaces*, 2020, **12**, 39561.
334 T. L. Wan, L. Ge, Y. Pan, Q. Yuan, L. Liu, S. Sarina and L. Kou, *Nanoscale*, 2021, **13**, 7096.
335 J. Y. Y. Loh, N. P. Kherani and G. A. Ozin, *Nat. Sustainability*, 2021, **4**, 466.
336 W. Ding, J. Lu, X. Tang, L. Kou and L. Liu, *ACS Omega*, 2023, **8**, 6164.
337 J. Xie, C. Guo, P. Yang, X. Wang, D. Liu and C. M. Li, *Nano Energy*, 2017, **31**, 28.
338 C. Noguera, *J. Phys.: Condens. Matter*, 2000, **12**, R367.
339 A. M. Kolpak, I. Grinberg and A. M. Rappe, *Phys. Rev. Lett.*, 2007, **98**, 166101.
340 C. Zhen, J. C. Yu, G. Liu and H.-M. Cheng, *Chem. Commun.*, 2014, **50**, 10416.
341 F. Chen, Z. Ren, S. Gong, X. Li, G. Shen and G. Han, *Chem.–Eur. J.*, 2016, **22**, 12160.
342 A. J. Welch, I. A. Digdaya, R. Kent, P. Ghougassian, H. A. Atwater and C. Xiang, *ACS Energy Lett.*, 2021, 1540.
343 J. Baltrusaitis, I. Jansen and J. D. Schuttlefield Christus, *Catal. Sci. Technol.*, 2014, **4**, 2397.
344 R. Li, L.-P. Qiu, S.-Z. Cao, Z. Li, S.-L. Gao, J. Zhang, S. Ramakrishna, Y.-Z. Long, R. Li, L.-P. Qiu, S.-Z. Cao, Z. Li, S.-L. Gao, J. Zhang, Y.-Z. Long and S. Ramakrishna, *Adv. Funct. Mater.*, 2024, 2316725.
345 P. Rovillain, R. de Sousa, Y. Gallais, A. Sacuto, M. A. Méasson, D. Colson, A. Forget, M. Bibes, A. Barthélémy and M. Cazayous, *Nat. Mater.*, 2010, **9**, 975.
346 A. Kumar, J. F. Scott and R. S. Katiyar, *Appl. Phys. Lett.*, 2011, **99**, 062504.